Dual Circularly Polarized Antennas for Full-duplex Radios

A

Thesis Submitted

in Fulfilment of the Requirements

for the Degree of

DOCTOR OF PHILOSOPHY

By

Sumantra Chaudhuri

Department of Electronics and Electrical Engineering
Indian Institute of Technology Guwahati
Guwahati, India.
April, 2020

Certificate

This is to certify that the thesis entitled "**Dual Circularly Polarized Antennas for Full-duplex Radios**", submitted by **Sumantra Chaudhuri** (156102019), a PhD student in the *Department of Electronics and Electrical Engineering, Indian Institute of Technology Guwahati*, for the award of the degree of **Doctor of Philosophy**, has been carried out by him under our supervision and guidance. The thesis has fulfilled all requirements as per the regulations of the Institute and in our opinion has reached the standard needed for submission. The results embodied in this thesis have not been submitted to any other university or institute for the award of any degree or diploma.

Prof. Rakhesh Singh Kshetrimayum
Professor,

Dr. Ramesh Kumar Sonkar
Assistant Professor,

Dept. of Electronics and Electrical Engineering,
Indian Institute of Technology Guwahati,
Assam - 781039.


भारतीय प्रौद्योगिकी संस्थान गुवाहाटी
Indian Institute of Technology Guwahati

Acknowledgements

This thesis is the culmination of my quest for PhD at the pinnacle of my research career as a student. At this stage I ponder over my journey and take the pleasure of expressing my gratitude to all those who contributed in various degrees to its success.

Foremost, my profound gratitude goes to my supervisors Prof. Rakhesh Singh Kshetrimayum and Dr. Ramesh Kumar Sonkar who had been my seemingly inexhaustible source of guidance, encouragement and valuable comments on my work. I appreciate the freedom they gave me to think deeply and explore novel ideas and most importantly the patience they have showed in reading and commenting on the manuscripts and several revisions of this dissertation. I do not hesitate to admit that timely completion of my PhD would have been impossible without their help.

I take this opportunity to thank my Doctoral Committee members for annually reviewing my work and their incisive questions that kept me unwavering on my track.

I would like to recognize the invaluable comments I received from Dr. Mahima Arrawatia time to time that played no trivial role in shaping this thesis.

I thank my colleagues Mr. Darpan Mishra, Mr. Mohit Mishra, Mr. Arijit Bhattacharjee, Mr. Bhaskar Saha and Dr. Ranjan Maity for their motivation and logistical support.

I express my whole-hearted appreciation to my dear friends Mr. Haradhan Chel and Dr. Biplab Ketan Chakraborty for their support in various capacities that are too numerous to mention.

A sense of indebtedness is also expressed to my MS supervisor Prof. Harishankar Ramachandran of IIT Madras whose dedicated personal and professional guidance enhanced my knowledge considerably about both scientific research and life in general. I candidly acknowledge that working under his guidance is an experience I will cherish for a long time to come.

Lastly, my deepest sense of gratitude is reserved only for my parents Mr. Debes Kumar Chaudhuri and Mrs. Shibani Chaudhuri, my brother Mr. Saptarshi Chaudhuri and my late aunt Mrs. Gita Chatterjee who reposed faith in my abilities when I had very little in mine.

Sumantra Chaudhuri

Abstract

Dual polarized planar antennas have great potential to increase channel capacity and minimize space requirement in modern wireless communication. Such antennas should essentially have highly decoupled ports and broad bandwidths that will reduce receiver complexity in communication systems. Of special interest are dual circularly polarized (DCP) antennas which, because of their superior properties compared to dual linearly polarized antennas and therefore find their utility in satellite communications, radars, altimetry, etc. This thesis therefore begins with the theory of planar antennas i.e. microstrip antennas and slot antennas exploring methods of generating circularly polarized (CP) waves from these antennas. A detailed study of the existing DCP antennas and port-decoupling in dual linearly polarized (DLP) antennas is made from which it is inferred that many of the techniques employed in the latter can be incorporated in the former for better port isolation. Moreover, since the bandwidths of the DCP antennas should be large, CP slot antennas can be possible candidates for extension to their DCP counterparts. It is with this rationale, three different kinds of DCP slot antennas employing different port-decoupling techniques have been presented. The first two antennas have slotted ground apertures excited by feed-lines with port-decoupling accomplished by means of interdigital capacitor and split-ring resonator-based metasurface which shows the characteristics of an electromagnetic bandgap (EBG) structure. Furthermore, to overcome the issue of low gain in slot antennas, a series-fed array of slots backed by a metallic reflector is designed which has a high gain apart from other useful properties namely high port-isolation and broad impedance and AR bandwidth. In this antenna, in spite of its ostensibly simple structure, a number of geometric parameters were found to tightly control its overall performance in general and the axial ratio (AR) and gain in particular. We have also demonstrated that using parasitic patches and defected ground structure (DGS) in a DCP patch antenna can greatly enhance its properties namely - impedance bandwidth, axial ratio bandwidth, gain, cross-polarization discrimination and interport isolation. In all these cases, details of design and mechanism of action are discussed. The simulated results are observed to reasonably tally with the measured data. Additionally, MIMO parameters, namely envelope correlation coefficient (ECC) and diversity gain (DG), were calculated for each of the novel antennas presented here.

Contents

List of Figures

List of Tables

List of Acronyms

AR	Axial ratio
ARBW	Axial ratio bandwidth
BSF	Bandstop filter
CP	Circularly polarized (or circular polarization)
CPW	Coplanar waveguide
CSSR	Complementary Square Spiral Resonator
DCP	Dual circularly polarized
DG	Diversity gain
DGS	Defected ground structure
DLP	Dual linearly polarized
EBG	Electromagnetic band-gap
ECC	Envelope correlation coefficient
EIW	Electromagnetic isolation wall
EM	Electromagnetic or electromagnetism
EMC	Electromagnetic coupling
FBR	Front-to-back ratio
FDX	Full-duplex
FSS	Frequency selective surface
IBFD	In band full duplex
IDC	Interdigital capacitor
LHCP	Left-handed circularly polarized
LP	Linear polarization
MIC	Microwave integrated circuit
MIMO	Multiple input multiple output
MLI	Meander line inductor
MNG	mu negative
MS	Metasurface

MTM	Metamaterial
NF	Noise figure
NL	Neutralization line
PEC	Perfect electric conductor
PIFA	Planar inverted F-antenna
PMC	Perfect magnetic conductor
RHCP	Right-handed circularly polarized
SI	Self interference
SIC	Self interference cancellation
SIW	Substrate integrated waveguide
SLL	Sidelobe level
SRR	Split-ring resonators
TE	Transverse electric
TM	Transverse magnetic
UAV	Unmanned aerial vehicle
UWB	Ultra wideband
VSWR	Voltage standing wave ratio
XPD	Cross polarization discrimination

List of Symbols

ε_r	Relative permittivity
$\tan\delta_{eff}$	Effective loss-tangent
Q	Quality factor
∇^2	Laplacian
$\vec{A}$	Magnetic vector potential
$k_{x,y,z}$	Wave number along X-, Y- or Z- axis
f_r or f_0	Resonant frequency
f_{AR}	Centre frequency of AR bandwidth
λ_r or λ_0	Wavelength at resonant frequency
η_0	Characteristic impedance of free-space
R_r	Radiation resistance
$\boldsymbol{\mu_e}$	Magnetic moment
f_p	Larmor frequency
G_T	Gain of transmitting antenna
G_R	Gain of receiving antenna
ε_{re}	Effective relative permittivity
Z_0	Characteristic impedance of transmission line
γ	Power coupling coefficient of a single radiator


भारतीय प्रौद्योगिकी संस्थान गुवाहाटी
Indian Institute of Technology Guwahati

1

Introduction

Dual circularly polarized planar antennas are essential for many types of wireless communications like satellite communication, radars, radio altimetry, and other applications where increased throughput is required at minimal volume and many unwanted phenomena like Faraday rotation and multipath need to be combated. This chapter begins with a discussion on the theory of planar antennas followed by explanation of the terms commonly associated with circular polarization and measurement techniques of different parameters for antenna characterization. The last but one section explores different types of planar circularly polarized antennas. Finally, the organization of the thesis is given at the end of this chapter.

1.1 Introduction

The last few decades have seen an unprecedented growth in wireless communication that has resulted in overlapping frequency bands for various applications in the radio spectrum. Therefore, a large number of applications have to compete over the allocated band that has necessitated adoption of polarization diversity in a single antenna to help overcome spectrum crunch which fuels the need of dual polarized (DP) antennas. It may be pointed out though, that designing DP antennas is a formidable task because of the trade-off that exists between antenna proximity and inter-port isolation. Moreover, other design goals that have to be commonly met are - realizing wide bandwidth and beamwidth while having a simple structure [?].

As will be seen in later part of this chapter, the nature of polarization of the antenna is of great importance in many applications based upon which DP antennas can either be dual linearly polarized (DLP) or dual circularly polarized (DCP). Of these two, this thesis is concerned with only the latter type because of its several advantages that are described in details in one of the later sections. The DCP antennas can be further classified as non-planar antennas and planar antennas and some instances of embodiment of the former can be found in [?, ?, ?, ?, ?, ?, ?, ?, ?]. In [?], a conical four-armed sinuous DCP antenna with a beamforming network is presented that operates over a wide frequency band with a high gain in the boresight direction and good inter-port isolation. Slots cut in waveguides form waveguide slot array antenna which can be configured to operate as DCP antennas as demonstrated in [?, ?, ?]. These antennas are seen to have very high gains ($\approx$ 27 dBic), low side-lobe levels ($\approx$ 18 dB) as in [?] and wide impedance bandwidth ($\approx$ 28%) as in [?]. For handling high power, DCP horn antennas are ideal which have been discussed in [?, ?, ?, ?]. Chakrabarti [?] proposed a DCP conical horn antenna with stepped metal septum having high wide band and low cross-polarization levels apart from high gain (12.7 to 14.5 dBic). Gatti and Rossi [?] presented a DCP horn antenna array excited using two interleaved slotted ridge waveguide arrays. In this work, the two orthogonal circular polarizations (CPs) are realized using linear-to-circular polarization converter in a 24×8 array which has a very high gain ($>$ 30 dBic) and low cross polarization. Jazani and Pirhadi [?] present a a quad-ridged DCP horn antenna with a septum polarizer and waveguide feed that has wide bandwidth (40%) and high gain (9 to 11 dBic) in its operational band. DCP horn antennas can also be used in W-band mm wave communications as presented in [?] based on a stepped septum polarizer that has a good CP performance over a large bandwidth and high gain.

It should be noted however, that in spite of showing excellent performances, the aforementioned antennas (i.e. conical sinuous, slotted waveguide array, and horn antennas) are bulky, expensive, and difficult to manufacture and are therefore unsuitable for personal, mobile, hand-held, and picosatellite communication. This leads the present day antenna designers to consider planar antennas that have low weight, electrically small profile, low cost, and ease of fabrication for which planar antennas like microstrip patch antenna and planar slot antennas are ideal as they are useful in designing wearable antennas and integration in MMICs [?]. It is thus important to understand the theory of such antennas towards which the Sections 1.3 and 1.4 are dedicated.

1.2 Advantages and applications of planar antennas

Advantages: The main advantages of planar antennas like microstrip patch antenna and planar slot antenna are [?, ?]

- Because of the advancements in printed-circuit technology, such antennas can be produced in bulk at a very low unit cost.
- These antennas are generally lightweight and occupy a low volume.
- They are more resistant to shocks and vibrations although failures do occur at the soldered joints and connectors.
- A large variety of shapes of these antennas can be designed using full-wave commercial EM simulation tools because of which planar antennas of various properties can be designed.
- Other active and passive microwave devices can be easily integrated with such antennas for desirable properties.
- These antennas can be made conformal which allows them to be mounted easily on surfaces of terrestrial and airborne vehicles.

Applications: A large number of applications of planar antennas can be found in various sectors [?, ?, ?] which include industries, aerospace, communication, medical and scientific study.

Moreover, wearable antennas can be designed for various purposes. In wireless communication, printed planar antennas are common in GPS, WLAN, Bluetooth, WiMax, GSM and WiFi applications. With the explosion of Internet-of-things (IoT) and 5G technology, these antennas are increasingly being sought after for their attractive properties mentioned above. Also, since these antennas can easily be configured to operate in CP mode, their usage in satellite communications (especially nano- and pico-satellites) and UAV are showing an upward trend. In medicine, planar antennas are used as a part of diagnostic systems for real-time monitoring of blood-pressure, insulin and endoscopic procedure [?]. One of the most promising fields where these antennas are finding their usage is biotelemetry where, by exploiting the low-profile and conformal nature of such antennas, implantable antennas are becoming indispensable.

1.3 Theory of microstrip patch antenna-cavity model

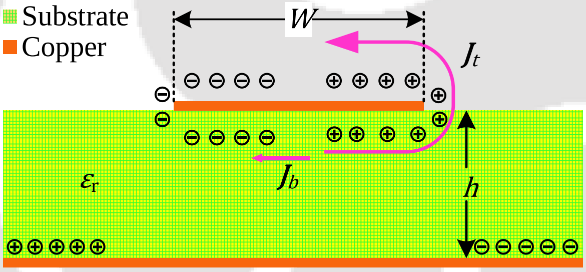

Fig. 1.1: Cavity-model of microstrip patch antenna [2]

The cavity model [2] is valid only when the height of the substrate h is much smaller than the operational wavelength of the antenna λ_0. We consider a mirostrip patch antenna of substrate height h and patch-width W as shown in Fig. 1.1. In this case, the top surface and the bottom surface of the patch antenna are considered to be Perfect Electric Conductors (PECs). When the microstrip patch is excited, a charge-distribution is developed on the upper and lower surfaces of the patch and at the bottom of the ground plane. This charge distribution is controlled by two mechanisms – an attractive mechanism and a repulsive mechanism. The former is between the opposite charges on the bottom side of the patch and the ground plane, which helps in keeping the charge concentration intact at the bottom of the patch. The repulsive mechanism is between the like charges on the bottom surface of the patch, which causes pushing of some charges from the bottom, to the top of the patch. As a result of this charge movement, currents flow at the top and bottom surfaces of the patch. Since this model assumes that the thickness of the substrate is very small compared to the width of the patch, the attractive mechanism dominates the repulsive mechanism and causes most of the charge concentration and the current to be below the patch surface. Much less current would flow on the top surface of the patch and as the height to width ratio further decreases, the current on the top surface of the patch would be almost equal to zero, which would not allow the creation of any tangential magnetic field components to the patch edges. Hence if $\vec{J_b}$ and $\vec{J_t}$ are the attraction and repulsion current densities respectively, then $\vec{J_t} \ll \vec{J_b}$. Therefore, the side-walls become Perfect Magnetic Conductors (PMC)s or $\vec{H}_\perp = 0$ as $\lim \vec{J_T} \rightarrow 0$.

It should be noted that if the walls of the cavity and the substrate are perfectly lossless, the impedance will be purely imaginary and the antenna will not radiate. Therefore a loss tangent $\tan\delta_{eff}$ is introduced, the inverse of which is the antenna quality factor Q $(Q = (1/\tan\delta_{eff}))$.

Because the substrate has a negligible thickness, the electric fields are almost normal to the surface and the fringing fields are very small. This is the reason why only the TM^x mode is considered. The expressions for resonant frequencies of TM^x_{010}, TM^x_{001} and TM^x_{020} mode can be found in Appendix A.1.

1.4 Theory of planar slot antenna

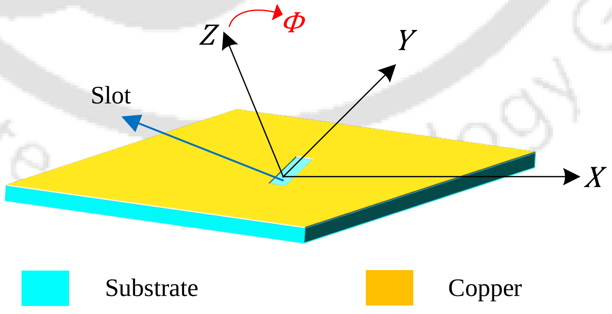

Fig. 1.2: Planar slot antenna on a substrate

A microstrip-fed planar slot antenna (shown in Fig. 1.2) consists of a slot cut out of a ground plane backed by a substrate (can be even air) such that the slot is perpendicular to the microstrip feed-line and its fields excite the slot. The major advantages are large bandwidth, less conductor losses, and economic utilization of space [?]. The slot antenna can be viewed as the complement of a planar dipole antenna whose far-field equations are produced here [76]

$$\vec{E}\left(r,\theta,\phi\right) = I_{in}\frac{\exp\left(-jk_0r\right)}{r}\frac{j\eta_0 l}{2\lambda_0}\sin\left(\theta\right)\hat{a}_\theta \tag{1.1}$$

$$\vec{H}\left(r,\theta,\phi\right) = I_{in}\frac{\exp\left(-jk_0r\right)}{r}\frac{jl}{2\lambda_0}\sin\left(\theta\right)\hat{a}_\phi \tag{1.2}$$

where I_{in} is the input current, l is the length of the dipole, λ_0 is the wavelength of the excitation and η_0 is the free-space impedance. Moreover, the expressions for power density P_D and power per unit solid-angle p_d are given as [76]

$$P_D\left(r,\theta,\phi\right) = \frac{\left|\vec{E}\left(r,\theta,\phi\right)\right|^2}{2\eta_0} = \left|I_{in}\right|^2\frac{\eta_0}{8r^2}\left(\frac{l}{\lambda_0}\right)^2\sin^2\left(\theta\right) \tag{1.3}$$

$$p_d\left(\theta,\phi\right) = r^2P_D\left(r,\theta,\phi\right) = \left|I_{in}\right|^2\frac{\eta_0}{8}\left(\frac{l}{\lambda_0}\right)^2\sin^2\left(\theta\right) \tag{1.4}$$

The total radiated power from the dipole antenna for a given input antenna I_{in} is given by

$$P_{rad} = \int_{\phi=0}^{2\pi}\int_{\theta=0}^{\pi} p_d\left(\theta,\phi\right)\sin\left(\theta\right)\, d\theta\, d\phi = \frac{\left|I_{in}\right|^2}{8}R_r \tag{1.5}$$

where R_r is the radiation resistance whose expression for a dipole antenna is

$$R_r = 80\pi^2\left(\frac{l}{\lambda_0}\right)^2 \tag{1.6}$$

The rigorous mathematical derivation of these equations may be found in [?]. As stated earlier, since slot antenna is a complementary dipole antenna, its far-field equations may be derived by the following steps [76]

(i) replace $\vec{E}\left(r,\theta,\phi\right)$ with $-\vec{H}\left(r,\theta,\phi\right)$, ε_0 with μ_0, $\vec{H}\left(r,\theta,\phi\right)$ with $\vec{E}\left(r,\theta,\phi\right)$, I_{in} with $2V_S$ and η_0 with $\frac{1}{\eta_0}$ for the top region of the slot antenna ($z > 0$) (as shown in Fig. 1.2)

(ii) for the $z < 0$ region, no substitution is needed other than reversing the signs of the field expressions

Therefore the far-field E- and H-components of the slot antenna are

$$\vec{E}\left(r,\theta,\phi\right)=\begin{cases} V_S\dfrac{\exp\left(-jk_0r\right)}{r}\dfrac{jl}{\lambda_0}\sin\left(\theta\right)\hat{a}_\phi & z>0\\ -V_S\dfrac{\exp\left(-jk_0r\right)}{r}\dfrac{jl}{\lambda_0}\sin\left(\theta\right)\hat{a}_\phi & z<0\end{cases} \tag{1.7}$$

$$\vec{H}\left(r,\theta,\phi\right)=\begin{cases} -V_S\dfrac{\exp\left(-jk_0r\right)}{r}\dfrac{jl}{\eta_0\lambda_0}\sin\left(\theta\right)\hat{a}_\theta & z>0\\ V_S\dfrac{\exp\left(-jk_0r\right)}{r}\dfrac{jl}{\eta_0\lambda_0}\sin\left(\theta\right)\hat{a}_\theta & z<0\end{cases} \tag{1.8}$$

Using the above two expressions, the expressions for power density P_D and power per unit solid-angle p_d may be written as

$$P_D\left(r,\theta,\phi\right)=\left|V_S\right|^2\frac{1}{2\eta_0r^2}\left(\frac{l}{\lambda_0}\right)^2\sin^2\left(\theta\right) \tag{1.9}$$

$$p_d\left(\theta,\phi\right)=r^2P_D\left(r,\theta,\phi\right)=\left|V_S\right|^2\frac{1}{2\eta_0}\left(\frac{l}{\lambda_0}\right)^2\sin^2\left(\theta\right) \tag{1.10}$$

Finally, the total radiated power P_{rad} of the slot antenna is obtained from its radiation resistance R_r can be given as

$$P_{rad}=\int_{\phi=0}^{2\pi}\int_{\theta=0}^{\pi}p_d\left(\theta,\phi\right)\sin\left(\theta\right)\,d\theta\,d\phi=\frac{\left|V_S\right|^2}{2R_r} \tag{1.11}$$

It is obvious from the above expressions that slot antennas have a bi-directional radiation pattern with a significant back-lobe that is the main cause behind low gains of such antennas. To remedy this drawback, several methods to suppress the back-lobe have been suggested viz. usage of metallic reflectors [?], cavity backing, [?, 18], and superstrates [?].

1.4.1 Polarization

This section elaborates some of the terms commonly associated with CP and the justification behind designing CP antennas which is followed by the measurement techniques of various parameters of CP antennas (axial ratio, gain etc.) that are discussed in depth.

1.4.2 Circular Polarization

The term *polarization* for an electromagnetic (EM) wave is related to the direction of its associated electric field (E-field) [76]. In other words, the geometric shape described by the tip of the E-field vector in a plane determines the polarization. For circular polarization, the tip of the field vector is seen to rotate describing a circle. The different cases of polarization along with their mathematical forms may be found in Appendix A.2.

The general expression of a plane EM wave is written as

$$\vec{E}\left(z,t\right)=\left(\hat{x}E_{x0}+\hat{y}E_{yo}\right)\exp\left(-j\left(kz-\omega t\right)\right) \tag{1.12}$$

The relationship between E_{0x} and E_{0y} determines the polarization of the wave. Therefore, if for instance, either of the components is 0 the wave is said to be linearly polarized along the other axis. On the other hand, suppose $E_{0y}=jE_{0x}$, then the real part of the field equation in (1.12) may be written as

$$\vec{E}\left(z,t\right)=\mathrm{Re}\left[E_{0x}\exp\left(-j\left(kz-\omega t\right)\right)\right]\hat{x}+\mathrm{Re}\left[E_{0x}\exp\left(-j\left(kz-\omega t\right)\right)e^{j\pi/2}\right]\hat{y} \tag{1.13}$$

$$=E_{0x}\left[\cos\left(kz-\omega t\right)\hat{x}-\sin\left(kz-\omega t\right)\hat{y}\right] \tag{1.14}$$

Thus, since the X-field component leads the Y-field component by $\pi/2$, the strength of E-field never becomes null in two planes simultaneously and the tip of the field vector is seen to rotate describing a circle. This is the case of circular polarization.

1.4.3 Faraday rotation effect

Faraday rotation effect is the outcome of a linearly polarized EM wave interacting with an applied magnetic field in a medium when its relative permittivity is in the form of a tensor. This phenomenon causes a rotation in the plane of polarization of the EM wave by an angle proportional to the intensity of the magnetic field because of different refractive indices experienced by the components of the LP wave. This rotation angle (complete expression may be found in Eq A.46 of the Appendix derived in A.3 and A.4) is also dependent upon the wavelength λ and the dispersion in the medium $\frac{dn\left(f\right)}{d\lambda}$. Therefore, a plane polarized wave, which is a linear sum of a right-hand and a left-hand wave, will rotate as it propagates. Hence it is clear that the effect is more pronounced at the lower frequencies. It is to be noted that CP antennas are inherently resistant to this phenomenon [3] because of which they are preferred in satellite communications

1.4.4 Multipath effect

A transmitted signal may be reflected by the ground, buildings and other obstacles. This may cause the signal to arrive multiple times or delayed at the receiver end [?] and is termed as multipath. The effect of multipath on an RHCP antenna is denoted mathematically by multipath ratio (MPR) that is given as [?]

$$MPR = \frac{G_{RHCP}\left(\theta\right)}{G_{RHCP}\left(180^\circ - \theta\right) + G_{LHCP}\left(180^\circ - \theta\right)} \tag{1.15}$$

Here G_{RHCP} and G_{LHCP} are the RHCP and LHRP gains (i.e., the antenna gain of co-polarized and cross-polarized components) of the radiated field from the antenna and θ is elevation angle in degrees. In antennas where the back-lobe (LHCP mode) points to the ground, the cross-polarization discrimination (XPD) should be low for a high MPR. A CP antenna is useful in combating multipath effects. This is because, a reflecting surface transforms RHCP to either LHCP or linear polarization that is rejected by an antenna tuned to receive RHCP.

1.5 Experimental measurement techniques in CP antennas

1.5.1 Measurement of AR

Toh et al [?] present a method to measure AR of CP antennas using a standard LP horn by utilizing the fact that the horizontal and vertical components of the E-field i.e. $\vec{E}_H$ and $\vec{E}_V$ are equal in magnitude and are in phase-quadrature (±90°). The final expressions of E-field for RHCP and LHCP (derived in Appendix A.5) can be written as

$$E_{RHCP} = \frac{1}{\sqrt{2}}\left\{\left[\vec{H}_A\cos\left(H_P\right) + \vec{V}_A\sin\left(V_P\right)\right] + j\left[\vec{H}_A\sin\left(H_P\right) - \vec{V}_A\cos\left(V_P\right)\right]\right\} \tag{1.16}$$

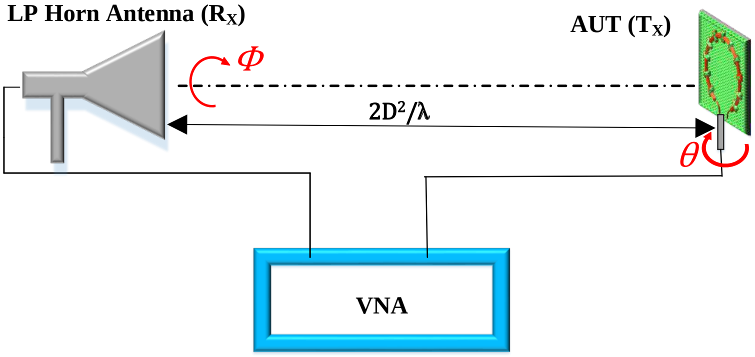

Fig. 1.3: Experimental set-up for AR measurement. (AUT: antenna under test)

and

$$E_{LHCP} = \frac{1}{\sqrt{2}}\left\{\left[\vec{H}_A \cos\left(H_P\right) - \vec{V}_A \sin\left(V_P\right)\right] + j\left[\vec{H}_A \sin\left(H_P\right) + \vec{V}_A \cos\left(V_P\right)\right]\right\} \tag{1.17}$$

where ($\vec{H}_A$, $\vec{V}_A$) are the horizontal and vertical amplitude components and ($\vec{H}_P$, $\vec{V}_P$) are their respective phase-angles.

For each sense of polarization, the power is given by

$$P_{CP} = 10\log_{10}\left(\frac{E^2}{377}\right) \tag{1.18}$$

The cross-polar power (in dB) is calculated as

$$P_{dB} = P_{RHCP}\left(dB\right) - P_{LHCP}\left(dB\right) \tag{1.19}$$

Once the value of P_{dB} is known, the AR is determined from the following equation

$$AR = 20\log_{10}\left(\frac{1+\kappa}{1-\kappa}\right) \tag{1.20}$$

where $\kappa = 10^{-P_{dB}/20}$.

1.5.2 Measurement of gain

The gain of the AUT which is denoted by G_T is measured by using a standard circularly polarized horn antenna (of gain G_R) using Frii's transmission formula [2] from the following equation

$$\frac{P_R}{P_T} = \frac{G_R G_T}{L_C} \left(\frac{\lambda}{4\pi R} \right)^2 \tag{1.21}$$

Here, L_C is the loss due to cables, λ is the wavelength at the frequency of operation, and R is the distance between two antennas which should be in the far-field region. The ratio of P_R to P_T is directly read from the Vector Network Analyzer (VNA) (in dB). By rearranging the above relation in logarithmic form and defining path-loss $P_L = \left(\frac{\lambda}{4\pi R} \right)^2$, G_T is calculated by

$$(G_T)_{dB} = 10 \log_{10} \left(\frac{P_R}{P_T} \right)_{dB} + 10 \log_{10} (L_C)_{dB} - (G_R)_{dB} - 20 \log (P_L) \tag{1.22}$$

It is to be noted that for an accurate gain measurement, the polarization sense of both the AUT and the standard CP horn antenna must be the same.

1.6 Literature survey on circularly polarized planar antenna

Having seen the advantages of CP and planar antennas we now examine the literature on CP planar antennas i.e. CP microstrip antennas and CP slot antennas and discuss different techniques of feeding such radiators in the next two sub-sections. The different techniques of CP patch antenna miniaturization and AR bandwidth improvement through modifications in patch topology have been examined and discussed here.

1.6.1 Microstrip patch antenna

The easiest approach for realizing CP waves is to excite the patch by two spatially orthogonal feeds using a power splitter of unequal length [?]. However the patch can also be excited using a single feed by creating perturbations in the shape of the patch. In such a situation, two degenerate modes of equal amplitudes are created. By ensuring an asymmetry in the cavity, one mode will have a lower frequency whereas the other mode a higher one. With proper design, the phase of one mode will lead that of impressed current by 45° whereas the phase of the other mode will lag by the same amount creating an orthogonality [?].

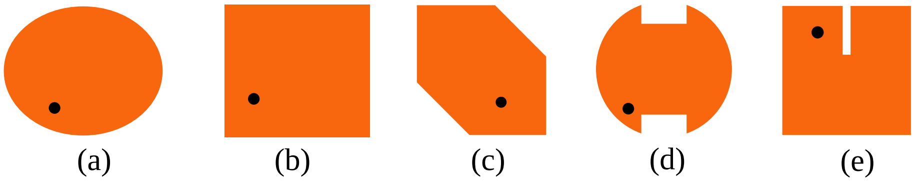

Fig. 1.4: Single-feed CP patch antenna configurations [3, 4]

Fig. 1.4 shows a few common single-feed CP patches. Here, the black dots represent the locations of feeds on the patches. Fig. 1.4(a) shows an elliptical patch that is excited in such a way to generate two orthogonal CP modes. If ξ is the ratio of the major axis to the minor axis of the patch, then ξ must satisfy the following relationship [3]

$$\xi = 1 + \frac{1.0887}{Q} \tag{1.23}$$

where Q is the quality factor of the antenna determined by the resonant frequency f_r, bandwidth Δf and VSWR of the antenna given as [3]

$$Q = \frac{f_r}{\Delta f}\frac{\text{VSWR} - 1}{\sqrt{\text{VSWR}}} \tag{1.24}$$

If the patch has a nearly square shape (as in Fig. 1.4(b)), its length L, and width W, are related by [3]

$$L = W\left(1 + \frac{1}{Q}\right) \tag{1.25}$$

where Q is given by (1.24). Fig. 1.4(c) depicts a common CP patch antenna whose opposite corners are truncated. The main drawback of this patch is its higher resonant frequency than that of a square patch because of which the former is not fit for antenna miniaturization [5]. The corresponding circular shape of the former is shown in Fig. 1.4(d). A modification of the patch of Fig. 1.4(b) is shown in Fig. 1.4(e) in which a slit is provided at the boundary for design optimization [4].

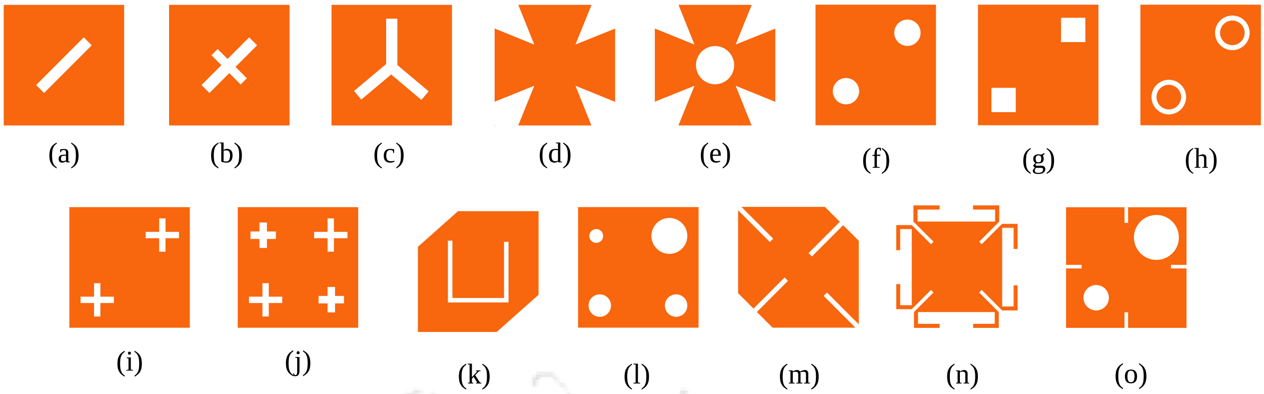

Fig. 1.5: Slots and slits in CP patch antenna [5–12]

CP patch antenna with slots and slits It is to be noted that addition of slots and slits to microstrip patches can aid in size-reduction [5–9], AR bandwidth augmentation [7], better impedance matching [10] and general ease of tuning for optimum performance [8]. Some of the common configurations of such slots and slits reported in literature are shown in Fig. 1.5. The patches shown in Fig. 1.5(a), 1.5(b) and 1.5(c) [5] are provided with slots of various shapes (tilted rectangular, cross and inverted Y-shaped respectively) that are useful in size reduction as the resonant frequency and AR band of the patches show a successive shift to the lower band. The presence of V-shaped slits to the corners (Fig. 1.5(d)), and an additional circular slot to the centre of the former (Fig. 1.5(e)), shifts the resonance further to a lower value of frequency. It is to be noted that the compactness comes at the expense of reduced impedance bandwidth, AR bandwidth and lower gain [5]. Nasimuddin et al [9] have presented a study of different types of diagonally-located slots (circular-, square-, annular- and cross-shaped as shown in Fig. 1.5(f), 1.5(g), 1.5(h), and 1.5(i) respectively) based on two slots. The study establishes that among all these shapes, a pair of diagonally-located crossed-slots is most preferable due to superior antenna compactness. For further miniaturization, two pairs of diagonally-located crossed-slots are suggested as shown in Fig. 1.5(j). In yet another work by Nasimuddin et al [8] , the authors have presented a CP patch antenna with four dissimilar slots for tuning and miniaturization as shown in Fig. 1.5(l). The same authors [6] have presented another slotted-patch antenna with a pair asymmetric circular slots in a patch that also has rectangular slits in the middle of its edges as shown in Fig. 1.5(o) for antenna size-reduction. Lam et al [7] present a probe-fed truncated-cornered patch antenna with U-shaped slot with superior AR and smaller patch size as shown in Fig. 1.5(k). The function of the U-shaped slot is to suppress the inductance of the probe by introduction of a capacitive reactance that broadens the AR bandwidth. In another truncated-cornered patch [11] a size reduction of 36% is achieved by the usage of four rectangular slits (Fig. 1.5(m)) by meandering the excited fundamental mode. The patch shown in Fig. 1.5(n) has slits and spur-lines or tails which increase the path of current for TM_{10} mode thus lowering the resonant frequency [12].

1.6.2 Planar slot antenna

CP slot antennas are preferred for their simple structures and relative ease of integration with microwave integrated circuit (MIC). They can also be cut out of the platform on which they are to be mounted. Fig. 1.6 shows some of the simplest dual-feed CP slot antenna configurations [3]. The slots can be of various shapes and are generally chosen as half the wavelength. The slots in Fig. 1.6(a) and 1.6(b) [3] are excited by means of Wilkinson power dividers whose longer arms are greater than the shorter ones by a quarter wavelength thus imparting a 90° phase difference between the feed-points. This generates two orthogonal modes and the slots radiate CP waves. Fig. 1.6(c) shows a square slot excited by means of two microstrip lines that terminate at a common end [13]. This configuration produces a wide AR and impedance bandwidth covering the WiMAX frequency band.

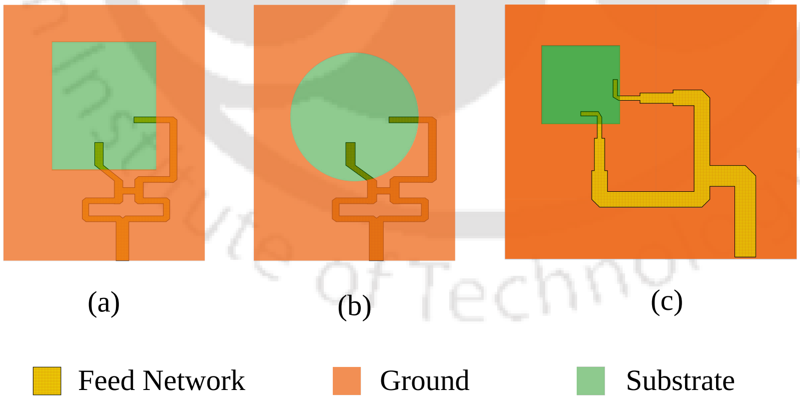

Fig. 1.6: Some common dual-feed CP slot antennas [3, 13]

All the structures described above have complicated shape and occupy too much of space that are undesirable in certain applications [3]. To overcome these drawbacks, CP slot antennas with single feeds are proposed, some of which are shown in Fig. 1.7. In Fig. 1.7(a), an L-shaped microstrip feed-line of quarter-wavelength is used to excite two orthogonal modes in a square ring-shaped slot to produce CP waves [3]. A dual-band CP antenna with U-shaped strip is presented in [14], in which the strip makes a 45° angle inside the slot as depicted in Fig. 1.7(b). The asymmetric feeding generates a 90° phase difference that creates CP. For wide-band operations, CP monopoles are ideal as reported in [15], in which an L-shaped slot ($\lambda/4$ length) cut at the corner of the ground plane is excited by a C-shaped microstrip line. A schematic of this antenna is given in Fig. 1.7(c). A coplanar waveguide (CPW) fed slot antenna with a T-shaped strip protruding from the ground (Fig. 1.7(d)) is presented in [16] that has high AR and impedance bandwidth. This study also gives the empirical design rules that have proven to be useful for designing similar types of antennas at other frequencies. A wide-band antenna suitable for wireless communication is proposed in [17] which has a shorting patch (inclined at 45° angle) joining the inner ring and the ground plane. In this design, impedance matching is accomplished by means of a meandered feed line with tuning stubs as shown in Fig. 1.7(e).

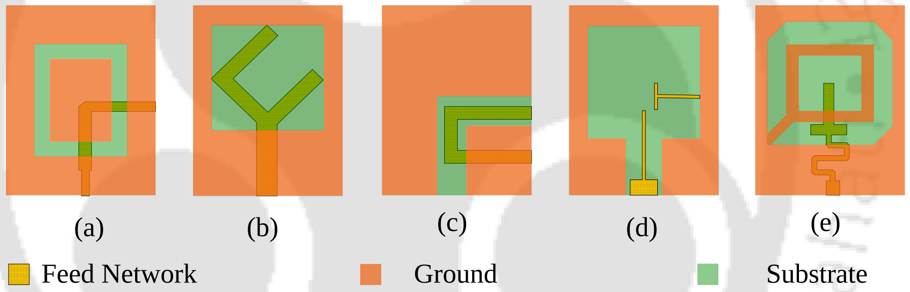
(a) (b) (c) (d) (e)

Fig. 1.7: Single-feed CP slot antennas [3, 14–17]

Finally, single-feed slot antennas that use split-ring resonators (SRRs) are discussed in brief. A proper selection of shape and dimensions of SRRs can be useful in yielding multiband operation in a CP slot antenna. When the SRRs are placed at the back of the antenna beneath the ground plane and the substrate, the perpendicular magnetic field of the slot antenna excites the SRR that acts as magnetic dipole which is responsible for the resonance at the higher band [18]. Kandasamy et al [18] have demonstrated this concept and have given the design of a slot antenna that resonates at two different frequencies. The antenna (schematic given in Fig. 1.8(a)) consists of a pair of conjoined SRRs and is backed by a metallic cavity to produce unidirectional lobe. Two dissimilar SRRs (with a single and multiple gaps) have been used in [?] and [20] (Figs. 1.8(b) and 1.8(c)) for producing second and third band in CP slot antennas.

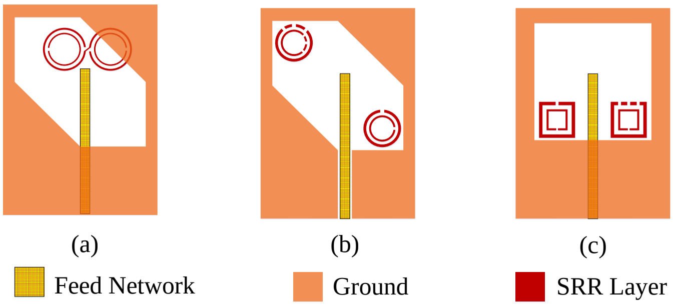
(a) (b) (c)

Fig. 1.8: Single-feed multiband CP slot antennas with SRR [18–20]

1.7 Planar spiral antennas

The planar spiral antenna is on of the traditional method of achieving CP performance in an antenna. The spiral antennas operate on the principle of scaling in which a radiating element is subjected to successive scaling about an axis, yielding structures which are identical with the original one. These antennas have the important feature of being broadband and have been extensively used in direction finding, ground penetrating radar and global positioning system [?]. The spirals, based on their geometry can be further classified as logarithmic spiral antenna [?, ?], equiangular spiral antenna [?, ?], archimedean spiral antenna [?, ?] and square spiral antenna [?] . Zamudio et al [?] present a wideband CP log-spiral antenna that is optically transparent and hence integrable with solar panels. The antenna is made up of a silver conductive film called AgHT and is intended for energy harvesting. Using multi-port network theory, the parameters of a planar logarithmic spiral antenna are derived assuming it to be made up of annular sector connected through ports in [?]. McFadden and Scott Jr. [?] present a study of planar equiangular spiral antenna with different substrates using the FDTD technique for modelling the spiral. In [?], a planar equiangular spiral antenna with embedded chip resistor for a high impedance bandwidth is discussed. Schreider et al [?] present an ultra-wideband planar archimedean spiral RHCP antenna with a very low profile. A wideband, miniaturized planar archimedean spiral antenna with moderate gain is discussed in [?]. Circular polarization can also be generated by spiral having non-curved edges as demonstrated in [?] where two radiating square spirals placed at different layers are capable of producing two types of CP waves (i.e. LHCP and RHCP) at two different frequencies.

The figure below Fig. 1.9 shows a few contemporary planar spiral antennas. In Fig. 1.9(a), a sequentially rotated archimedean spiral array with high gain of more than 10 dBic is presented [21]. The array also has a high impedance and AR bandwidth and is cavity-backed. The authors in [22] present a complementary two turns spiral antenna array that is designed to operate at two different bands at LHCP and RHCP as shown in Fig. 1.9(b). It has been demonstrated that spiral slots may be incorporated in the radiating elements to enhance the CP performance in antennas in [23–26]. Yang et al [23] present a circular patch antenna with four spiral slots for a dual-band CP operation as shown in Fig. 1.9(c). The slots perturb the fields in such a way that the resonant frequencies of the two orthogonal modes i.e. TM_{11} and TM_{12} are close to each other thereby producing CP. In [24], [25] and [26], the authors have presented CP antennas with CPW feeds having a pair of grounded spiral slots. The schematics of the slotted ground plane for these three antennas can be seen in Figs 1.9(d), (e) and (f).

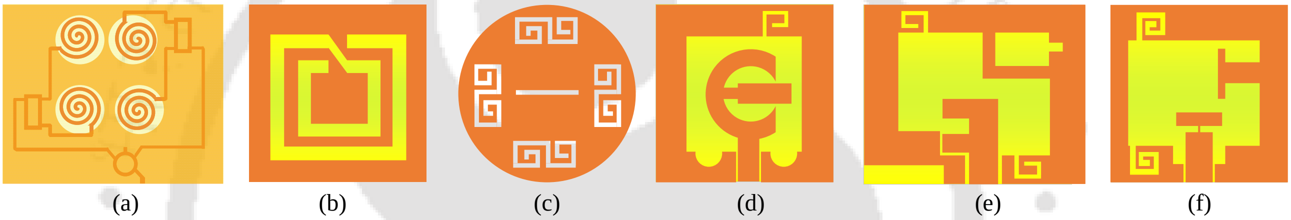
(a) (b) (c) (d) (e) (f)

Fig. 1.9: Examples of spiral CP antennas from the contemporary literature [21–26]

Even though, traditionally non-planar helical antennas have been used for CP generation [**?**], one such planar embodiment has been devised by Chen and Shen in [**?**].

The above discussion may be summarized as

- A corner-truncated patch antenna is not preferable for antenna miniaturization. However, addition of other geometric artefacts like slots and slits to such a patch can greatly improve its properties
- A careful design of a single-feed slot antenna can yield very wide impedance and AR bandwidth
- Usage of SRRs can greatly enhance the characteristics of a slot antenna
- Single-feed slot antennas offer much greater design flexibility of decoupling networks between the feed-lines

- Due to the bi-directional nature of its radiation pattern, the gain of a slot-antenna is quite low. This deficiency, however, can be overcome by various techniques as mentioned earlier.

- Addition of spirals can enhance the CP properties of an antenna

It needs mentioning that in some of the later chapters, detailed study on such single-feed microstrip patch and slot antennas with dual CP (DCP) configuration will be presented where we will examine the methods to maximize the interport isolation. It will also be shown that rows of properly designed SRRs can be used as band-stop filter to decouple the ports of a DCP slot antenna. A study of CP microstrip patch antennas with Defected Ground Structures (DGS) will also be presented.

The table 1.2 below gives the comparison between different feeding techniques in planar CP antennas in a nutshell whereas the comparison between different types of CP antennas may be found in table 1.1.

1.8 A background on MIMO antenna technology

Single-input-single-output (SISO) technology has fallen out of favour in modern wireless communication because of its low SNR, poor average signal to interference with noise ratio, and higher power per unit bandwidth requirements because of which it is unsuitable for gigabit-per-second wireless links in non-line-of-sight (NLOS) systems. Therefore the multiple-input-multiple-output (MIMO) technology is being adopted increasingly to cater to the high gain, data-rate and efficiency requirements [?, ?]. For example, in many communication systems like the 4G-enabled handheld devices 2 antennas are employed in MIMO configuration [?]. The assessment of MIMO performance is done on the basis of evaluation of certain parameters like envelope correlation coefficient (ECC) and diversity gain (DG) which are described in details.

Envelope correlation coefficient (ECC) - The ECC gives a measure of the diversity performance of a MIMO antenna [?] by providing a measure of channel correlation. The value of ECC is calculated using Eqn (4) of [?] and should be as low as possible for a high channel capacity as shown in [?]. It should be noted that the ECC calculated using the S-parameters

(Eqns (5) and (6) of [?]) is based on the fact that the antennas have an efficiency of 100%, a condition which is never met in practical situations.

Diversity gain (DG) - The diversity gain (DG) is a metric used for quantifying the performance of diversity techniques. The diversity techniques are employed to combat fading in wireless links by ensuring that different replicas of the same signal are sent to the receiver, so that the probability of all of them fading simultaneously is small. These signals can be sent over multiple independent paths, and therefore, by providing redundancy, the receiver is able to decode the transmitted signal. Therefore, DG is the gain of the received SNR because of diversity techniques [?].

1.9 Objective of the thesis

The objective of the thesis is to first understand what metrics of a dual circularly polarized antennas need to be improved upon. To this end, the mechanism of coupling in a two-port antenna is studied and the responsible factors of low port-isolation are identified. It is also established that, a high AR bandwidth, in conjunction with a very low port-coupling, is vital for a simple receiver in a transceiver system. In the next step, various port-decoupling techniques in dual linearly polarized antennas are studied. A review of a large number of dual circularly polarised planar antennas is presented which encompasses antennas of both types - single element antenna and series-fed arrays. The contributory chapters i.e. Chapters 4, 5, 6 and 7 present different types of DCP antennas designed by the author with the key objectives of - high AR bandwidth, high interport isolation, simplicity in feed and moderately high gain which are elaborated under the next section **Organization of the Thesis.**

1.10 Organization of the thesis

With this introduction, the remaining part of the thesis is organized and arranged in the following manner:

Chapter 2 begins with a discussion on mechanism of electromagnetic coupling in patch antennas followed by a mathematical explanation of signal interference and its dependence on port-decoupling and bandwidth. The last section is an evaluation of different techniques for augmenting antenna port isolation.

Chapter 3 presents an elaborate literature survey on planar DCP antennas which encompasses DCP slot antennas, DCP antenna arrays, multilayer DCP antennas and DCP antennas for various applications like MIMO communication and energy harvesting. The last section introduces a rarer kind of DCP antennas called travelling-wave antennas which are a type of series-fed arrays.

Chapter 4 presents a DCP slot antenna in which inter-port isolation has been boosted using an interdigital capacitor connecting the antenna ports. This chapter elucidates the design equations, CP mechanism and the sensitivity of various antenna parameters on its performance followed by discussion on measured data.

Chapter 5 discusses a shared-aperture DCP slot antenna consisting of a split-ring resonator based metasurface describing the detailed design process of the aperture, feed-lines and the metasurface. This chapter also presents a comparison of different substrates by evaluating their effect on antenna gain and suggests a method to improve the gain.

Chapter 6 presents a patch antenna with a multifunction DGS where the latter plays a vital dual role in port-decoupling and reducing cross-polarization.

Chapter 7 elaborates on travelling-wave DCP antennas introduced in Chapter 3. The chapter begins with an analytical understanding of such antennas followed by a novel DCP travelling-wave slot antenna array.

The concluding remarks stressing on the applications of the designed antennas in the preceding chapters followed by exploration of avenues of future work in this domain have been presented in Chapter 8.

Table 1.1: Comparison of different radiators implemented in CP antennas

Radiator type	Features	Geometry	Advantages	Disadvantages
Microstrip patch	• Rectangular patch with truncated corner • Feed (dual or single) is placed asymmetrically	Planar and simple	• Large variety of shapes can be designed • Good FBR	• Narrowband • Low gain • Higher XPD • Low efficiency
Slotted ground	• Has a slot cut out of ground plane • Excited by microstrip line	Planar and simple	• Wider bandwidth • Low XPD • Low Conductor loss • Low profile	• Low gain • Presence of back-lobes
Spiral	Modified dipole antenna where arms are wrapped around each other	Planar and moderately complex	• Frequency independent • Bandwidth as high as 30 : 1 • Inherently CP • CP behaviour over a wide bandwidth	Complicated feed network
Helical	• Consists of conducting wire wound as helix • Operates in two modes – normal and axial	Non-planar and simple	• High directivity • Wide bandwidth • Inherently CP	• Bulky • Efficiency reduces with increasing number of turns

Table 1.2: Comparison of different feed-types in planar CP antennas

Feed type	**Features**	**Simplicity**	**Volume**	**AR**	**ARBW**
Single-feed	• Two degenerate modes are excited • Feed is placed asymmetrically • One mode leads whereas other mode lags • Net orthogonality is created between the modes	Simple	Compact	Moderate	Low
Dual-feed	• Two orthogonal edges of patch are excited • Feeding done by two orthogonal microstrip lines • Done using Wilkinson's power divider, 90° hybrid coupler, 120° phase-shifter	Moderately complex	More voluminous	Low	High
Series-fed array	• Radiating elements are successive fed • Energy radiated by n^{th} element depends upon its distance from feeding port • Beam-direction changes with frequency • Useful in satellite communication	Simple	Compact	Low	High
Sequential rotation	• Phase angle of n^{th} element (out of N elements) is $\frac{2*\pi*(n-1)}{N}$ • Can be applied to all elements or subarrays • Have been used in combination with other feeds	Complex	Bulky	Low	High

2

Study of EM coupling in two-port antennas

This chapter discusses the challenge in designing two-port antennas by describing the mechanism of electromagnetic coupling between antenna ports. A justification for having high port-to-port isolation and broad bandwidth is given mathematically that clearly shows the sufficiency of a simpler transceiver if the first two conditions are met. Thereafter, some commonly known methods of port decoupling in two-port planar antennas are discussed. Lastly, examples of planar dual circularly polarized antennas from the contemporary literature are discussed which encompass slot antennas, multi-layer antennas, CPW-fed antennas, cavity-backed antennas, and antenna arrays. It is pointed out that further enhancement of port-to-port isolation in dual circularly polarized antennas need to incorporate the concepts of port-decoupling discussed here.

2.1 Electromagnetic coupling in antennas

In-band-full-duplex (IBFD) technology holds tremendous potential in wireless communication as it has the capability to improve network throughput. Especially, in military radios, this technique can be used to disrupt enemy communication while at the same time, continue to receive the intended signals [?]. Furthermore, IBFD can be used to build radios with compact and lighter filters [?]. However, the main challenge in realization of IBFD is the self-interference (SI) of the transmitter, which being orders of magnitude higher than the receiving signal, tends to suppress the latter [?]. For selecting a proper method of suppressing SI, it is necessary to understand how electromagnetic coupling (EMC) occurs between antennas. Niroo-Jazi et al [27] have identified four types of waves that come into play between two coaxial probe-fed patches of a two-port antenna (Ports P_1 and P_2) separated by a distance, as shown in Fig. 2.1

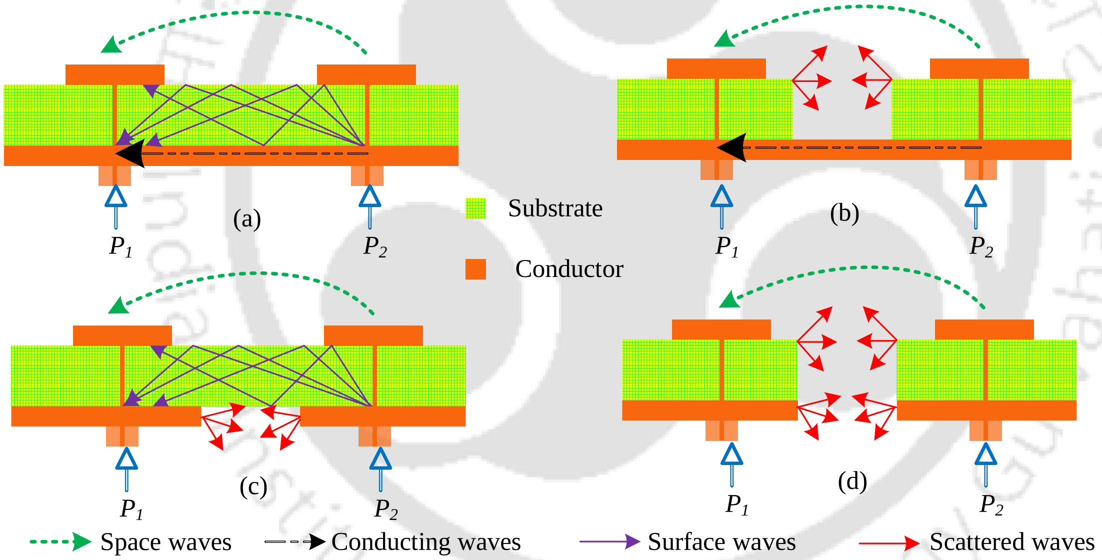

Fig. 2.1: Mechanism of EM coupling in a dual-port antenna with two patches [27]

When the patches share the same substrate and the ground-plane (Fig. 2.1(a)) the EMC is the strongest, causing low port-to-port isolation as in this case the electromagnetic interaction happens due to space-waves, surface-waves (trapped in the substrate), and conducting waves. The isolation improves slightly when the patches are made to share different substrates on the same ground-plane (Fig. 2.1(b)) as the surface-waves no longer have any effect, though the scattered waves from the edges of the substrates still cause undesirable coupling. Keeping the ground-planes separate while having the same substrate for the patches (as in Fig. 2.1(c)) eliminates the effects of conducting waves that have an important role in port-decoupling. Finally, if the two patches are placed on separate substrates and ground planes, surface waves and conducting waves are totally absent that yields lowest EMC. It should, however, be noted that the most significant contribution towards EMC is by space-waves and lateral waves (due to both surface- and conducting-waves). The effects of the former (i.e. the space-waves) can be eliminated by ensuring that the patches are tuned to two orthogonal polarizations whereas a large number of methods have been devised to mitigate the role of the latter.

A two-port dual-polarized (DP) antenna can be used in IBFD communication provided that the inter-port isolation is high enough to prevent the SI from saturating the receiver apart from having a broad bandwidth. These features of such an antenna will ensure simpler transceiver design by lower SI cancellation (SIC) requirement as demonstrated in [?, ?]. The received noise power P_N is given by [?]

$$\mathrm{P_N} = -174\,\mathrm{dBm} + 10\log_{10}(BW) + \mathrm{NF} \tag{2.1}$$

Assuming the T_X signal power to be P_T, the required SIC is: $P_{SIC} = P_T + P_N$. A portion of this P_{SIC} is provided by the antenna port-to-port isolation ($|S_{21}|_{dB}$), whereas the remaining is taken care of by the receiver. Therefore if the antenna bandwidth BW and $|S_{21}|_{dB}$ are large enough, a simpler receiver can be realized.

Moreover, a DP antenna offers a higher diversity gain and lower output correlation in contrast with conventional slanted dipole antennas used in cellular base-stations [?] and allow frequency reuse. DP antennas are also used in MIMO systems [?] for their superior performance in Rayleigh fading channels [?]. If used in radar systems [?], such antennas should have low cross-polarization levels or high cross-polarization discrimination (XPD).

2.2 Methods to improve port-to-port isolation

Since the inter-port isolation should be very high for DP or two-port antennas, a large number of techniques have been proposed to augment the isolation between the ports of such antennas. This section discusses some of the common ones and examines their merits and demerits.

2.2.1 Excitation of orthogonal modes

The most straightforward way to have a spatially orthogonal feed is to excite two orthogonal polarizations. The main advantages of this approach are its relative simplicity and a higher capacity offered. Some of the DP antennas with orthogonal feeds are shown in Fig. 2.2.

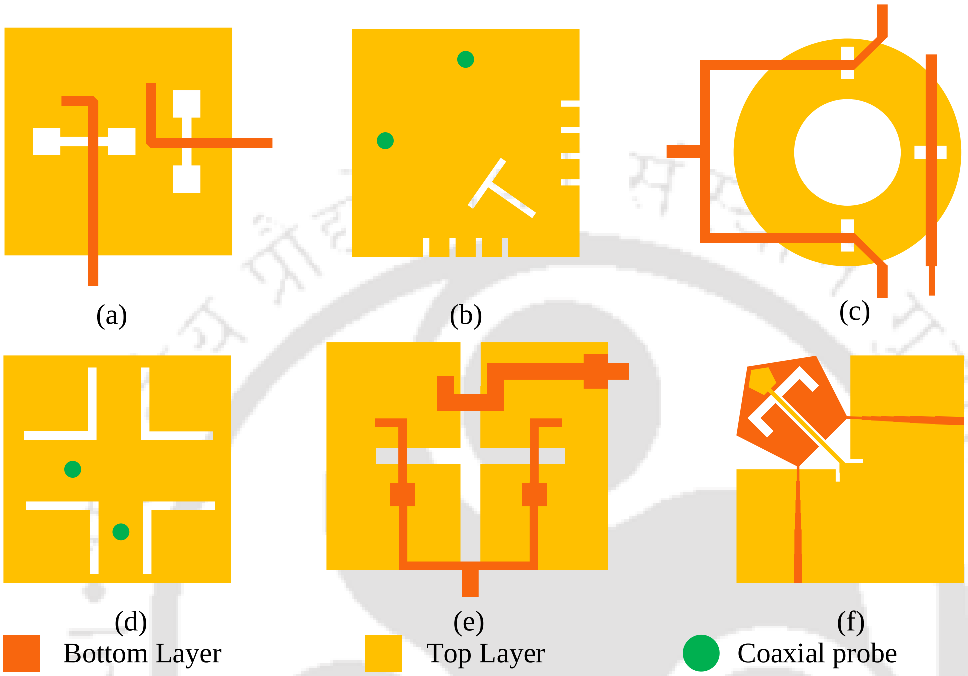

Fig. 2.2: Orthogonal feeding techniques in dual-polarized antennas [28–33]

A DP antenna with two H-shaped apertures (Fig. 2.2(a)) on one of the radiating patches of a (dual linearly polarized) DLP antenna consisting of two radiators is proposed in [28]. The major advantages of this antenna are its broad bandwidth (≈ 21%), high port-to-port isolation (> 36 dB), high XPD (> 22 dB) and low back-lobe (< −21 dB). Zaman et al [29] present a probe-fed DLP antenna with two patches in which the lower patch has a T-shaped slot in the middle and rectangular edge-slots to decouple its ports, as shown in Fig. 2.2(b). With this configuration, a bandwidth of 7.62%, inter-port isolation > 23 dB and XPD > 16.5 dB in the broadside direction are obtained. An annular ring-shaped aperture-coupled patch antenna with two orthogonally spaced feeds (Fig. 2.2(c)) is given in [30] whose impedance bandwidths are 1.3% and 1.9% and port-to-port isolation > 19 dB. The main drawbacks of this design are low bandwidths and different resonant frequencies for different ports. In [31], a DLP patch antenna with 4 L-shaped symmetric slots (Fig. 2.2(d)) is discussed whose XPD is 23 dB and inter-port isolation is 35 dB. The role of the slots is to aid in antenna miniaturization by imparting perturbations in the current paths and hence meandering them. Lindmark [32] presents a cross–slot shaped DLP patch antenna in which shunt capacitive tuning is applied to one of the ports (Fig. 2.2(e)) for impedance matching with fairly large bandwidths (13.7% and 17.5%) and good isolation (> 30 dB) between the ports. In one of the more recent antennas of such type [33], high isolation between ports is achieved by a T-shaped slot in one of the radiators and extending a branch of the slot to the axis of the radiator and co-radiator as shown in Fig. 2.2(f). The same design has been modified slightly to devise a 4-port MIMO antenna (not shown here) in the latter part of the same paper.

It may be inferred that in these designs, the effect of space-waves is minimized to a large extent by employing orthogonality, though the surface waves could not be mitigated. This leads the researchers to look for other alternatives that aim to reduce interference between ports by attenuating the surface-waves between them.

2.2.2 Usage of Electromagnetic Band Gap (EBG)

EBGs are useful in mitigating the effects of near-field radiations and thus suppress surface-waves [?]. In recent times, many types of EBGs have been fashioned to maximize isolation between antenna ports, some of which can be seen in Fig. 2.3.

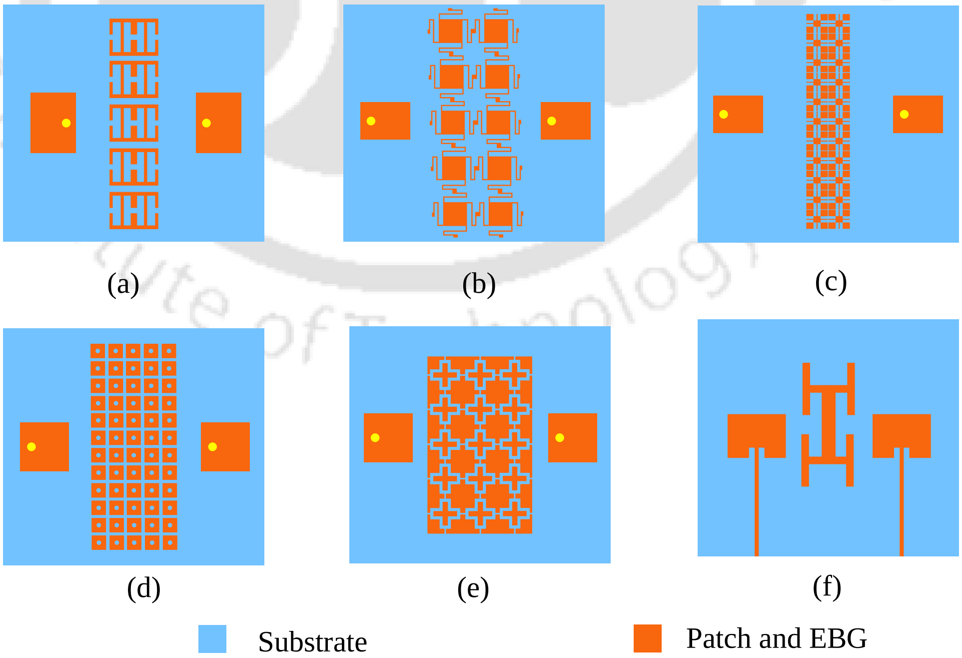

Fig. 2.3: Different types of EBGs in dual-polarized antennas [34–39]

A 5-unit cell EBG is placed between two patches that improves the isolation between the latter by up to 21 dB in [34] as shown in Fig. 2.3(a). In [35], a double-folded 5×2 EBG shown in Fig. 2.3(b) is presented that offers up to an additional 17 dB improvement in inter-port isolation. The purpose of the folds is to lengthen the effective paths for electric and magnetic currents thus increasing the net inductance and capacitance which lower the resonant frequency. To reduce the unwanted interference between antenna elements and EBG, the latter is placed in a separate layer above the patches (Fig. 2.3(c)) that also acts as a superstrate as in [36]. With this set-up, an improvement of 11 dB in interport isolation and 1.3 dB in directivity is observed. Fu et al [37] report an increase of 6 dB inter-port isolation by placing a 5×12 EBG (Fig. 2.3(d) whose unit cells are mushroom-shaped and where each such cell has a vertical metallic via at its centre. Assimonis et al [38] propose several EBGs based on different types of unit-cells out of which a 3×5 array of cross-shaped unit cells (shown in Fig. 2.3(e)) is placed between two probe-fed patches that imparts an additional 15 dB isolation at resonance. An EBG comprising two conjoined H-shaped unit cells is placed between two patches (as in Fig. 2.3(f)) for an extra 16 dB isolation by the authors in [39].

It needs to be mentioned that properly designed EBGs are capable of blocking undesirable surface waves at all incident angles and polarizations, though their greatest drawbacks are narrow bandwidths [36] and unsuitability at low frequencies [35]. This is because, due to their periodic nature, they occupy large physical space that makes it hard to enforce no grating-lobe condition.

2.2.3 Usage of Neutralization Line (NL)

In this technique, a thin conducting strip is used to connect two antenna elements in such a way that the field-lines generated in the elements oppose the ones produced by the existing coupling thereby reducing the latter [40]. This method is useful in applications like wireless USB-dongle [41], where very less board space is available to accommodate a decoupling network.

Fig. 2.4. shows a few recent 2-port antennas utilizing this method for port-decoupling. One such antenna for the aforementioned wireless USB-dongle [40] consists of two symmetric monopole antennas placed on a common substrate (Fig. 2.4(a)). The NL maneuvering the edge joins the two antenna elements (Fig. 2.4(a)) yields additional isolation of 15 to 30 dB in the impedance bandwidth. Another antenna for a similar purpose and having a similar structure

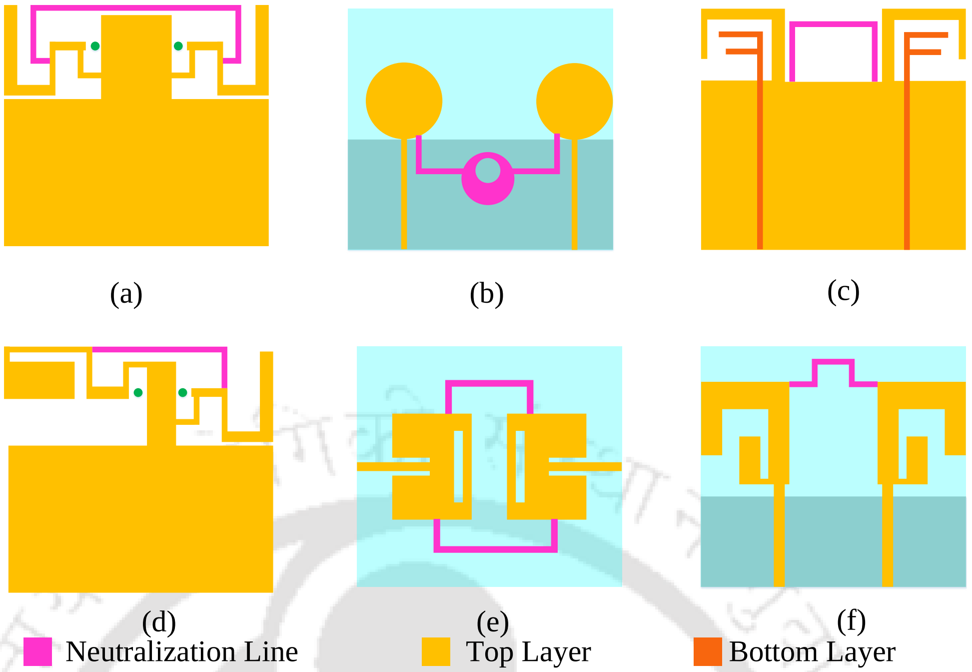
(a) (b) (c)

(d) (e) (f)

Fig. 2.4: Different types of NLs in dual-polarized antennas [40–45]

is presented by Su et al [43] (Fig. 2.4(d)) in which the NL contributes 10 dB of extra isolation. Even though NLs generally operate over a narrow bandwidth, Zhang and Pedersen [41] present an NL consisting of two metal strips and a circular disc (as shown in Fig. 2.4(b)) to reduce EMC between two monopoles that augments the interport isolation by 12 to 25 dB over a wide bandwidth ranging from 3.1 to 5 GHz. Another wideband antenna (1.6 to 3.2 GHz) employing NL is presented in [42] (as shown in Fig. 2.4(c)) in which an antenna element is formed of F-like monopole, and a grounded branch shows an isolation improvement of 10 to 15 dB due to the NL. One example of an application of the NL technique in a dual-band antenna is demonstrated in [44] in which two slotted inset-fed patches are joined by two NLs of varying lengths for different frequency bands. A schematic of this set-up is shown in Fig. 2.4(e). The NL in [45] shows a wide-band action by providing an extra 15 dB isolation in a dual-band antenna that has two C-shaped monopoles. The schematic of this configuration is shown in Fig. 2.4(f).

The NL technique requires a simple geometry and lesser space, thus finding its utility where other complicated methods cannot be used. However it is limited by its usual effectiveness over a narrowband, though broadband operations can be accomplished by substantially larger NLs.

2.2.4 Usage of Defected Ground Structure (DGS)

Etched patterns on the ground, called DGS, exhibit bandstop property that has been suggested for decoupling antenna ports [46–51]. The DGS may have a single unit cell or a number of such cells that may be similar or dissimilar [?]. The DGS causes a perturbation in the EM fields in its vicinity thus trapping the E-fields and surface-currents. In addition, various losses in conductor and dielectric is represented by an equivalent resistance R. Thus a realistic lumped element model of a DGS is an RLC-parallel circuit in which the circuit components are determined from the S-parameters of the DGS. However, there exists no closed form mathematical expression to extract the lumped element parameters directly for an arbitrary DGS and the former can only be computed from S-parameters through full-wave simulation [?].

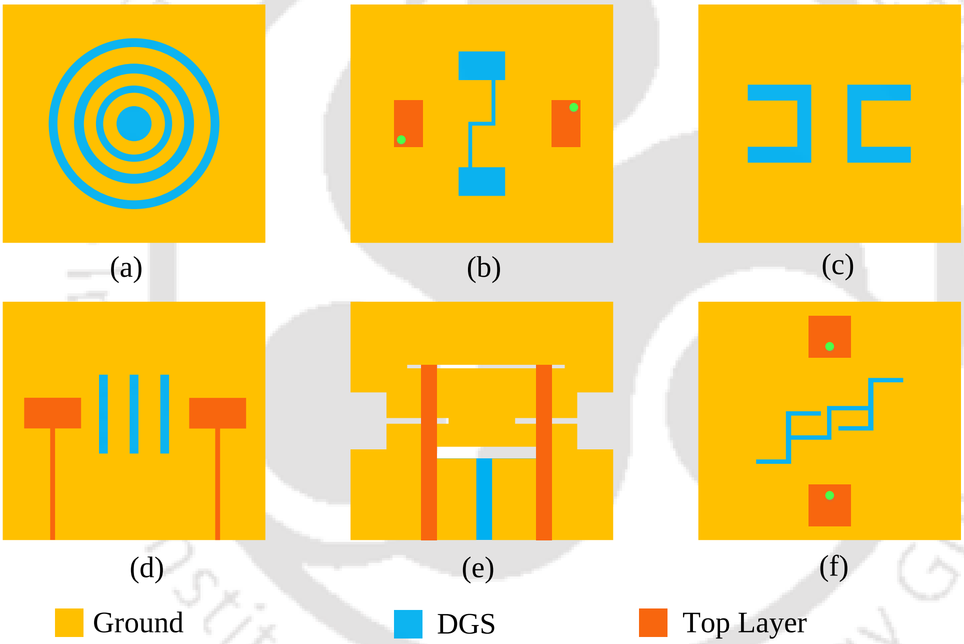

Fig. 2.5: Different types of DGS in dual-polarized antennas [46–51]

Guha et al [46] present different types of DGSs based on sets of concentric ring-shaped patterns on the ground-plane out of which one is shown in Fig. 2.5(a). All these patterns show wide stopband characteristics centred at 10 GHz and each has been tested with a secondary ground-plane backed substrate behind them to mimic an antenna. Zhu et al [47] present a dumb-bell shaped DGS shown in Fig. 2.5(b) to reduce EMC between two PIFAs that provides 17.43 dB greater isolation than without. The authors in [48] present a back-to-back U-shaped DGS (as shown in Fig. 2.5(c)) that reduces the mutual coupling at the cost of poorer front-to-back ratio (FBR) and higher sidelobe levels (SLLs). In [49], the authors have presented a simple DGS consisting of 3 rectangular slots on ground-plane (Fig. 2.5(d)) that aid in port-decoupling by a reduction of 16.5 dB in EMC. An even simpler DGS is proposed by Luo et al [50] in which a rectangular slot on the ground plane as shown in Fig. 2.5(e) is instrumental in reducing the EMC between two ports of a UWB-MIMO antenna. Wei et al [51] have demonstrated that a fractal DGS (Fig. 2.5(f)) greatly improves the interport isolation (> 30 dB) apart from playing a minor role in increasing antenna efficiency and cross-polar power.

Since the DGS technique concerns only the ground plane, the feed-lines or the radiating patches are left undisturbed. Therefore, in contrast to the NL technique, the DGS has less effect on the original antenna impedance [50]. However, if DGS is to be used, optimum distance between the patches is vital for a good gain as inappropriate values of this parameter can give rise to spurious back-radiation that adversely impacts the gain [48].

2.2.5 Usage of Split-Ring Resonator (SRR)

Split-ring resonator (SRRs) and complementary SRRs (CSRRs) are resonant structures that interact with vertically polarized magnetic and electric fields. This property of these types of resonators is exploited to suppress mutual coupling between the elements of a multiport antenna. In one of the pioneering works of CSRR-based bandstop filters, Bait-Suwailam et al [?] have shown that because CSRRs have strong rejection characteristics in the band-gap zone, they can be etched on the ground-plane to attenuate surface-waves.

Fig. 2.6(a) shows a square SRR used to enhance isolation by 6.4 dB between two PIFAs as discussed in [52]. Habashi et al [53] propose a double row of folded SRRs (Fig. 2.6(b)) that provides up to 41 dB of additional isolation in the resonant bandwidth. Qamar et al [54] present 8 units of slot combined complementary SRR (SCCSRR) (Fig. 2.6(c)) on both the substrate and the ground plane for more up to 19 dB EMC attenuation between two probe-fed patches. Hsu et al [55] propose a square SRR based metamaterial that is arranged in H-shape to alleviate EMC between two L-shaped antenna elements coupled by a T-shaped branch, as shown in Fig. 2.6(d). A significant improvement in antenna isolation of 61 dB is seen by the usage of 3 CSRRs on the ground plane (Fig. 2.6(e)) in [56] though there is a slight decrease in the main-lobe radiation. Among the unusually shaped SRRs, a Labyrinth split-ring resonator (LSRR) that has μ- negative (MNG) property, is used to reduce the EMC between two meander-line

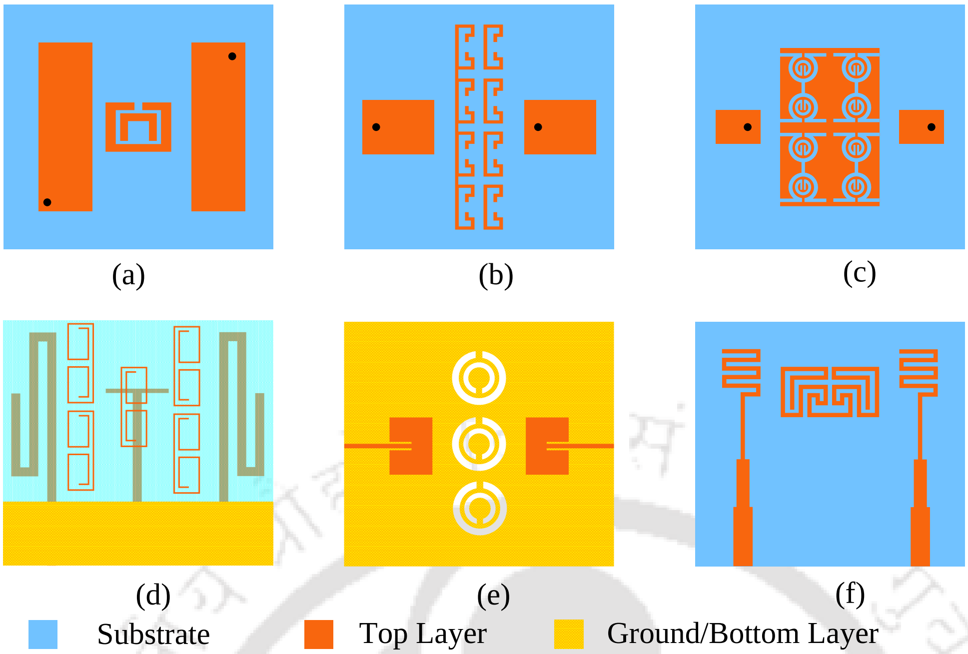

Fig. 2.6: SRRs/CSRRs and metamaterials for surface-wave mitigation [52–57]

antenna elements (Fig. 2.6(f)) by 39 dB as discussed in [57].

For the EMC reduction, employing SRRs/CSRRs has gained popularity because of their sub-wavelength size that requires very less physical space. Moreover, it has been observed that SRRs/CSRRs show sharper band-rejection than EBG and DGS [56]. Though, like the latter, due to the periodicity of SRRs, they tend to radiate EM energy, thereby reducing antenna gain [56].

2.2.6 Other methods

We now explore some of the remaining methods used to boost port decoupling. Most of these methods are either non-planar, thereby requiring complex fabrication, or are not easily implementable in case of antennas with more than two ports. The schematic of a few such methods is given in Fig. 2.7.

In [58], a high port-isolation is obtained by using a self-complementary geometry (Fig. 2.7 (a)) in which the orthogonally-placed antenna elements are fed perpendicularly. The important advantage of such a layout is its independence from any decoupling network. It has been shown in [?] that the inter-port isolation may be enhanced by introducing a net negative admittance

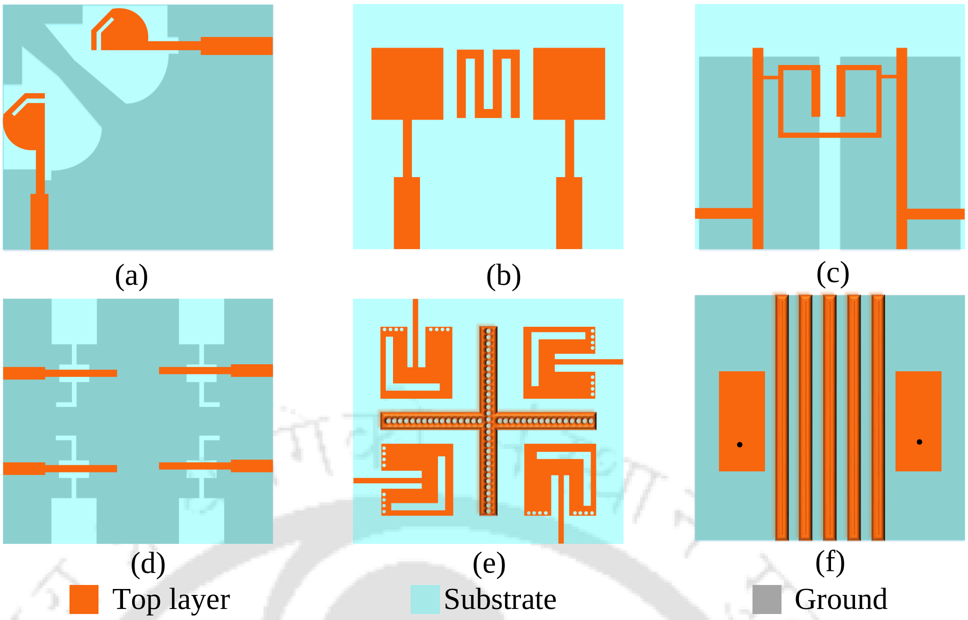

Fig. 2.7: Other methods for high port-to-port isolation [58–63]

of $-j\beta$ to cancel out the residual signal between the T_X and R_X ports. Using this concept, a meander line inductor is placed between the patches of [59] for greater port isolation as shown in Fig. 2.7(b). A mu-negative (MNG) metamaterial (MTM) based bandstop filter (Fig. 2.7(c)) is demonstrated to reduce coupling between DLP and DCP antennas in [60]. A high interport-isolation is achieved in a 4-port MIMO antenna (as shown in Fig. 2.7(d)) exploiting the directional radiation properties of slot antennas [61]. The next two designs use 3D metallic walls to separate patch antenna elements. To realize dual band operation, each of the rectangular patches has L-shaped slot etched at its edge. Boukarkar et al [62] have discussed the implementation of a cross-shaped metallic walls and strips shorted to the ground using vias for isolation enhancement between orthogonally arranged 4-element MIMO antenna, as shown in Fig. 2.7(e). The EMC between antenna elements may also be attenuated using a 3-D electromagnetic isolation wall (shown in Fig. 2.7(f)) by up to 29 dB as demonstrated by Jiao et al [63].

2.3 Summary

This chapter presents a study on the mechanism of mutual coupling between the ports of a two-port antenna. This apart, a vital mathematical equation relating noise-power P_N with the antenna bandwidth and interport isolation is presented which justifies a need for a very high value of the two latter quantities. These two sections form the motivational backbone for exploring port-decoupling methods in DCP antennas. In the next part of this chapter, a large number of port-decoupling techniques in DLP antennas are studied discussing their merits and demerits. Thus, a conclusion is drawn that for a DCP antenna with high port-isolation, orthogonal ports with a combination of one of the remaining technologies is worth exploring.

3

Dual circularly polarized antenna - a literature survey

This chapter discusses examples of planar dual circularly polarized antennas from the contemporary literature which encompass slot antennas, multi-layer antennas, CPW-fed antennas, cavity-backed antennas and antenna arrays. A section on a different type of antennas is dedicated to dual circularly polarized treavelling-wave antennas elaborating their advantages and applications. It is pointed out that further enhancement of port-to-port isolation in dual circularly polarized antennas need to incorporate the concepts of port-decoupling discussed here.

3.1 Planar dual circularly polarized antenna

Having seen the advantages of DCP antennas over DLP antennas in the previous chapter, we now focus our attention to the former and examine the state-of-the-art. It needs to be mentioned that most of the techniques for inter-port isolation enhancement discussed above are applicable to DCP antennas as well; though caution must be exercised while designing such antennas, as the AR being a delicate parameter, is sensitive to even minute changes in antenna geometry. It should also be noted that the term BW in (2.1) has to be replaced by the portion of the AR bandwidth BW_{AR} overlapping with the impedance bandwidth for DCP antennas.

In one of the first such papers on DCP antennas published by Hall [?], it was shown that a sequentially rotated array of notched circular patches could produce CP waves, though the main shortcoming is its high SLL. More recently, exploiting the odd and even modes of a co-planar waveguide, Narbudowicz et al [?] present a DCP antenna whose main limitation is its narrow AR bandwidth of only 1.3%. Lai et al [?] present a DCP antenna with H-shaped apertures excited using branch line couplers whose drawback is its high profile.

For vehicle-mounted satellite communication, a multi-layer DCP antenna is proposed in [?] whose main characteristic is its conical-shaped beam though the design suffers from narrow impedance bandwidth (of 3%) and high profile. Luo et al [?] also present a stacked multi-layer DCP antenna with fairly good CP bandwidth of 7.5% but poor inter-port isolation (of 7 to 21 dB). Chakrabarti [?] presents a shared-aperture DCP antenna with fairly high impedance bandwidth, AR bandwidth, and inter-port isolation though a thick foam-layer (0.1λ thickness) between the substrate and the ground-plane increases the antenna profile. Among the multi-layer DCP arrays, the antenna by Luo et al [?] is composed of sequentially rotated triangular patch elements which in spite of having a peak gain of 9.3 dBic, suffers from a relatively low gain in most of its usable bandwidth. In yet another sequentially rotated DCP antenna array [?] of corner-truncated patches, though high AR bandwidth and gain are achieved, the condition of strict-duplexity is unfulfilled because of different resonant frequencies for LHCP and RHCP mode. Furthermore, the antenna suffers from unwanted grating-lobes in spite of having high XPD (> 15 dB). A DCP antenna with versatile performance is presented in [?] whose principal shortcoming is its multilayer structure with a lossy power-divider in the feed network.

Ferreira et al [?] present a DCP antenna consisting of a ring-slot radiator with a metamaterial-based artificial magnetic conductor surface housed in an open cavity which suffers from the drawbacks of low AR bandwidth (4.8%) and interport-isolation (5 to 20 dB).

Isoflux beam is required in some types of satellite communications to ensure distribution of uniform signal strength over a well-defined region on the earth's surface. One such DCP antenna proposed in [?] consists of a dual circularly polarized feed and a choke horn antenna that requires a complicated fabrication.

A single-aperture DCP antenna having a dual-feed system for each polarization sense is presented in [?] which has a high profile and narrow AR bandwidth (3.2%) for one of the polarization types. In another shared-aperture DCP antenna [?], a single spidron fractal slot with an L-shaped slit is excited by utilizing the even and odd modes of a CPW transmission line. Kumar et al [?] also present a shared-aperture DCP slot antenna with two orthogonal ports having CPW transmission lines that in spite of being quite compact and wide-band, suffer from low-gain due to the bi-directional nature of its radiation pattern.

DCP antennas have also been used for energy-harvesting operations as demonstrated in [?] in which a shared square radiator has a feed-structure comprising a modified cross-slot with an annular ring-slot and four linear slot arms. This configuration gives a wide AR beamwidth (of 120°) though the impedance bandwidth and gain are not so high. Another DCP rectenna is presented in [?] in which a square microstrip patch is excited using a large AR bandwidth (30%) and good XPD (32 dB).

Filtering antennas with extremely low gain at the out-of-band frequencies are useful in wireless systems as they eliminate the losses between antennas and filters and reduce signal transmission path. One such dual-band DCP filtering antenna is presented by the authors in [?] that performs poorly in terms of AR bandwidths (1.1% and 3.2%) in spite of having good frequency selectivity and out-of-band rejection.

A non-planar, DCP omni-directional antenna, consisting of a printed dipole, is proposed in [?] that offers a relatively low gain of 0 to 2.4 dB in its entire AR bandwidth. One of the major challenges in designing of DCP antennas is to simultaneously realize wide beam and AR bandwidth which has been overcome in the work by Zhang et al [?] in which a cavity-backed metal patch is excited using ring-shaped microstrip feed-line. As far as CP performance is concerned, 3-dB beamwidth of 110° and AR bandwidth of 16% is reportedly obtained from the measured data. DCP antennas can also be designed for MIMO communication as shown in [?] where a CPW-fed slot antenna with orthogonal ports is presented.

Schematics of a few of the recent DCP planar antennas are shown in Fig. 3.1. A square-shaped slotted ground, having a modified meander line and excited by two CPW orthogonal lines is presented by authors in [25] in Fig. 3.1(a). A CPW-fed ultra-wide-band slot antenna with a U-shaped slot is presented in [64] as shown in Fig. 3.1(b). Another CPW-fed square slot antenna having an inverted-L grounding strip and orthogonal feed-lines having T-shaped stubs at their ends [65] can be seen in Fig. 3.1(c). A dual-band dual-sense CP antenna is presented in [66] and can be seen in Fig. 3.1(d). Xu et al [67] propose a microstrip-fed DCP slot antenna with a U-shaped slot that can be seen in Fig. 3.1(e). Chandu and Karthikeyan [68] present a ultra-wideband DCP monopole antenna having a modified ground plane as seen in Fig. 3.1(f). Chaudhuri et al [69] have demonstrated that using a complementary split-ring based isolator, a high port-to-port isolation of upto 18 dB can be achieved in a broadband DCP slot antenna. In this design the isolator blocks the surface currents thus aiding in port decoupling which can be seen in Figs. 3.1(g) and 3.1(h). Wu et al [70] present a DCP microstrip antenna with a circular patch having asymmetric slots based on an orthogonal-feed system. The antenna has a relatively simple geometry but has a narrow AR bandwidth of only 4.8% though this is sufficient to cover the RFID frequency band as shown in Fig. 3.1(i).

3.2 Sequentially rotated CP antenna arrays

The technique of sequential rotation is a method commonly used CP arrays for producing main-beams with high polarisation purity [?] and have better radiation pattern symmetry [?]. In this feeding technique, it is ensured that the phase angle ϕ of the n^{th} element is $\frac{2\pi(n-1)}{N}$ where N is the total array size [?]. Kumar et al [?] present a 4×4 array consisting of 2×2 subarrays of corner truncated square patches. In this scheme, the sequential rotation is applied only on the subarrays and the antenna, having a gain of 22 dBic, is suitable for X-band spacecrafts. A dual CP sequentially rotated array consisting of interlaced microstrip patch arrays of size 2×2 is discussed in [?]. A combination of series feeding and sequential rotation is applied in a CP array in [?] to achieve a peak gain of 18 dBic. In a CP antenna array employing both the corporate and the sequential feeding technique, a large AR bandwidth of 3 GHz with a low AR (≤ 1) and a high gain of 18 dBic is obtained by the authors in [?].

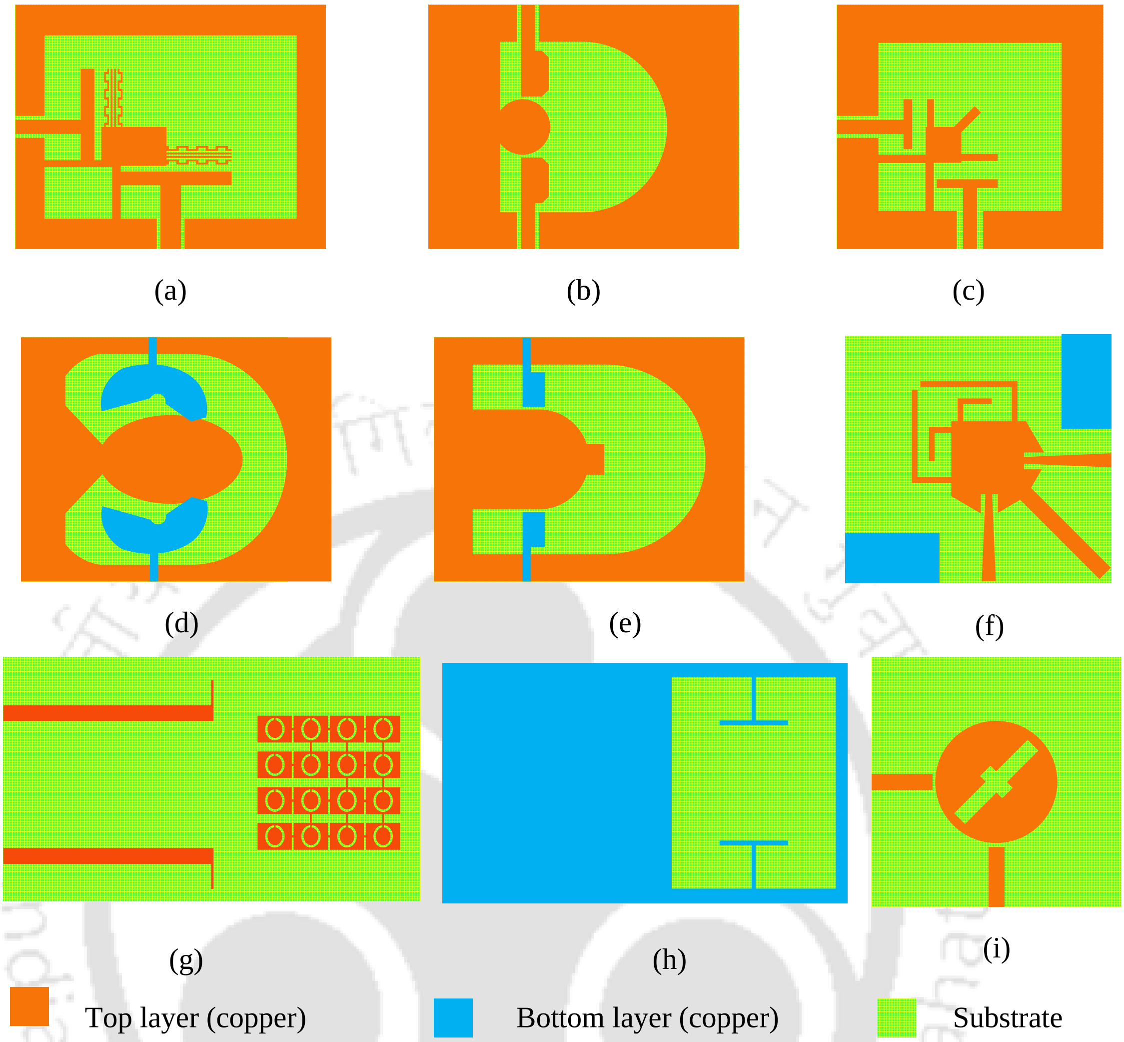

Fig. 3.1: Examples of DCP antenna arrays in contemporary literature (a) CPW-fed DCP wideband slot antenna with modified meander line [25] (b) CPW-fed DCP ultra-wideband slot antenna [64] (c) DCP ultra-wideband slot antenna with inverted L-shaped grounded strips [65] (d) Dual wideband horse-shoe shaped slot antenna [66] (e) DCP ultra wideband U-shaped slot antenna [67] (f) DCP microstrip-fed monopole antenna [68] (g) & (h) DCP slot antenna with a novel isolator [69] and (i) DCP antenna with crossed-slots on circular patch [70]. Note - The antennas in (a), (b) and (c), having slotted ground-planes, are devoid of any metal on their obverse sides. In case of the antenna in (i), being a circular patch antenna, the metallization of the ground is intact beneath the substrate. For the rest, the metallizations on reverse sides are shown in sky-blue.

3.3 Series-fed CP antenna

In the preceding section, we have discussed resonant antennas where the radiated waves travel back and forth. This section introduces a different kind of antennas called travelling wave antennas (also known as leaky-wave antennas) which are a type of series-fed antenna arrays. Series-fed resonant antennas are terminated by an open or a short-circuit, with the inter-element spacing being equal to one wavelength. This ensures bore-sight beam though at the cost of a narrow bandwidth. In contrast, travelling-wave arrays are terminated by matched load to absorb any residual power. The important advantages of these types of antennas are their wide bandwidths [?] and the scanning feature of main beams with frequencies [?]. This type of antennas are especially useful in satellite communications as the satellite observed from the earth's surface always has the main-beam tilted at an angle ranging from 24.4° to 67.3° away from the broadside direction [?]. Other important advantages are - good Axial Ratio [?] and the fact that individual elements need not be separately excited [?].

Two of the first DCP antennas of this type were devised by Lum et al in [?, ?]. In these works, two successive radiating patches are placed on the edge of a circular slotline at a distance apart such that CP is generated. In another work by Lum et al [?], the four-port CP antenna contains a folded slot-line so that the overall size of the antenna is reduced. In this antenna, the successive patches are placed at incremental offsets with respect to the slot so that all the patches receive the same amount of coupled power as the signal propagates around the slot that gradually decreases in amplitude. Min and Free [?] present an analysis of this type of arrays using a power control model considering the losses due to feed line. In this work, the authors have considered two different aperture-coupled arrays of 4 and 8 elements, and as expected, the gain of the larger array is considerably higher (by 5 to 6 dBic). The same authors have reported another CP antenna [71] with two concentric ring sub-arrays of linearly polarized rectangular patch elements with 4 and 8 elements in the inner and outer ring. The patches are excited through rectangular apertures on the ground plane. Hallbjorner et al [72] present a DCP antenna for operation at 5.6 GHz consisting of an array of series-fed 5 pentagonal patches. A series-fed DCP antenna array of circular patches excited by proximity coupling is reported in [73]. Some of the common configurations of CP series-fed antenna arrays are given in Fig. 3.2.

Chaudhuri et al [74] present a DCP microstrip antenna comprising 12 series-fed radiating patch elements separated by phase shifters. These elements are arranged in a circular fashion with two ports at the feed-lines connected to terminal patches- one each for transmission (T_X) and reception (R_X). The impedance and AR bandwidth are 399 MHz and 256 MHz respectively with the overlap of the two being > 64%. The interport isolation is very high and ranges from

30 dB to 59 dB though the gain is modest (2.9 to 3.87 dBic). The low gain can be due to lossy substrate (FR-4) and sparse array-like structure.

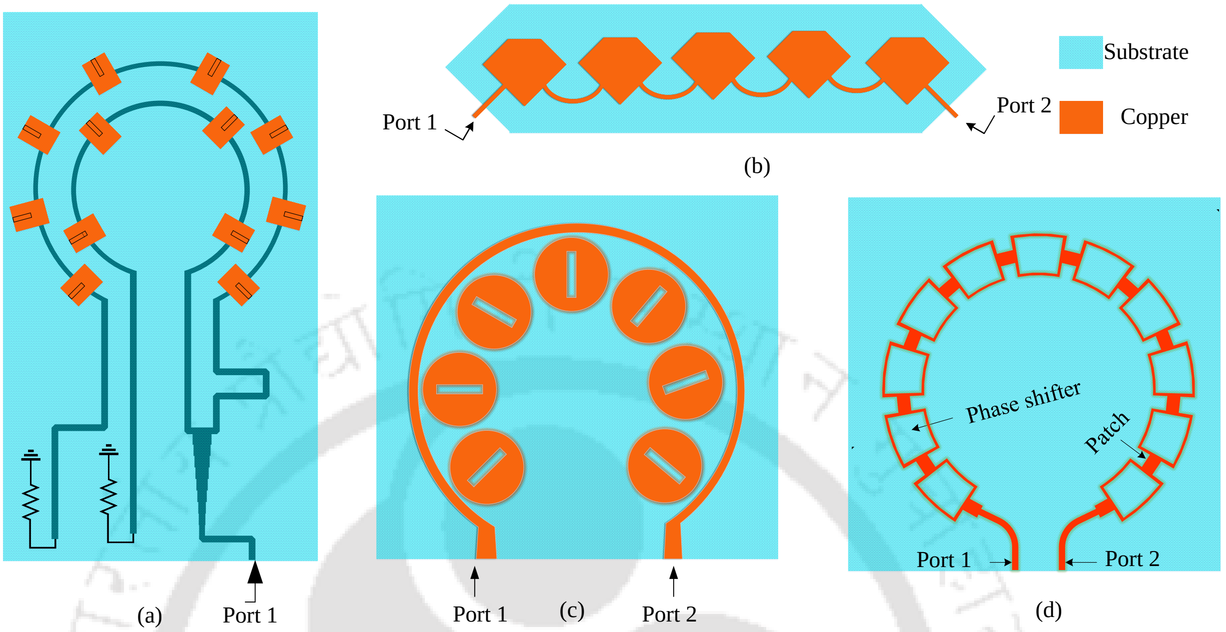

Fig. 3.2: Some series-fed CP antenna arrays in contemporary literature (a) Series-fed concentric ring patch array [71] (b) DCP array with chamfered patches [72] (c) DCP array with proximity coupling [73] and (d) DCP modified Franklin antenna array [74]

It is thus obvious from the above discussion that for a simple receiver design, both the port-to-port isolation and BW_{AR} should be very high. While the EMC reduction is accomplished by various decoupling networks, for a wider bandwidth slot antennas are a preferable. However, since slot antennas suffer from low broad-side gain, additional techniques for back-lobe suppression need to be considered.

3.4 Summary

In the first part of this chapter, a large number of planar single-element DCP antennas are presented employing various technologies like - multi-layer, cavity-backing, aperture-coupling, co-planar waveguide (CPW), etc. From this discussion, one arrives at the conclusion that, if high AR bandwidth is desired, DCP antennas with slotted-ground planes are desirable. In the later part of this chapter, series-fed arrays have been discussed which perform well in all the parameters in spite of having simple feed-networks.

4

Dual circularly polarized antenna with interdigital capacitor

*A planar dual circularly polarized slot antenna is presented. The designed antenna has two tilted '8' shaped slots fed by microstrip lines, one each for transmission (T_X) and reception (R_X) operations. The isolation between the two ports (*i.e. *T_X and R_X) is augmented by means of an interdigital capacitor based bandstop filter. The proposed antenna has an impedance bandwidth of 361 MHz centered at 2.293 GHz (2.113 - 2.474 GHz) with the isolation between the ports being >17.6 dB which goes up to a value as high as 46 dB within the band of operation. The 3 dB AR bandwidth is 11.52% centered at 2.1275 GHz though the actual usable AR bandwidth is 137 MHz. Because of its high inter-port isolation within the AR bandwidth, the design is suitable as a full-duplex antenna for applications in S-band.*

4.1 Introduction

In this work, a DCP FDX slot antenna with high inter-port isolation and wide impedance and AR bandwidth has been presented. This design incorporates the approach presented in [?] where it was shown that the inter-port isolation may be enhanced by introducing a net negative admittance of $-jB$ to cancel out the residual signal between the T_X and R_X ports. The proposed antenna has two '8' shaped slots inclined at 135° and 45° to the horizontal axis for R_X and T_X operations respectively. The diagonally opposite corners of the tilted square slots have square appendages [?] thereby generating two mutually orthogonal polarizations in two slots. In the present design, an interdigital capacitor (IDC) is provided between the port feeding lines, which aids in decoupling the ports. This IDC acts as band-stop filter (BSF) which reduces the residual admittance between the ports and hence mitigates the mutual coupling between the T_X and R_X slots. This filter has the advantage of compactness in size compared to the conventional open circuited quarter-wavelength capacitor.

The proposed antenna has fairly high gain within the AR and impedance bandwidth and relatively low inter-port coupling better than 17.6 dB which is suitable for most industrial applications. The antenna is ideal for applications like mobile satellite service (MSS) (2000 MHz to 2200 MHz) and UMTS or IMT-2000 (2110 - 2200 MHz).

4.2 Antenna geometry

Fig. 4.1(a) shows the front view of the antenna comprising two tilted slots on the ground. The slots are designed using the equation given in [?]

$$W = \frac{c}{2f\sqrt{\varepsilon_{re}}} \tag{4.1}$$

where W is the dimension of the slot, c is the velocity of light, f is the frequency of interest, and ε_{re} is the effective relative permittivity. From this equation, the initial dimension of the slot is roughly obtained to be 46.1 mm which is then optimized in the software for the best performance at the desired frequency. It is to be noted that the perimeter of the slot is $2S_1 + 2S_2 + 2S_3 + 2\sqrt{S_2^2 + S_3^2} = 155$ mm which is approximately one wavelength. The feed line beneath the substrate excites a travelling-wave magnetic current in this slot which is instrumental in

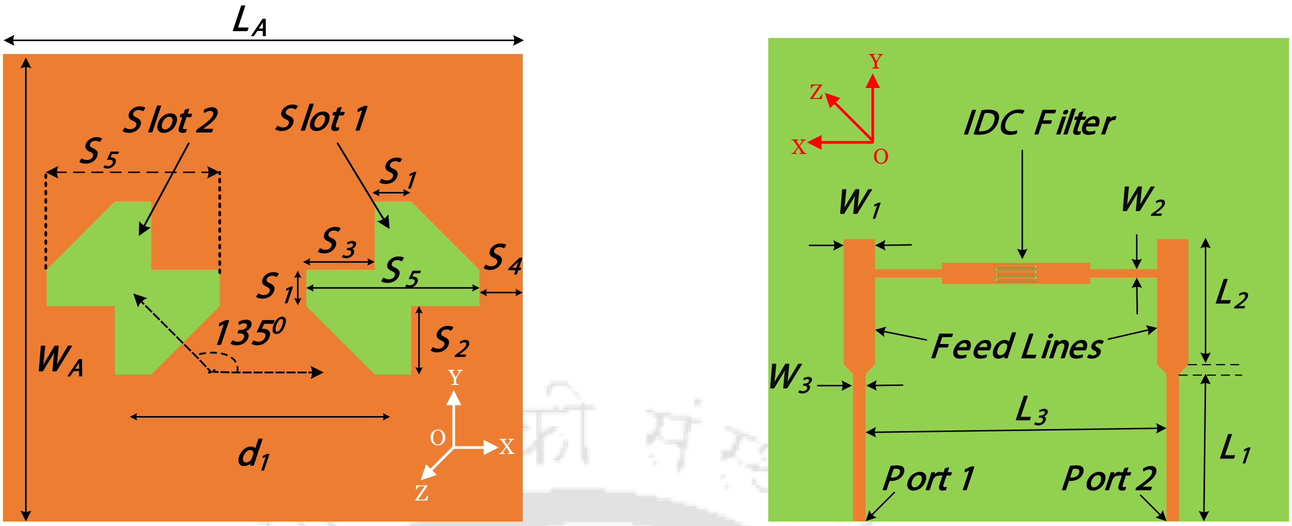

(a) (b)

Fig. 4.1: Front and rear view of the antenna showing (a) slotted ground plane and (b)feed-network with IDC

generating a EM waves in the far-field zone with 90° spatial and temporal phase, and thus CP radiation is produced [?, ?, ?].

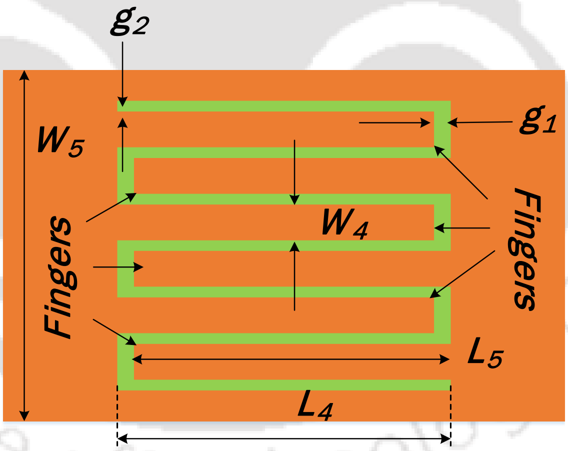

Fig. 4.2: Enlarged view of the IDC filter showing the 6 fingers

The reverse side of the antenna is shown in Fig. 4.1(b) whereas Fig. 4.2 depicts the enlarged view of the band-stop filter comprising IDC. The two microstrip lines shown in Fig. 4.1(b) form the feed of the slots. The net dimension of the antenna is 150 mm × 135 mm × 1.6 mm fabricated on FR-4 substrate ($\varepsilon_r = 4.3$, $\tan\delta = 0.03$). The filter lying between the feed lines has six fingers or digits. The width of the lower part of a feed-line W_3 was optimized in such a way that it has an impedance of $50\,\Omega$ for compatibility with standard devices. Since the antenna is symmetric about the ports, for the sake of brevity, the radiation patterns, AR and gain with respect to frequency presented here have been obtained by exciting port 1 of the antenna that corresponds to slot 1 (on the right side of Fig. 4.1(a)). The planes of radiations of the orthogonal CP waves are different for each type. Hence at the plane $z > 0$, slot 1 radiates in LHCP sense whereas at the $z < 0$ plane the same slot radiates in RHCP sense. This concept is similar to the ones discussed by the authors [65, 68] in their designs of DCP antennas. The values of geometric parameters of Figs. 4.1 and 4.2 are given in Table 4.1.

GP	Value	GP	Value	GP	Value	GP	Value	GP	Value
S_1	10.50	S_2	19.75	S_3	19.75	S_4	12.50	S_5	50.00
L_A	150.00	W_A	135.00	d_1	75.00	L_1	37.50	L_2	30.00
L_3	60.00	W_1	7.50	W_2	2.37	W_3	3.00	g_1	0.50
g_2	0.10	L_4	10.00	L_5	9.50	W_4	0.40	W_5	4.25

Table 4.1: Values of the geometric parameters (GPs) of Figs. 4.1 and 4.2 (all values are in mm)

4.3 Design prototypes

Before arriving at the final design, three different prototypes were developed and their performances were examined as shown in Figs. 4.3(a), 4.3(b) and 4.3(c). Prototype 1 in Fig. 4.3(a) shows the antenna with two square slots. Prototype 2 of Fig. 4.3(b) is a further modification of Prototype 1 which has triangular appendages at the corners of the square slots whereas in Prototype 3 of Fig. 4.3(c) the radiating elements are made up of two pairs of conjoined square slots. Finally, Prototype 4 shown in Fig. 4.3(d) combines the features of all the preceding ones. Fig. 4.4(a) and 4.4(b) show the performances of the prototypes in terms of $|S_{11}|$ and AR versus frequency. It is evident from the plots that Prototype 4 has the best of these features in terms of both impedance matching and circular polarization. Hence, Fig. 4.3(d) is the prototype that was chosen for final design and measurements.

4.4 Parametric analysis

The parametric analysis is divided into two parts, namely study of parameters of the IDC filter and those of the antenna as discussed in the following sub-sections.

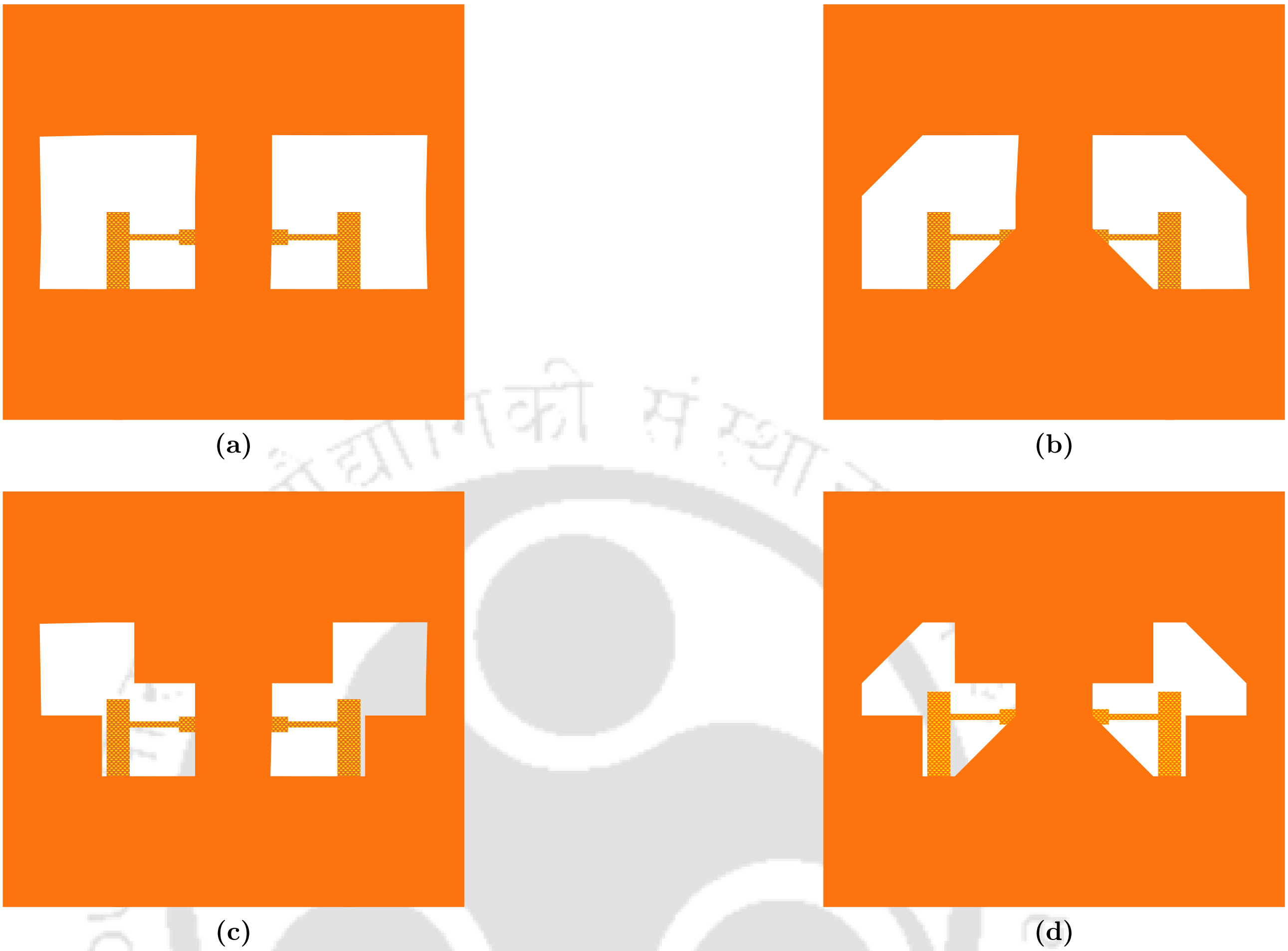

(a) **(b)** **(c)** **(d)**

Fig. 4.3: Different prototypes of the antenna (a) Prototype 1, (b) Prototype 2, (c) Prototype 3, and (d) Prototype 4 (The feed network is shown against the white background within the slots beneath the substrate)

4.4.1 IDC Filter parameters

The filter was designed in such a way that its band-stop characteristics lie at around the resonant frequency of the antenna. To this end, the net finger length ($L_5 = L_4 - g_1$) and the number of fingers (n) were optimized. This is in accordance with ref [**?**] which established that

$$C\,(\text{in pF}) = l[k_1(n-3) + k_2] \tag{4.2}$$

where C is the capacitance, l (L_5 as per Fig. 4.2) is the net length of the capacitor finger, and k_1 and k_2 are constants. This value of C determines the central frequency of the filter. The different $|S_{21}|$ characteristics of the filter with varying finger number n is shown in Fig. 4.5(a). As evident from the figure, for $n = 6$, the central frequency is 1.98 GHz with a 3 dB

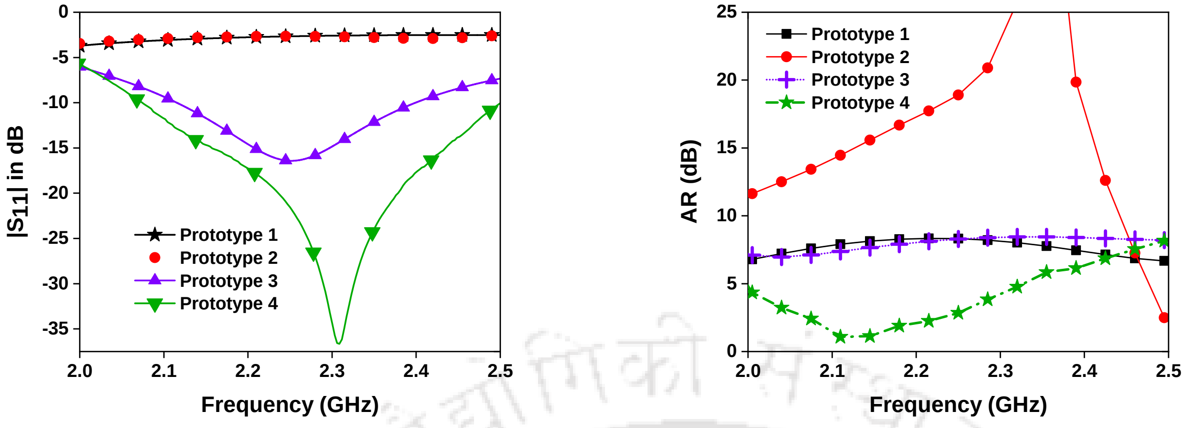

(a) (b)

Fig. 4.4: Performance of different prototypes (a) $|S_{11}|$ and (b) AR with respect to frequency

bandwidth of 405 MHz which ensures that the isolation produced by the device across its ports is maximum around this frequency. The variation of center-frequency of the filter with respect to finger length L_5 is shown in Fig. 4.5(b). Since maximum isolation is desired within the antenna operating frequency, L_5 is chosen as 9.5 mm.

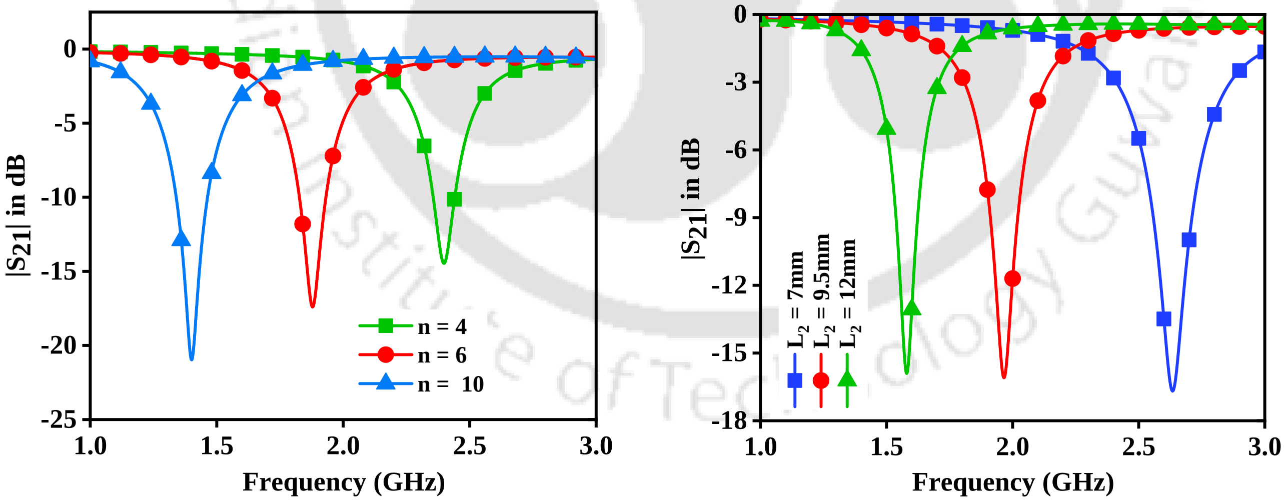

(a) (b)

Fig. 4.5: Characteristic of IDC filter (a) with varying finger number n and (b) for different finger lengths L_5 with respect to frequency

4.4.2 Antenna parameters

It has been seen that the antenna parameters are mainly dependent upon length (L_A), width (W_A), edge-length of the slot (S_1) and feed-line width (W_1). It is obvious from Fig. 4.6 that the best isolation is obtained when $L_A = 150$ mm which is one of the major design goals and any other value of L_A yields poorer inter-port isolation.

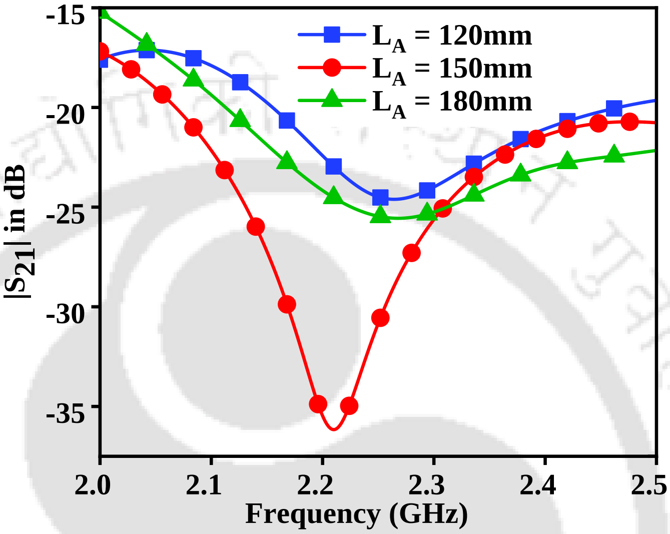

Fig. 4.6: Variation of $|S_{21}|$ with antenna length L_A

From Figs. 4.7(a) and 4.7(b) it is observed that the CP performance of the antenna is severely degraded for $W_A = 160$ mm though the inter-port isolation is still acceptable. For $W_A = 110$ mm even though the ports are adequately decoupled, the AR bandwidth is narrower than when $W_A = 135$ mm. For this reason, W_A is chosen as 135 mm.

Fig. 4.8 depicts that the variation of $|S_{11}|$ for different values of S_1. It can be observed that this is an important parameter for a good impedance matching and best results are obtained for $S_1 = 10.5$ mm because for other values of S_1 the return loss suffers unwanted degradation.

Selecting the proper feed-line width W_1 is essential for impedance matching as seen from Fig. 4.9(a). The optimum value is found to be $W_1 = 7.5$ mm. It is to be noted that the value of W_1 has a role in the positioning of minimum isolation point as seen in Fig. 4.9(b) as this factor decides the impedance seen by the IDC. A lower or higher value of W_1 shifts the $|S_{21}|$ minima to either higher or a lower frequency and also affects the gain as seen in Fig. 4.9(c). It can therefore be concluded that the feed-width W_1 controls the reactance encountered by the IDC filter and hence it is essential to choose W_1 properly for best inter-port isolation within

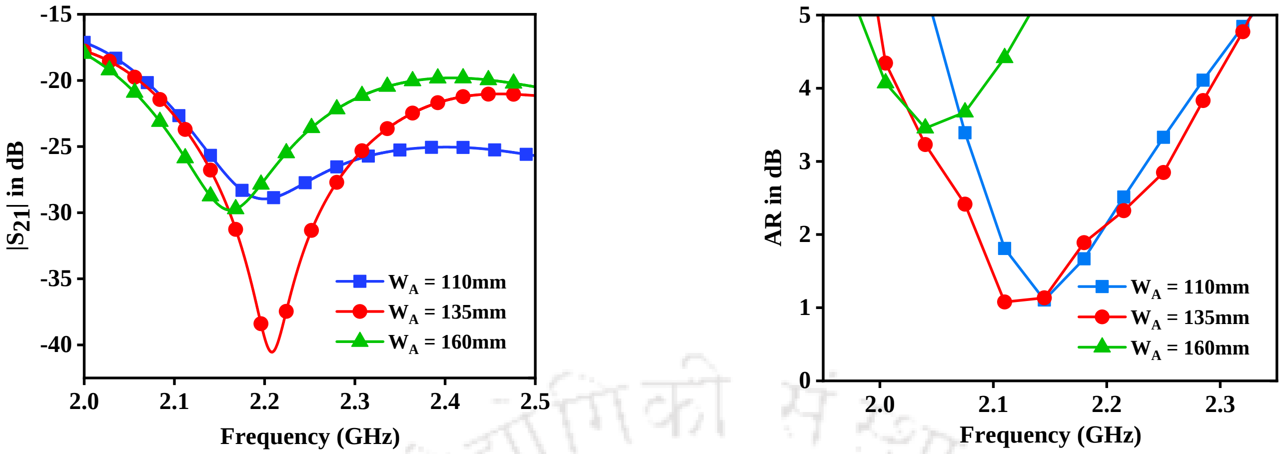

(a) (b)

Fig. 4.7: Variation of antenna performance for different values of W_A (a) $|S_{21}|$ and (b) AR with respect to frequency

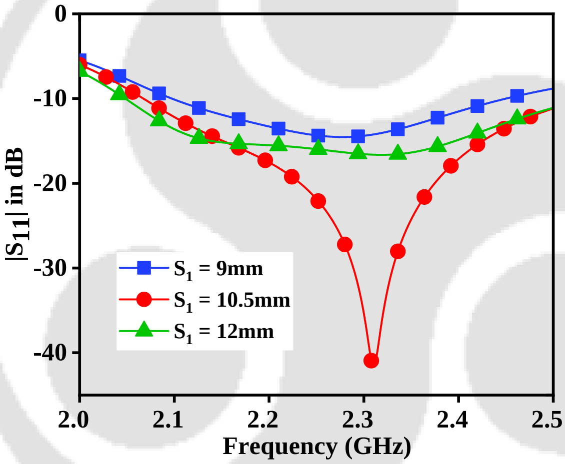

Fig. 4.8: Variation of $|S_{11}|$ with S_1 at different frequencies

the AR and impedance bandwidth.

4.5 Results and discussions

Fig. 4.10(a) shows the plots of $|S_{11}|$ and $|S_{21}|$ versus frequency. It can be seen that the -10 dB bandwidth is 361 MHz i.e. 15.75% of the central frequency $f_0 = 2.293$ GHz. The isolation in this band is > 17.6 dB that reaches 46 dB at 2.225 GHz. From the same figure it can also be observed that the isolation between the ports without the IDC filter ranges from 17 dB to 20 dB. The slight deviations of the measured values from the simulated parameters can

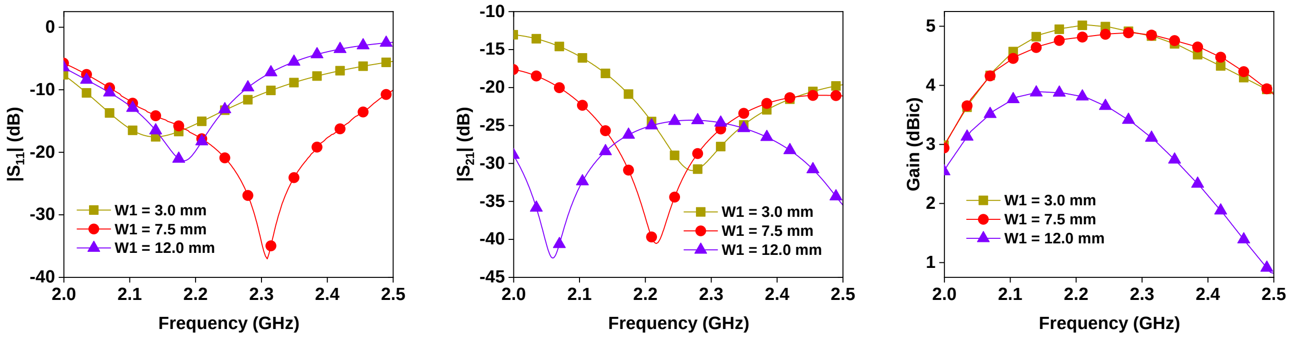

(a) (b) (c)

Fig. 4.9: Variation of antenna performance for different values of W_1 (a) $|S_{11}|$, (b) $|S_{21}|$ and (c) gain with respect to frequency

be attributed to fabrication tolerances, soldering, and connector imperfections. Fig. 4.10(b) shows the current distribution in the feed lines corresponding to ports 1 and 2. The higher current distribution in the feed-line of port 1 compared to that of port 2 indicates the bandstop filtering action of the IDC.

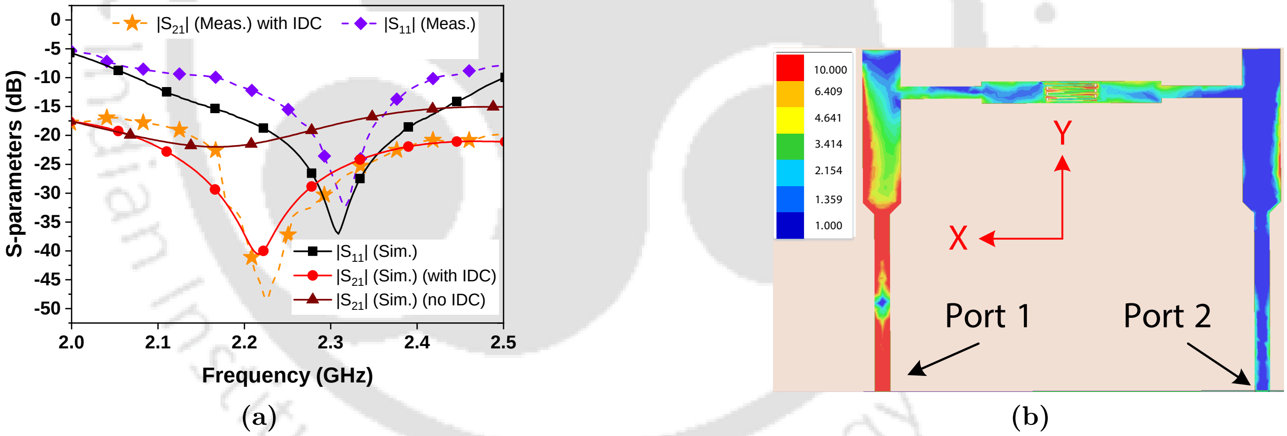

(a) (b)

Fig. 4.10: Performance of the antenna (a) Simulated and measured S-parameters with respect to frequency and (b) Current distribution in the feed lines corresponding to Ports 1 and 2 at $f = 2.13$ GHz (Sim. - Simulated, Meas. - Measured)

The IDC BSF has an area of 4.25 mm × 9.5 mm that is only 12.45% of the physical size of a traditional quarter-wave microstrip BSF (of dimension 18 mm × 18 mm). The method of composite vector analysis [?,68] has been employed to study the nature of rotating surface currents and identify the polarization sense. The different current densities around the radiating slot at different phase angles (at $\omega t = 0°$, $90°$, $180°$ and $270°$), are shown in Fig. 4.11 by means of solid black lines whereas the resultant **R** of the current components is represented by dotted red lines. The lengths of the black arrows roughly correspond to the strength of the magnetic currents as observed from the colours of the current vectors on the ground plane. Since the tip of the vector **R** rotates in clockwise direction if seen from $z > 0$ plane, it can be concluded that LHCP is generated in that plane.

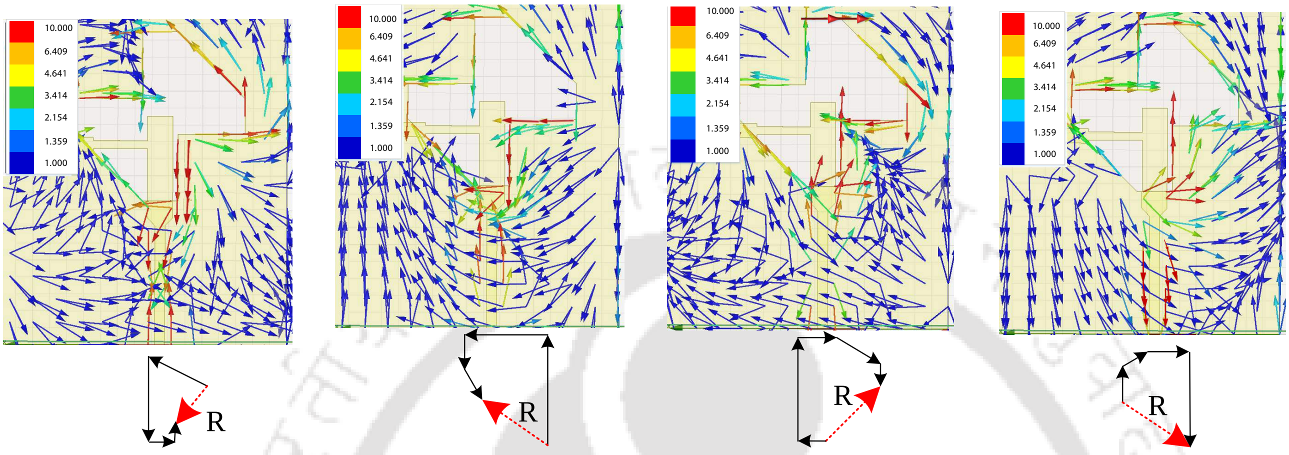

(a) **(b)** **(c)** **(d)**

Fig. 4.11: Current density around the excited slot at $f = 2.125$ GHz for the phase angles (a) $\omega t = 0°$ (b) $\omega t = 90°$ (c) $\omega t = 180°$ and (d) $\omega t = 270°$

In the power pattern and AR measurements of this antenna, port 2 was terminated by a matched load of $50\,\Omega$ to study the characteristics of the slot corresponding to port 1 which is same as the procedure followed while studying dual polarized antennas as mentioned in [68]. Since the antenna is symmetric, exactly similar results will be obtained when port 2 is excited. The polar radiation pattern plots of port 1 are shown in Fig. 4.12 for the xoz-plane and the yoz-plane. It can be seen from Figs. 4.12(a) and 4.12(b) that port 1 transmits LHCP in the upper hemisphere which is also confirmed by the direction of rotation of current vectors. Since the radiating slot is located at an offset with respect to the centre of the antenna, the beam is slightly tilted off the broadside direction. The best cross-polarization level is 18 dB.

From Figs. 4.12 and 4.13a it may be observed that the radiation pattern is fairly bi-directional and the gain is moderate. These features agree with the characteristics of slot antennas that generally have high bandwidth at the cost of low front-to-back ratio (FBR). This bi-directional nature of the beam is especially useful in S-band satellite communications [?, ?], mobile communication [?] and communication in coal-mines [?]. The simulated radiation efficiency of the proposed antenna is > 78% and reaches as high as 84% within the impedance bandwidth. Fig. 4.14 shows the photograph of the fabricated and tested antenna.

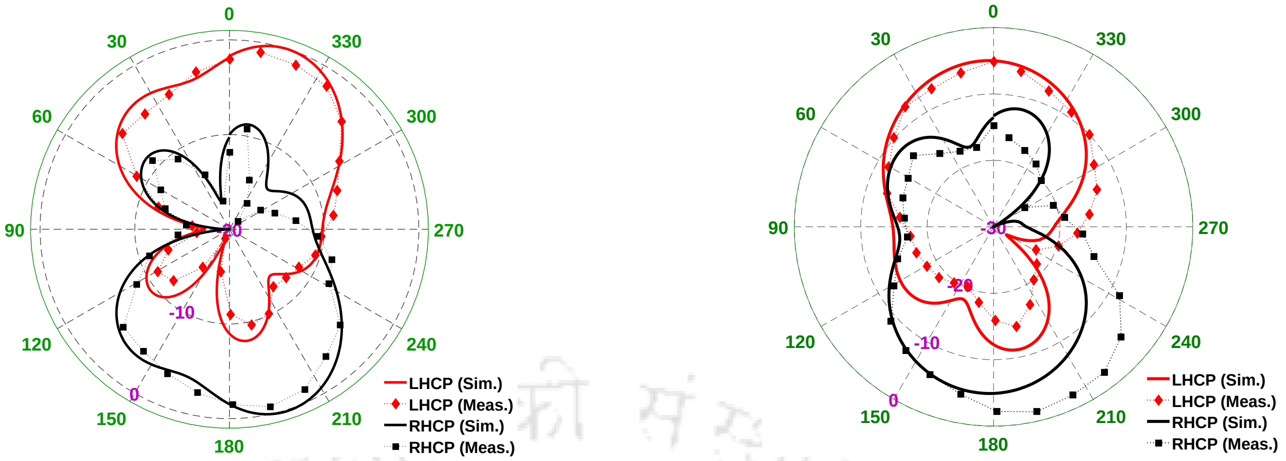

(a) **(b)**

Fig. 4.12: Normalized radiation pattern at $f = 2.13$ GHz in (a) xoz-plane and(b) yoz-plane

The AR plot shown in Fig. 4.13(a) from which it can be seen that the 3 dB AR bandwidth is 11.52% of the centre-frequency $f_{AR} = 2.1275$ GHz. It is to be noted that the antenna is usable as a DCP antenna within the frequency band 2.113 GHz to 2.25 GHz i.e. 137 MHz as $|S_{11}| < -10$ dB and $AR < 3$ dB within this region (denoted by yellow-coloured box in the plot). Beyond this frequency band, the antenna acts as a DLP antenna for the remaining part of the impedance bandwidth. The same plot also shows the maximum gain at different frequencies which ranges from 3 to 5 dBic.

4.5.1 MIMO Performance:

Since the ports of this antenna are mutually orthogonal, it is worthwhile calculating the ECC as this quantity (denoted by ρ_e) is an important parameter to check the suitability of the antenna for MIMO performance [?]. The ECC (ρ_e) is calculated from the S-parameters as given in [?]. Another important parameter for MIMO antennas, called the diversity gain is given by [?]:

$$DG = 10\sqrt{1 - \rho_e^2} \tag{4.3}$$

The plots of ECC and DG of this antenna are shown in Figs. 4.13(b) and 4.13(c) which indicates that the ECC is lower than 0.02 and the DG is very stable at 10 dB in its entire operational bandwidth. Thus the antenna may be used for MIMO applications.

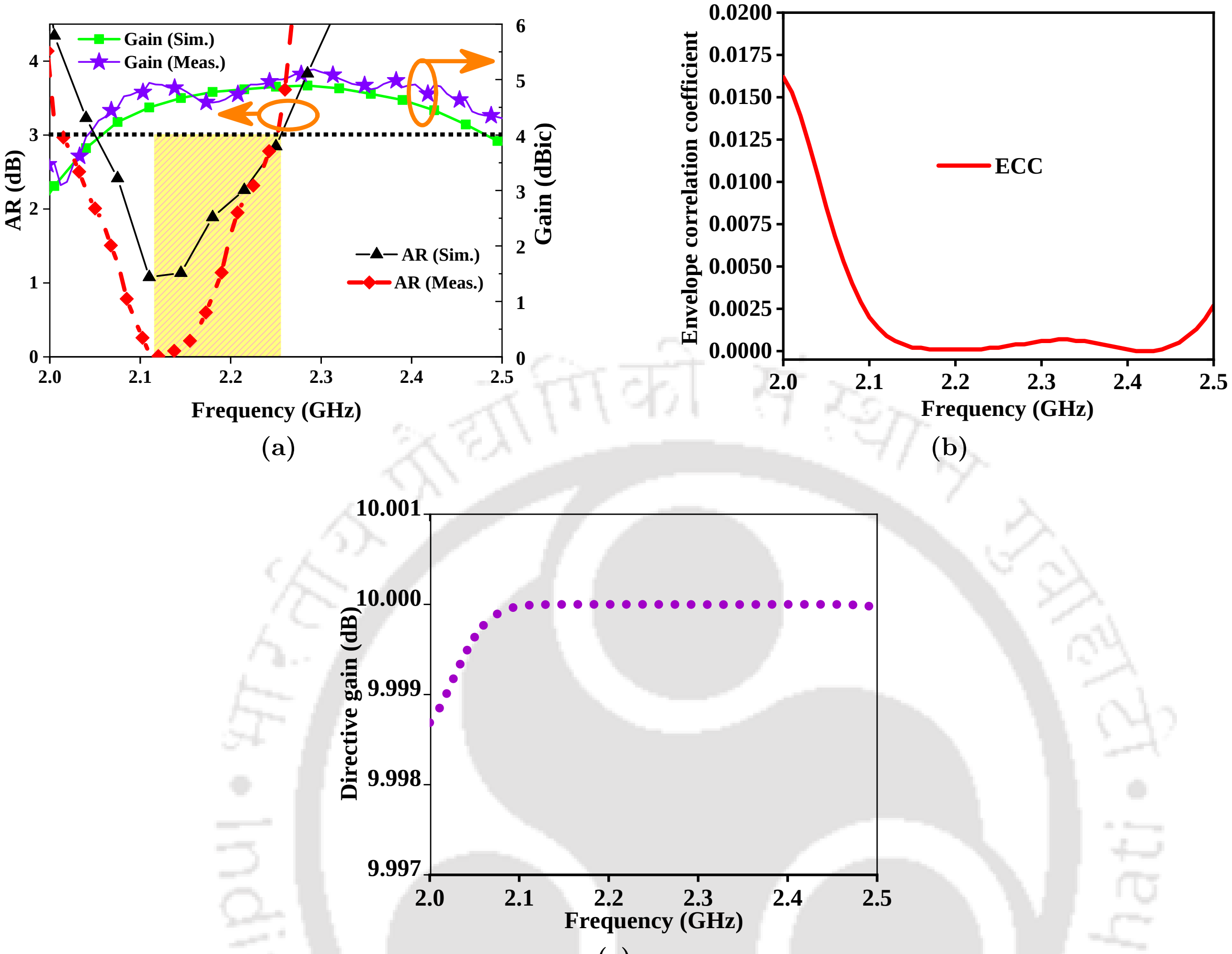

(a)

(b)

(c)

Fig. 4.13: (a) AR and gain (both simulated and measured), (b) ECC and (c) DG as functions of frequency

Table 4.2 presents a comparison of the performances of the proposed antenna with other recent DCP antennas. It is to be noted that, for a fairer comparison, the gain mentioned for ref [?] is the one without the metallic reflector. Among all the antennas given here, the proposed one performs the best in terms of inter-port isolation while having a very simple structure and a moderate gain because of its low FBR. This is especially in contrast to [?] and [?] which, in spite of demonstrating superior gains, have complex multilayer structure. It can therefore be summarized from the table that this antenna has better performance in terms of inter-port isolation and AR bandwidth than most of the ones mentioned in the table with the gain being the best among the bi-directional antennas.

(a) (b)

Fig. 4.14: Photograph of the fabricated and tested antenna (a) slotted ground plane (b) feed-lines with IDC

4.6 Design guidelines

The following design guidelines may be followed:

Step 1: The length of the slot is determined from the equation $W = \frac{c}{2f\sqrt{\varepsilon_{re}}}$ where where W is the dimension of the slot, c is the velocity of light, f is the frequency of interest, and ε_{re} is the effective relative permittivity. From this equation, the initial dimension of the slot is roughly obtained to be 46.1 mm which slows a close match with the final optimised dimension $2 * S_2 + S_1$=50 mm. The total perimeter of the slot $2S_1 + 2S_2 + 2S_3 + 2\sqrt{S_2^2 + S_3^2}$ should be approximately one wavelength which is 155 mm in this case.

Step 2: The length of the ground-plane L_A, in conjunction with the frequency of operation f, is observed to control the $|S_{21}|$ that can be roughly estimated using the equation given below obtained from curve-fitting technique.

$$\begin{aligned} |S_{21}| = &-2724 + 3157 * f + 10.4 * L_A - 1176 * f^2 - 9.345 * f * L_A \\ &- 0.004269 * f^2 + 146 * f^3 + 1.79 * f^2 * L_A + 0.004258 * f * L_A^2 \end{aligned}$$

To test the validity of this equation, as an example only the plot for L_A=150 mm (which is equal to $2.34\lambda_g$) is shown in Fig. 4.15a which indicates that the equation above gives a good estimate of the $|S_{21}|$.

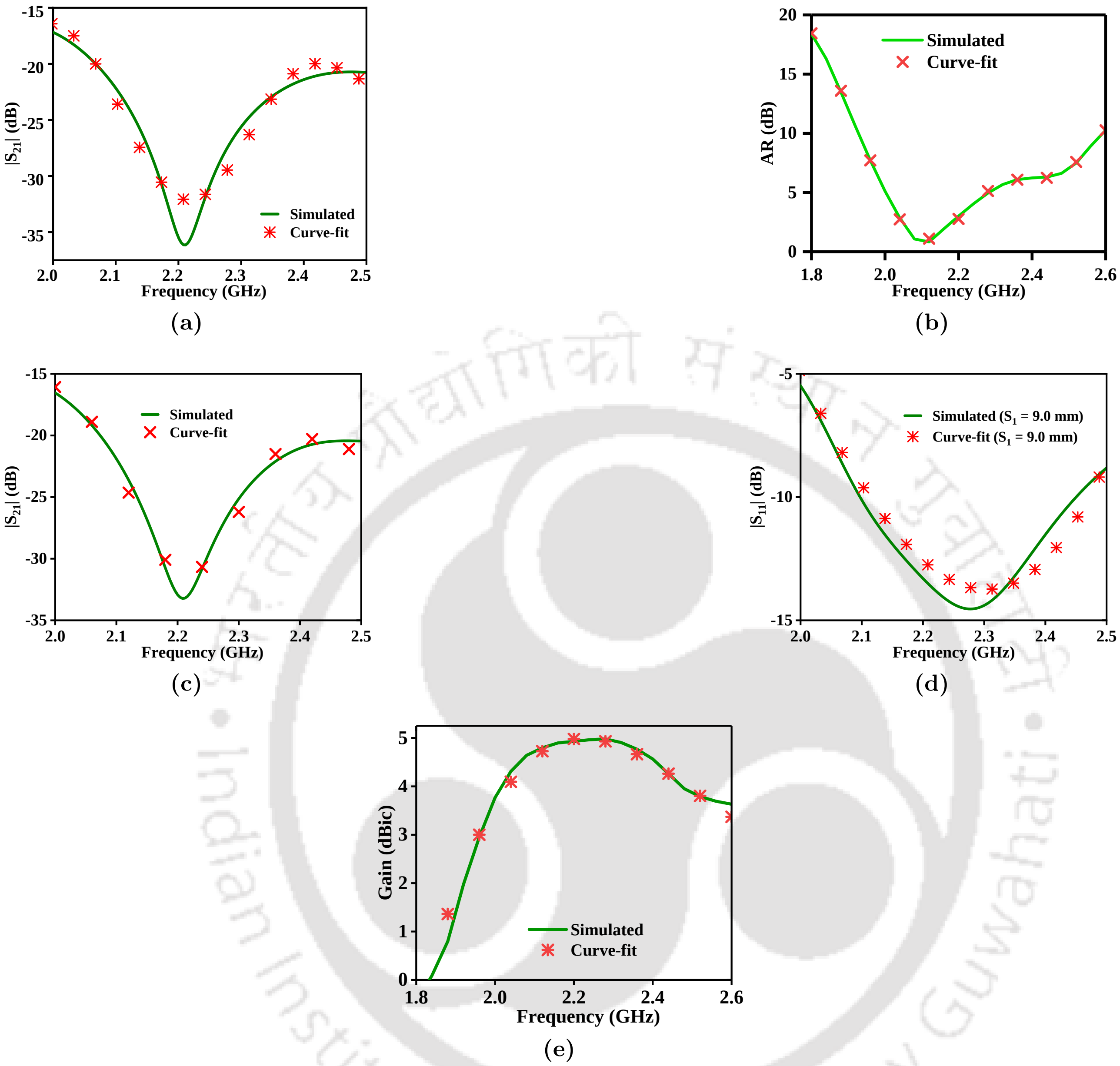

(a) (b) (c) (d) (e)

Fig. 4.15: Plots of curve-fit and simulated data (a) $|S_{21}|$ versus frequency for $L_A = 2.34\lambda_g$ (b) AR versus frequency for $W_A = 135$ mm or $2.1\lambda_g$ (c)$|S_{21}|$ versus frequency for $W_A = 135$ mm or $2.1\lambda_g$ (d) $|S_{11}|$ versus frequency for $W_A = 135$ mm or $S_1 = 0.14\lambda_g$ (e) Gain versus frequency for $W_1 = 0.11\lambda_g$

Step 3: The width of the ground-plane W_A controls both the AR and $|S_{21}|$ as discussed in the Parametric Study. The following two equations give a reasonably accurate estimate of these metrics for a given $W_A = 135$ mm (or $2.1\lambda_g$ in this case) at different frequency points f.

$$\begin{aligned} AR\,(\text{in dB}) = 35.16 * \sin(1.906 * f + 4.595) + 24.41 * \sin(3.773 * f + 9.688) \\ +1.733 * \sin(15.04 * f - 1.448) \end{aligned}$$

$$|S_{21}| = -21.58 - 4.16 * \cos(8.008 * f) + 3.97 * \sin(8.008 * f) + 2.83 * \cos(16.016 * f) + 1.80 * \sin(16.016 * f) + 1.06 * \cos(24.024 * f) - 0.05 * \sin(24.024 * f)$$

The plots in Figs. 4.15b and 4.15c below test the validity of the above equations for $W_A = 135$ mm.

Step 4: In the next step the slot dimension S_1(as in Fig. 4.1a) is optimised for the best impedance bandwidth. The following equation relates $|S_{11}|$ to both S_1 and frequency f.

$$|S_{11}| = -1007.5 + 1145 * f + 116.8 * S_1 - 447 * f^2 - 78.65 * f * S_1 - 4.274 * S_1^2 + 74.97 * f^3 + 5.297 * f^2 * S_1 + 2.585 * f * S_1^2$$

As an example, the plot of $|S_{11}|$ versus frequency for $S_1 = 0.14\lambda_g$ or 9.0 mm is shown in Fig. 4.15d.

Step 5: A rough estimate of the feed-line width W_1 is obtained by specifying the peak-gain at different frequencies (f) constrained by the equation given below.

$$\text{Gain (in dBic)} = 26.47 * f^3 + -198.1 * f^2 + 488.4 * f - 392.55$$

The plot of gain with respect to frequency for $W_1 = 7.0$ mm is shown in Fig. 4.15e as an example.

Step 6: The interdigital capacitor (IDC) filter has a capacitance that is found to obey 4.2 which is produced here: $C\,(\text{in pF}) = l * [k_1 * (n - 3) + k_2]$. This value of C determines the central frequency of the filter. Therefore, since the resonant frequency of the antenna and its AR bandwidth are known, the capacitor is designed in such a way that its stopband coincides with the antenna AR bandwidth.

4.7 Packaging of the antenna

While installing slot antennas, radomes are suggested for minimisation of interference from external factors [?,?]. The radome should be designed in such a way that its interference on the vital parameters of the antenna like reflection coefficient and radiation pattern. The prescribed thickness for a radome wall is given by Eqn. 5.27 of [?], though it should be noted that for radome materials having dielectric constants equal to 1 or slightly greater, any thickness is acceptable [?]. Slot antennas are susceptible to the presence of reflecting structures very close to the ground plane. This drawback is more pronounced in case of circularly polarised slot antennas as seen in [?]. With these considerations in mind, the antenna presented here is modified in the following manner:

- Providing metallic reflector below the feed-network to shield the slot lines from external interferences.
- Encase the antenna in hemispherical radome (polyurethane foam, $\varepsilon_r = 1.05$) of radius equal to 2.5 times that of the antenna dimension.

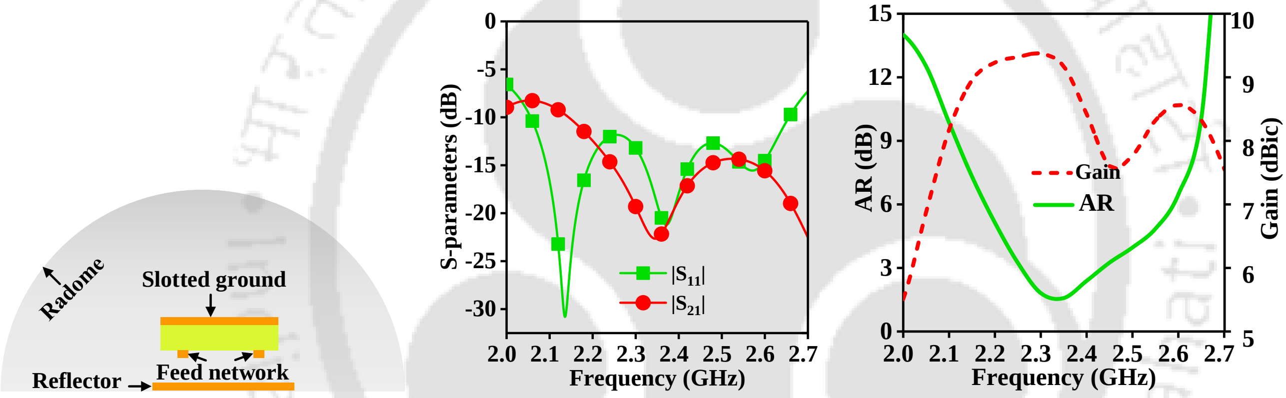

(a) (b) (c)

Fig. 4.16: Antenna with the radome and reflector (a) schematic (b) S-parameters (c) AR and gain

For the antenna presented here, the effect of such a metallic reflector is given graphically in Fig. 4.16a. The reflector is placed 21 mm below the substrate along the negative z- axis. The $|S_{21}|$ of the antenna suffers a slight degradation whereas the -10 dB impedance bandwidth shows an improvement of around 150 MHz as seen in Fig. 4.16b. The AR bandwidth (shown in Fig. 4.16c), though mostly unchanged at 180 MHz, has no offset with respect to the impedance band. The gain increases considerably to reach 7.8 to 9.6 dB within the AR bandwidth because the backlobe is suppressed as can be seen in Fig. 4.16c.

4.8 Summary

The antenna presented here is a DCP slot antenna built to operate on the S-band, that has two separate slots (corresponding to each polarization) where port decoupling was accomplished using an interdigital capacitor. This antenna has a 361 MHz bandwidth with port-to-port isolation ranging from 17.6 dB to 46 dB while the available AR bandwidth ranges from 2.113 to 2.25 GHz. As it is a slot antenna, its moderate gain and bi-directional main lobe has its utility in numerous kinds of applications like S-band satellite communications, MIMO communication, mobile communication (UMTS or IMT-2000), mobile satellite service (2000-2200 MHz) and communication in coal mines. Moreover, the low gain can be easily augmented to a considerably high value by addition of a metallic reflector behind the feed-lines at a distance of 21 mm.

Table 4.2: Comparison of the performance of the proposed antenna with other recently reported antennas: IBW - -10 dB impedance bandwidth, ARBW - 3 dB AR bandwidth, $\mathrm{I_i}$ - Interport isolation within IBW, $\mathrm{A_A}$ - Area of the antenna

Ref.	**$\mathbf{I_i}$ (dB)**	**IBW (%)**	**ARBW (%)**	**$\mathbf{A_A}$ (λ_0)**	**Peak gain (dBic)**	**Radiation pattern**
[?]	10 to 40	4.87	4.87	2.18×2.18	5 to 6.4	Isoflux
[?]	4 to 21	3.2	1.3	0.73×0.68	-4.8 to 7.4	Unidirectional
[?]	20 to 35	4.1 to 5.2	3.2 to 7.7	0.90×0.90	5.8 to 7.2	Unidirectional
[?]	22 to 35	6.69	3.79	1.13×1.13	5 to 9.3	Unidirectional
[?]	10 to 23	23.9	10 and 8.5	0.3×0.3	2.3 to 2.7	Uni/bidirectional
[70]	11 to 23	8.7 and 9.9	4.8	Not given	3.6 to 3.8	Unidirectional
[?]	16 to 30	84.4	33.08	0.45×0.45	0.33 to 3.4	Bidirectional
[?]	20 to 30	10.1 to 20.2	8 to 9.15	1.09×0.76	2.5 to 5.4	Bidirectional
[?]	20 to 30	4.2	6.25	0.41×0.41	3 to 4.5	Bidirectional
This work	17.6 to 46	15.75	11.52	1.14×0.91	3 to 5	Bidirectional

5

Dual circularly polarized slot antenna with split-ring resonator based novel metasurface

---

In this chapter, a DCP full-duplex planar slot antenna suitable for C-band applications is presented. The antenna has a single slot with a T-shaped stub that is shared by both the transmitting (T_X) and receiving (R_X) ports which operate at two mutually orthogonal circular polarizations. A metasurface made up of 4 pairs of face-to-face SRRs acts as a decoupling network to enhance the isolation between T_X and R_X ports. The designed antenna has an impedance bandwidth of 1340 MHz which is 28.52% of the centre frequency $f_0 = 4.71$ GHz. The 3 dB AR bandwidth is 8.97% centred at $f_{AR} = 4.44$ GHz whereas inter-port isolation is better than 27 dB and reaches up to 36 dB within the usable band. The proposed design also exhibits characteristics suitable for MIMO applications.

5.1 Introduction

The radar altimeter (radalt), which were the first radars [?], operate at C-band (4.2 to 4.4 GHz) and is an integral part of modern aeronautical safety system for determining proximity of ground, collision avoidance system, landing, and low-level flight operations for altitudes up to 5000 ft. The antennas prescribed for such radars operate on very low power [?] and should be broad-beamed to function independently of aircraft altitude and flight-dynamics [?]. In such systems, a full-duplex (FDX) antenna with high isolation between $\mathrm{T_X}$ and $\mathrm{R_X}$ is necessary as electronic filtering is less effective at higher altitudes [?]. Moreover, with a two-antenna system, the accuracy reduces at lower altitudes. This is especially problematic during landing where an accuracy of less than one metre is required. Therefore, dual circularly polarized slot antennas or monopole with low gains and FDX feature are preferable [?] for their low weights and volumes are especially useful in unmanned aerial vehicles (UAVs).

In this work, a strictly duplex circularly polarized slot antenna using a novel decoupling unit to reduce SI is presented that is easy to fabricate and compact in size. The antenna slot has a T-shaped stub which is shared by both the T_X and R_X sections. This is similar to the design in [?] with the difference being that in the present work, the T-section alone of the slot is sufficient in generating CP waves in conjunction with the feed-lines and hence has a simpler design. Additionally, in our approach the isolation between the T_X and R_X sections is enhanced by means of a SRR based decoupling metasurface (MS) between two feed-lines on the opposite surface of the slotted ground plane beneath the *FR*-4 substrate. This follows the technique similar to the one in [?] where the MS suppresses the surface waves in the substrate which is the main cause of higher isolation. The proposed design has the major advantage of being inexpensive and low-profile and is suitable for radio altimeter applications, being superior to the contemporary ones in terms of bandwidth [?] and polarization diversity [?, ?, ?]. The antenna can also be used for 5G applications described in [?] as it has sufficient CP bandwidth at 4.5 GHz.

5.2 Antenna geometry

The proposed antenna has been fabricated on an inexpensive *FR*-4 substrate ($\varepsilon_r = 4.3$, $\tan\delta = 0.02$) of 1.6 mm thickness with 1 oz copper on both sides. The dimensions of the antenna are 105 mm × 50 mm. The exploded view of the antenna is shown in Fig. 5.1. The antenna has a rectangular slot cut out of the ground plane as depicted in Fig. 5.2(a). The slot has a T-shaped structure at its base and is excited by two microstrip feed-lines which in turn terminate with T-shaped ends as shown in Fig. 5.2(b) . The metasurface (shown in Fig. 5.1) consisting of SRR unit cells as shown in its close-up view in Fig. 5.3(a) whereas the magnified view of its constituent split ring can be observed in Fig. 5.3(b). The width W_{F1} of the feed is chosen as 3 mm so that the characteristic impedance is 50 Ω and is hence compatible with standard devices.

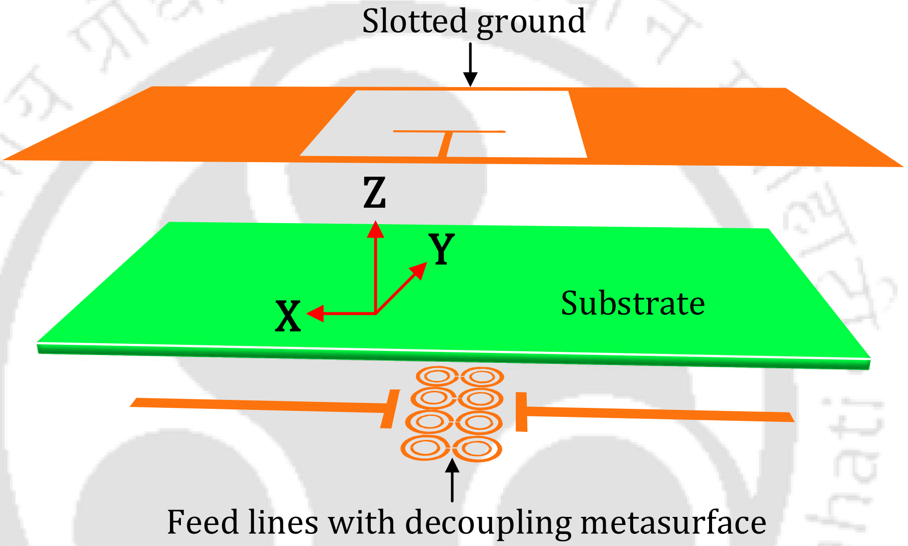

Fig. 5.1: Exploded view of the antenna

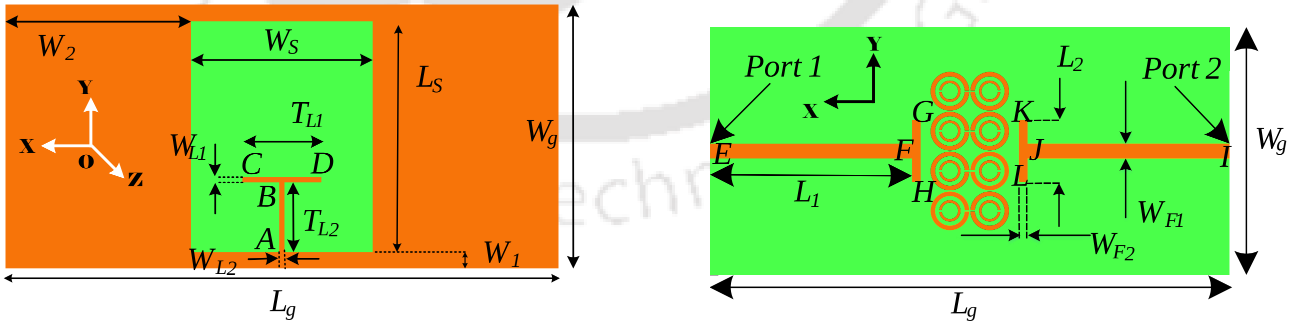

(a)

(b)

Fig. 5.2: Schematic of the antenna (a) Slotted ground and (b) Feed-network

The dimensions of the slot on the ground are roughly chosen using the equation [?]:

$$W = \frac{c}{2f\sqrt{\varepsilon_r}} \tag{5.1}$$

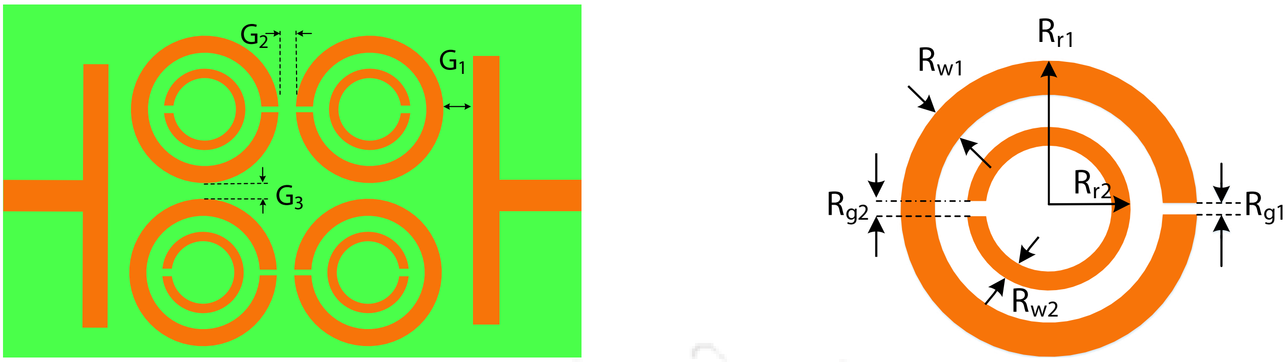

(a) (b)

Fig. 5.3: Schematic of (a) decoupling MS showing 2 pairs of face-to-face SRRs and (b) Enlarged view of a single split ring

where W is the slot dimension, c is the velocity of light in vacuum, f is the operational frequency and ε_r is the effective dielectric constant. From this equation, the initial value of W_s (as in Fig. 5.2(a)) is obtained which is then optimized using CST Microwave Studio for the best performance. The effective width of the slot is further increased by the portion of the T-section AB that yields a high bandwidth. The slot should be long enough for a shift in resonance frequency towards a lower value as seen in [?]. For this reason L_s is initially chosen as 25 mm but because of poor impedance bandwidth and CP performance at the desired band, it is finally optimized to 43.75 mm which is sufficient to be accommodated within the ground-width W_g. The optimized values of all the parameters of Figs. 5.2 and 5.3 are given in Table 5.1.

$\mathrm{G_P}$	Value	$\mathrm{G_P}$	Value	$\mathrm{G_P}$	Value	$\mathrm{G_P}$	Value	$\mathrm{G_P}$	Value
L_g	105	W_2	35.25	L_g	105	W_{F2}	1.75	R_{r2}	1.09
W_g	50	T_{L1}	13.2	W_g	50	G_1	2.00	R_{g1}	1.09
L_S	43.75	T_{L2}	15.00	L_F	41.22	G_2	0.25	R_{g2}	1.09
W_S	34.50	W_{L1}	1.00	L_2	12.50	G_3	0.25	R_{w1}	1.09
W_1	3.13	W_{L2}	1.00	W_{F1}	3.00	R_{r1}	3.70	R_{w2}	1.09

Table 5.1: Values of the geometric parameters ($\mathrm{G_P}$) of Figs. 5.2 and 5.3 (all values are in mm)

5.3 Antenna design evolution

The evolution of the proposed design shown in Fig. 5.4. The first antenna of Fig. 5.4(a) has rectangular microstrip feed lines and a square-slotted ground plane. The second design of Fig. 5.4(b) is very similar to the first one with the only difference being a thin rectangular section on the slotted ground plane. Fig. 5.4(c) has the additional modification of a T-section on the rectangular slot whereas Fig. 5.4(d) shows the final prototype which was implemented for design and experimentation.

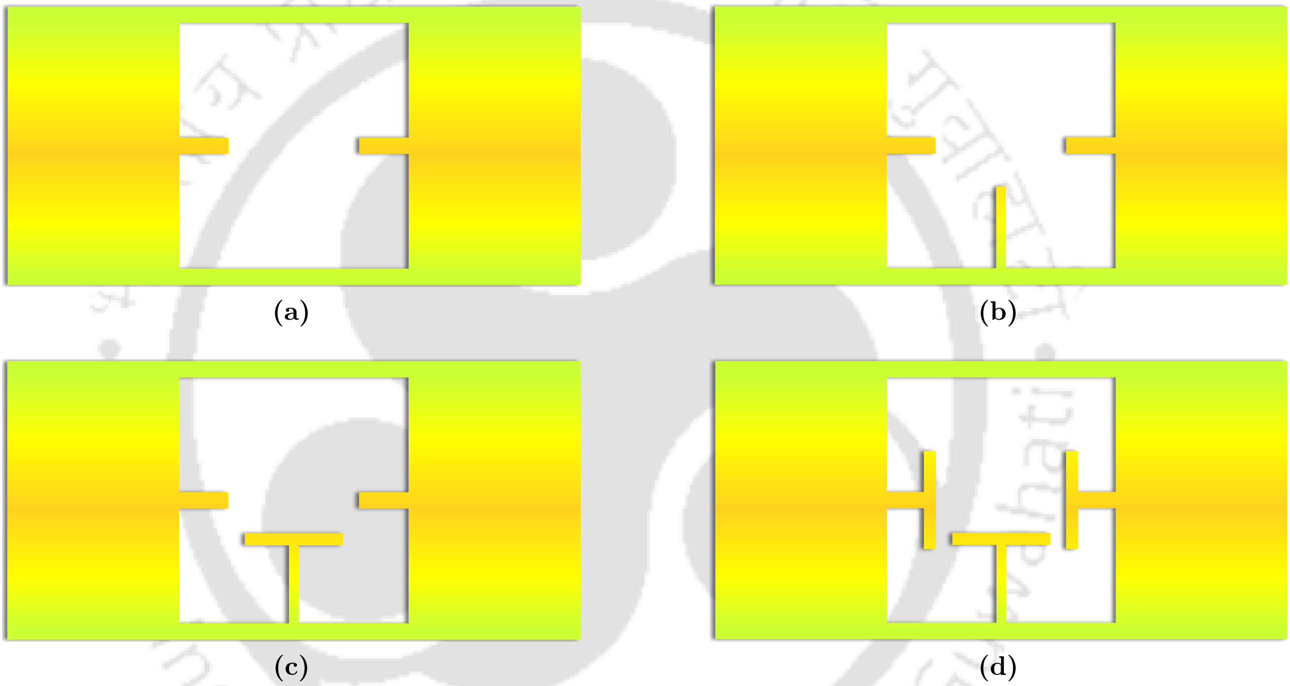
(a) **(b)** **(c)** **(d)**

Fig. 5.4: Evolution of the proposed antenna (without MS) through four different prototypes

Figs. 5.5(a), 5.5(b), 5.5(c), and 5.5(d) show the $|S_{11}|$ parameters, ARs, $|S_{12}|$ parameters and gain of the prototypes versus frequency. It is obvious that Prototype 1 is unsuitable for use as a CP antenna due to very poor impedance bandwidth, high AR $\geq 15\,\text{dB}$ and low gain. Prototypes 2 and 3, in spite of having sufficient 3 dB AR bandwidth, suffer from improper impedance matching and poor gain whereas Prototype 4 is found to be most suitable for DCP operation being free of all the drawbacks with the exception of port-to-port isolation which can be remedied by a decoupling unit. Thus, it can be concluded that the T-section at the terminal of the feed line is essential for good impedance matching.

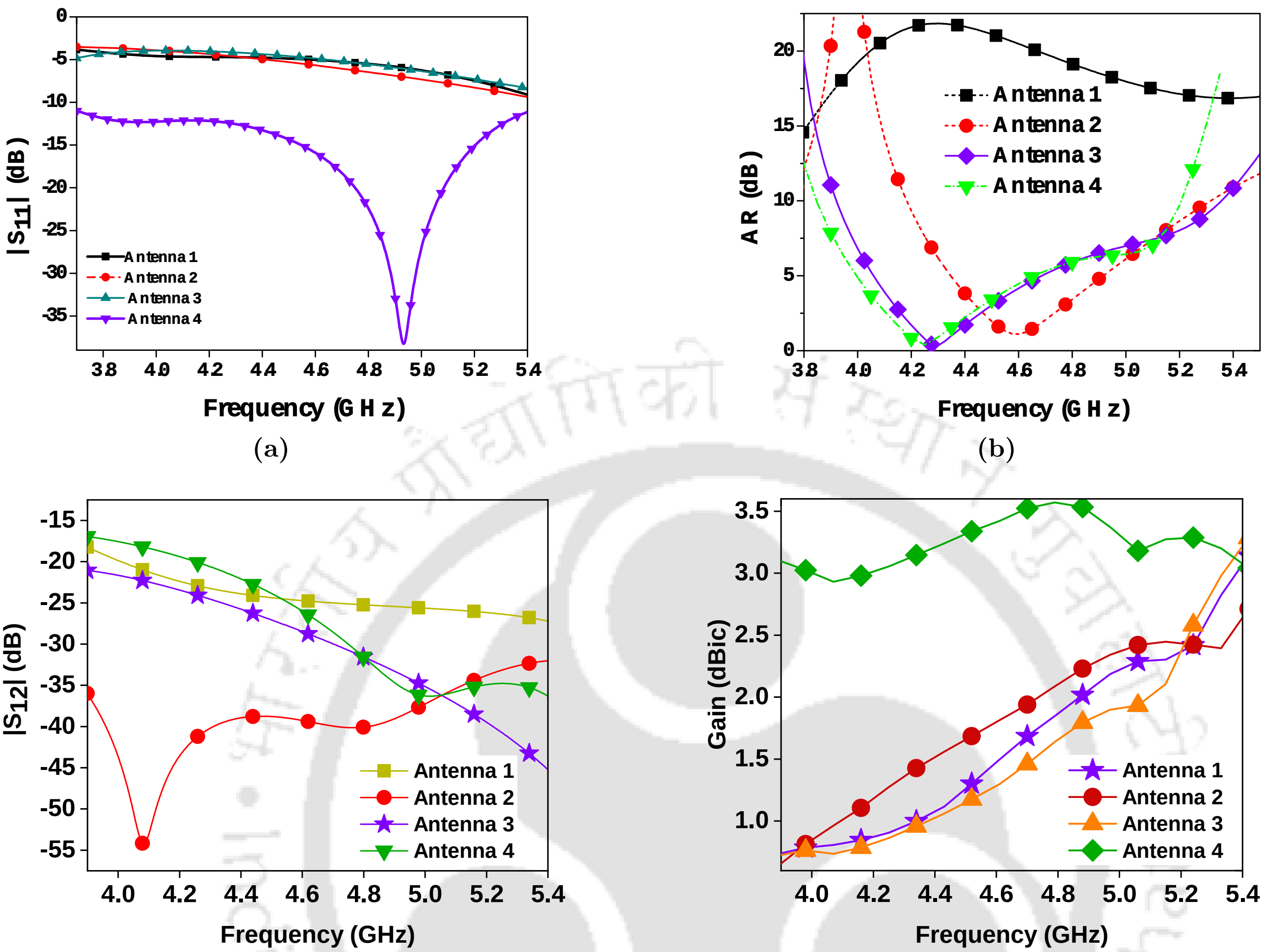

(a) (b)

(c) (d)

Fig. 5.5: Performance of the antenna prototypes: (a) $|S_{11}|$ (b) AR (c) $|S_{21}|$ and (d) Gain at different frequencies

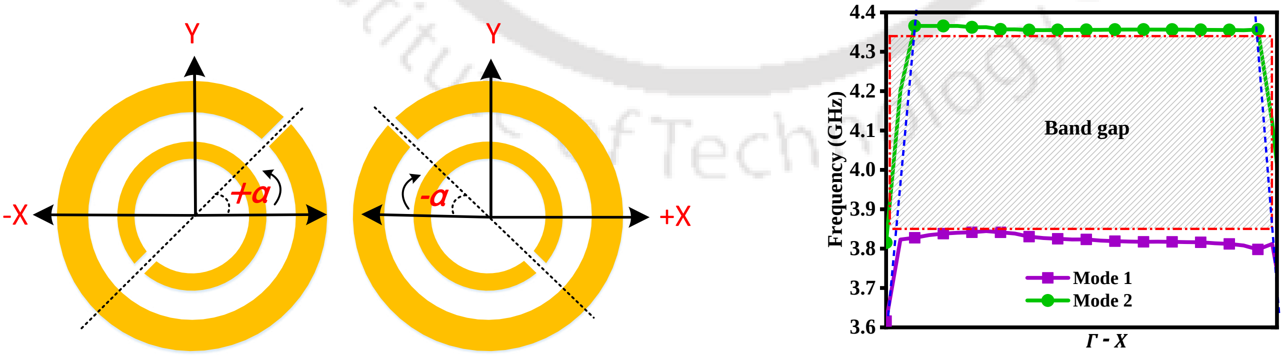

(a) (b)

Fig. 5.6: (a) Schematic of a unit-cell of the MS showing two face-to-face SRRs and (b) $\Gamma - X$ diagram of a unit cell.

5.3.1 Characteristic of the MS unit cell

This section is devoted towards the study of the unit cell of the metasurface (as see in Fig. Fig. 5.6a). Here the word 'metasurface' implies a 2D-array of 'meta'-blocks whose property is markedly different from a conventional 2D array. In fact, based upon its macroscopic property and the role it performs in specific situations, the metasurface may behave as electromagnetic band gap (EBG), high impedance substrate (HIS), frequency selective surface (FSS), to name a few [?]. It should be noted that since the mutual coupling is the strongest in the E-plane along X-axis [?], the unit cells are placed along the X-axis. For the present structure, the $\Gamma - X$ diagram of the first two modes of a unit cell is shown in Fig. 5.6b. The presence of a forbidden band between 3.85 GHz and 4.35 GHz confirms that the structure behaves as an EBG and helps in blocking the surface waves from reaching the other port.

5.3.2 Design of the SRR-based Metasurface

As mentioned earlier, the MS is composed of 4 pairs of SRRs. Here, each unit cell can be viewed to be made up of two SRRs whose slits face each other as shown in Fig. 5.6a. The resonant frequency of a single SRR is determined using the equation given in [?]

$$f_0 = \frac{1}{2\pi\sqrt{L_T C_{eq}}} \tag{5.2}$$

The total inductance L_T is given by [?]:

$$L_T = 0.0002l\left(2.303\log\frac{4l}{d} - \gamma\right) \tag{5.3}$$

where l is the length of the SRR, d is the width of the gap between outer ring and inner ring of SRR, and γ is a constant whose value is 2.451 for a circular SRR.

The equivalent capacitance C_{eq} is given as [?]:

$$C_{eq} = \frac{(\pi r_0 - g)}{2}C_{pul} - \frac{\epsilon_0 R_{w2} h}{2g} \tag{5.4}$$

where r_0 is the average ring-radius, C_{pul} is the capacitance per unit length, R_{w2} is the thickness of the inner ring, h is the thickness of substrate, and $g = 0.5(R_{g1} + R_{g2})$ is the average width of ring splits (Fig. 5.3(b)).

The above equations are utilized to arrive at a starting value of ring dimensions which are then further optimized for resonance at the desired frequency. It is to be noted that since each unit cell has two such rings whose currents mitigate each other, the effective electrical length is less than the one obtained from the equations Eq.(5.2), (5.3) and (5.4).

Simulations showed that the parameters most instrumental for optimum performance of this structure are tilt-angle α of a ring with respect to X-axis (Fig. 5.6a), horizontal gap between the two rings within a unit cell (G_2 as in Fig. 5.3(a)), vertical spacing between two adjacent unit cells (G_3 as in Fig. 5.3(a)), outer ring radius (R_{r1} as in Fig. 5.3(b)), and number of such unit cells.

Fig. 5.7(a) shows the port-to-port isolation and gain versus frequency for different values of α. Here, α is measured in anti-clockwise sense for the left SRR and in clockwise sense for the right SRR. Within the AR bandwidth (i.e. 4.245 GHz to 4.635 GHz), the $|S_{21}|$ values at $\alpha = -60°$ and $0°$ are very close to each other though the gain at the latter tilt-angle (given in Fig. 5.7(b)) is 0.5 to 1 dBic higher than the same at other angles. Hence α is chosen as $0°$ which implies that the slits lie along the X-axis.

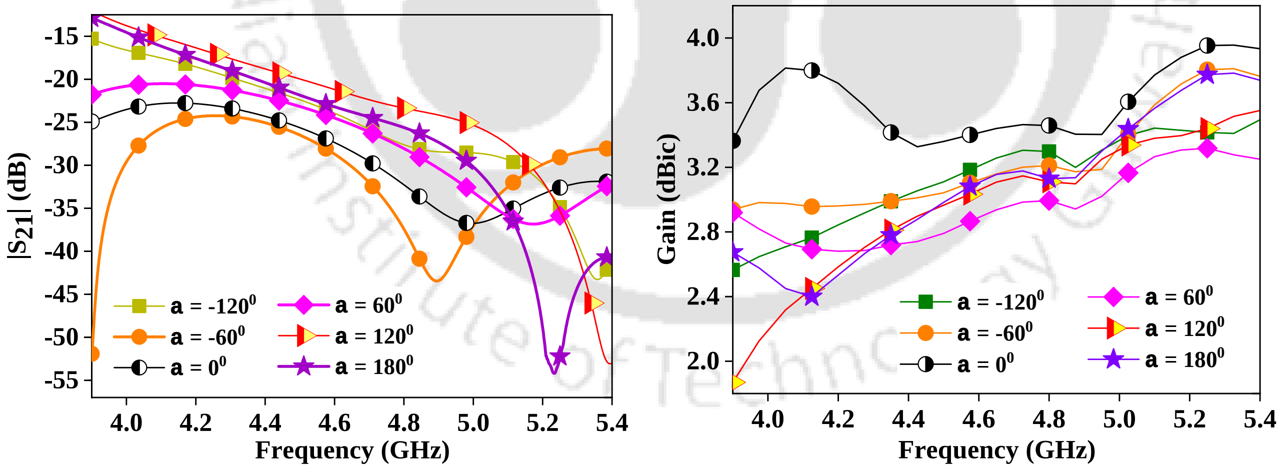

(a) (b)

Fig. 5.7: Variation of (a) $|S_{21}|$ and (b) Gain with respect to frequency at different ring tilt angles α

The tilt-angle α of the slit is vital in deciding the current-direction in the rings. As evident from the surface current plot in Fig. 5.8a, when the angle $\alpha = 90°$, the current vectors become non-coherent and they are no longer cancelled. Instead, the rings starts radiating as their total dimension approaches the resonant frequency. This is also evident from the front-to-back ratio

(FBR) plots (in Fig. 5.8b) at different α which indicates that for a better FBR, the value of α should be non-zero. This is the reason behind poor performance in terms of inter-port isolation and gain for a non-zero α.

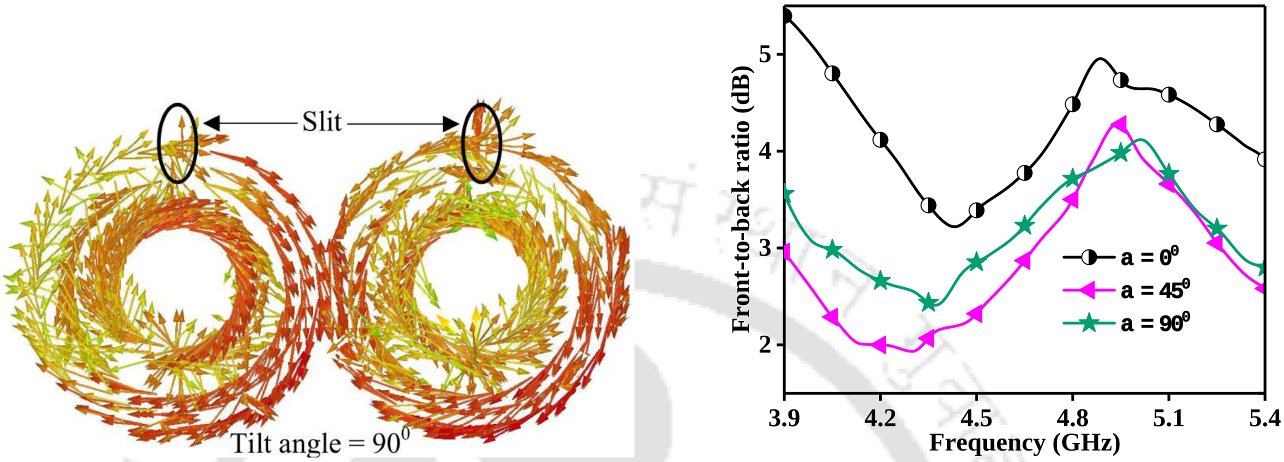

(a) (b)

Fig. 5.8: (a) Surface current distribution on the lowermost SRR pairs of the MS at $f_{AR} = 4.44$ GHz when tilt-angle $\alpha = 90°$ (b) FBR with respect to frequency for different values of α

The effects on $|S_{21}|$ and gain for different values of intra-cell spacing G_2 were studied as shown in Fig. 5.9. This was examined for two close gaps 0.05 mm and 0.25 mm, and a larger spacing of 4.5 mm. It can be observed from Figs. 5.9(a) and 5.9(b) that a larger spacing between the rings within a unit cell has adverse effects on both inter-port isolation and gain. Therefore, G_2 is selected as 0.25 mm as opposed to 0.05 mm for simpler fabrication.

The parameter having a significant influence on the periodicity of the unit cells is designated as G_3 (as in Fig. 5.3(a)) which is the spacing between two adjacent unit cells along the Y-axis. This value was found to be affecting both the inter-port isolation and AR as shown in Fig. 5.10. It is observed that though a larger value of G_3 results in a minor increase in inter-port isolation, it comes at the expense of a diminished AR bandwidth that has a shift towards a higher band. For this reason G_3 was selected as 0.25 mm.

The other two parameters influencing the inter-port isolation are the radius of the outer ring R_{r1} and the number of unit cells as depicted in Figs. 5.11(a) and 5.11(b) respectively. It can be inferred from these plots that for the best possible port decoupling, R_{r1} should be 3.7 mm and the number of unit cells should be 4.

In Fig. 5.12 the effects of horizontal gap (G_2) and vertical gap (G_3) between two adjacent

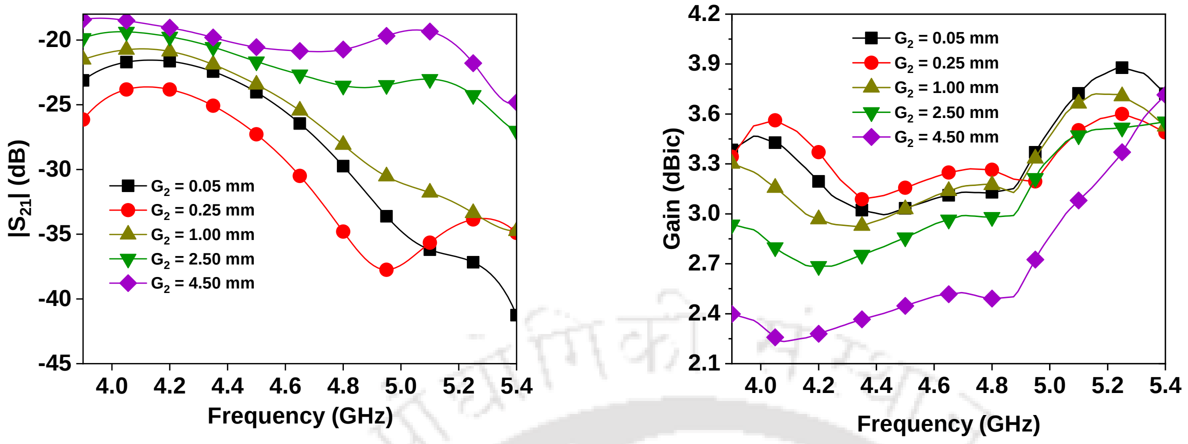

(a) (b)

Fig. 5.9: Variation of (a) $|S_{21}|$ and (b) Gain with respect to frequency for different values of G_2

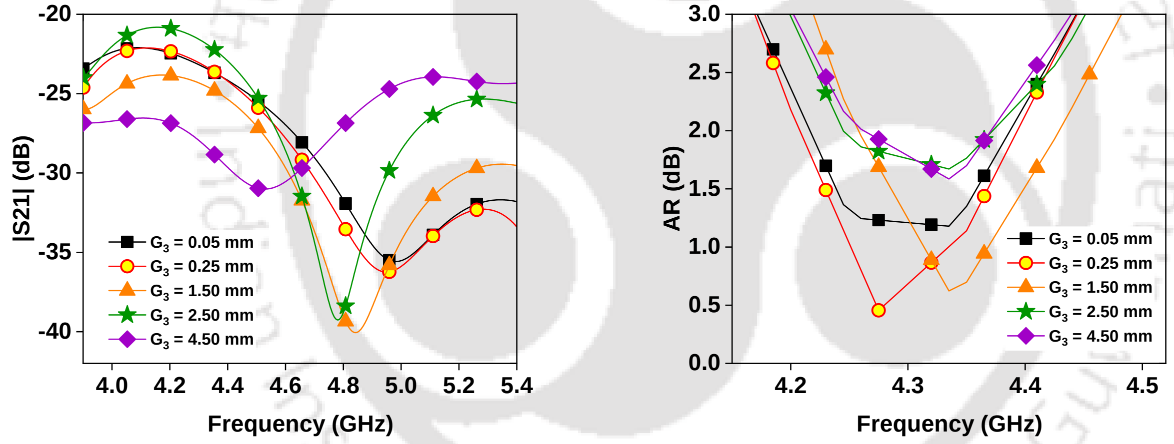

(a) (b)

Fig. 5.10: Variation of (a) $|S_{21}|$ and (b) AR with respect to frequency for different values of G_3

SRRs can be observed. For a very large G_2, the coupling between the SRRs weaken, which adversely impacts the gain. The plot of FBR versus frequency shown in Fig. 5.12a for different values of G_2 confirms this fact. Here it is seen that if the value of G_2 is too large, the FBR reduces which deteriorates the gain and $|S_{21}|$. However, a too small G_2 (G_2 = 0.05 mm) is avoided due to fabrication tolerance.

To understand the effect of a too large vertical spacing between the unit cells, the surface current distribution on the slotted ground is given in the figure below at different phase angles. It is obvious that at G_3 = 4.50 mm the field lines effected so much that the resultant current

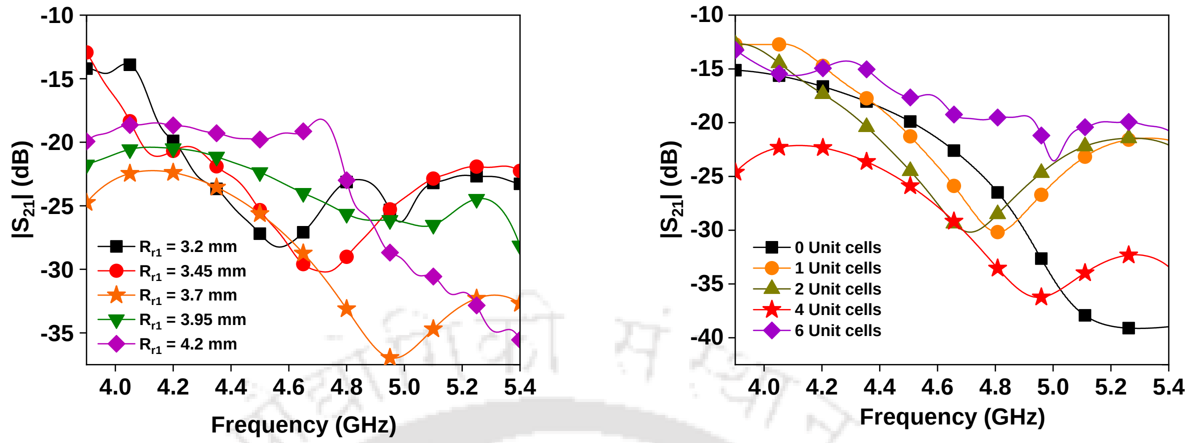

(a) (b)

Fig. 5.11: Variation of $|S_{21}|$ versus frequency for (a) different values of outer ring radius R_{r1} and (b) different numbers of unit cells

vector given by R no longer rotates. This causes the antenna to lose its CP property as evident from the plot of AR versus frequency in Fig. 5.10b.

5.4 Parametric study

It was found through several simulations that the most important parameters for optimum antenna performance were: length of the T-section of the feed L_2 (represented by GH and KL of Fig. 5.2(b)), gap between feed and MS G_1 (as in Fig. 5.3(a)), the length of ground L_g, and the width of the ground W_g (as in Fig. 5.2). The simulated $|S_{11}|$ for different values of L_2 are shown in Fig. 5.13(a). It can be seen that for L_2 less than 12.5 mm, the impedance matching degrades within the desired frequency band whereas the resonant frequency shifts to a higher value for $L_2 = 16.0$ mm. Hence the most suitable value of L_2 is chosen as 12.5 mm.

Fig. 5.14 shows the variation of gain and $|S_{11}|$ with respect to G_1. It is observed that for the best impedance matching and the most stable gain over entire bandwidth, G_1 must be equal to 2 mm.

Fig. 5.15 depicts the inter-port isolation and gain of the antenna for different values of L_g. It is obvious from this figure that while there is a minor improvement in the inter-port isolation the gain improves by 0.5 dBic to 1.2 dBic within the band of 3.9 GHz to 4.6 GHz for $L_g = 105$ mm. Finally, it is also observed that the W_g has an impact on the CP performance

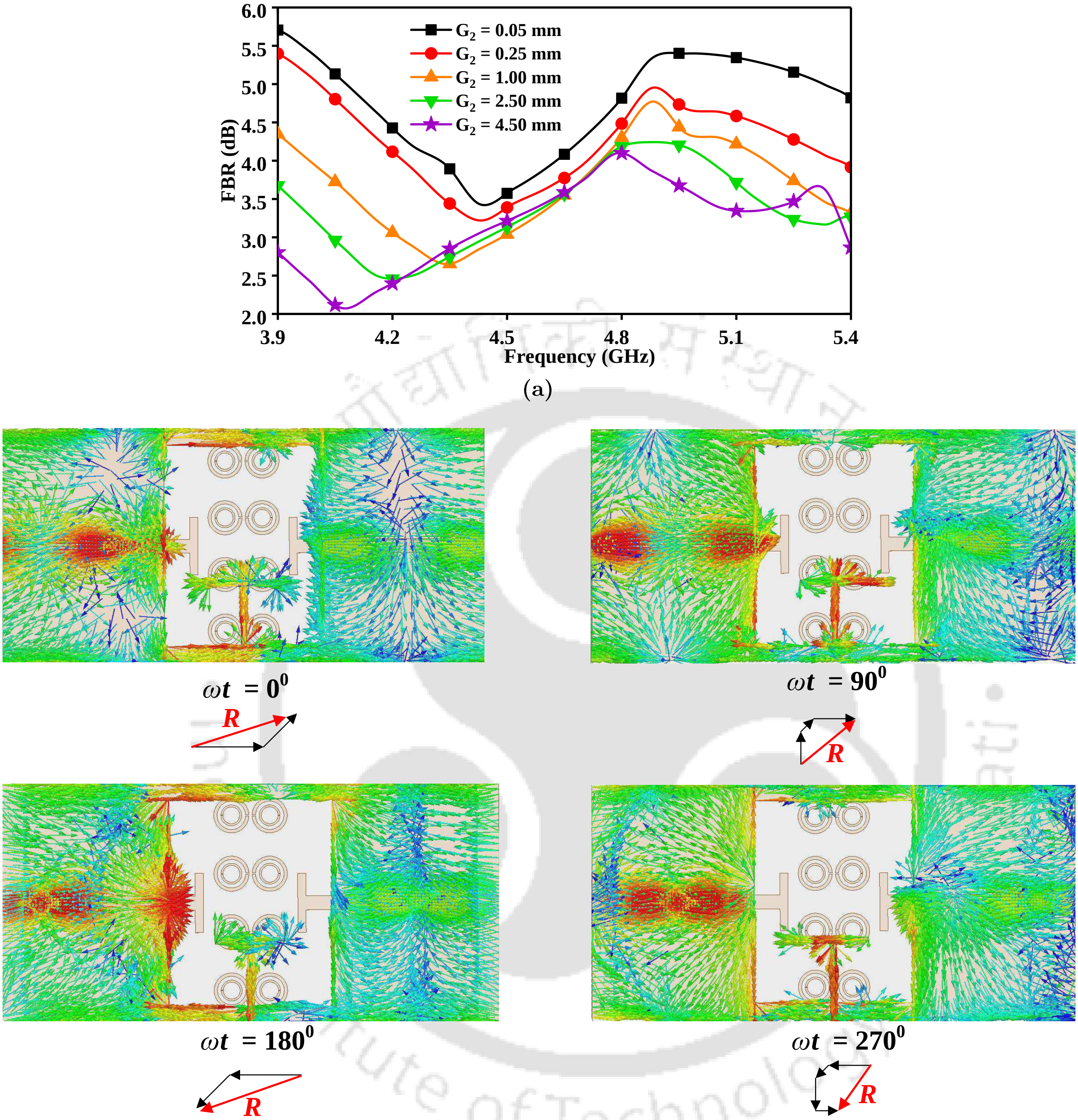

(a)

(b)

Fig. 5.12: Antenna performance due to non-optimal ring-gaps G_2 and G_3 (a) FBR against frequency for different values of G_2 (b) Surface current distribution at different phase angles when the vertical gap between SRR pairs $G_3 = 4.50$ mm at 4.5 GHz. The SRR pairs with large vertical gaps between them can be seen in the background.

of the antenna as shown in Fig. 5.13(b). It can be deduced that for $W_g = 50\,\text{mm}$ the best AR bandwidth is obtained as the other values of W_g yield reduced usable AR bandwidth.

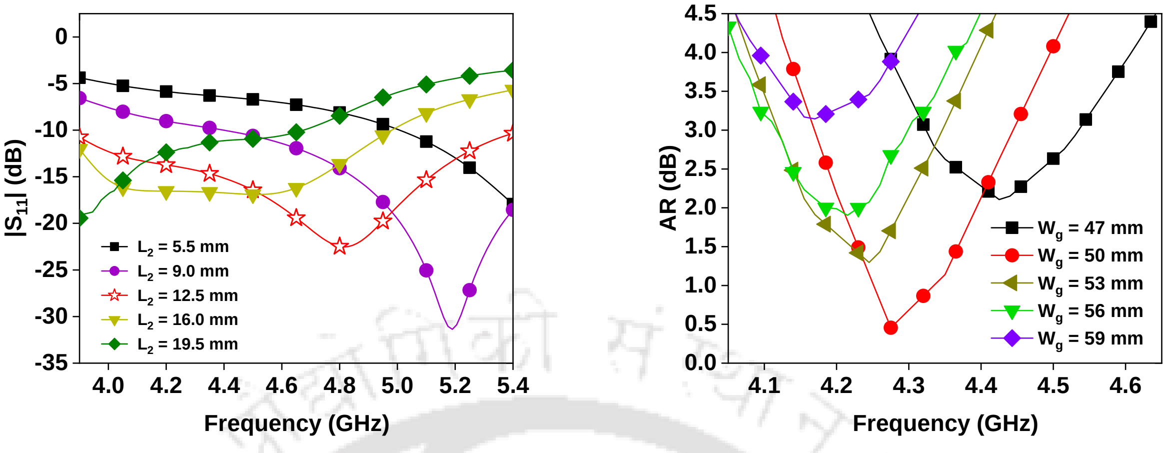

(a) (b)

Fig. 5.13: Variation of (a) $|S_{11}|$ with respect to L_2 and (a) AR with respect to W_g as functions of frequency

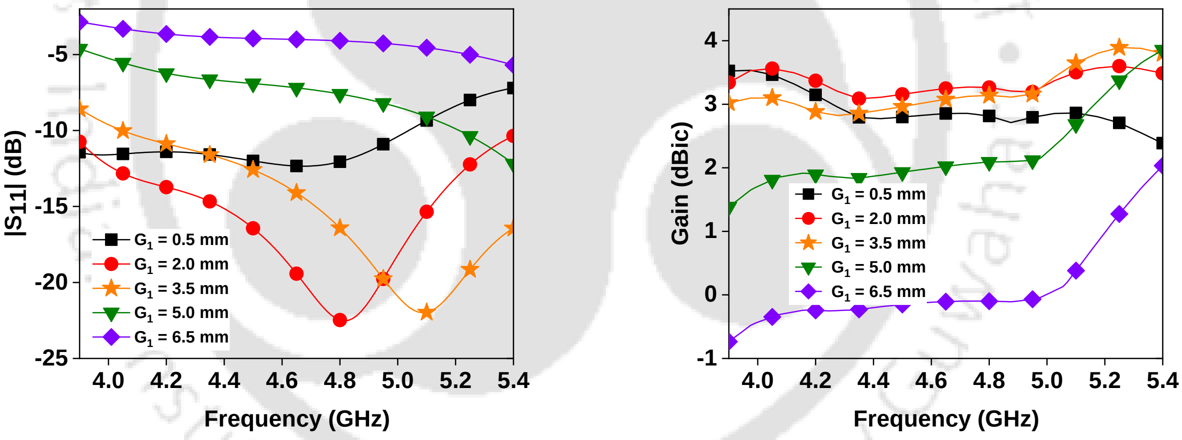

(a) (b)

Fig. 5.14: Variation of (a) $|S_{11}|$ and (b) AR with respect to frequency for different values of G_1

5.5 Results and discussions

The photographs of the fabricated and tested design are shown in Fig. 5.16. For the radiation pattern and AR measurements, port 1 was excited while port 2 was terminated by a matched load, exploiting the antenna symmetry and reciprocity. Fig. 5.17 shows the S-parameters of the antenna. It is seen from the $|S_{11}|$ plot that the -10 dB impedance bandwidth is 1340 MHz lying between 4.03 GHz and 5.4 GHz for $f_0 = 4.71$ GHz. This wideband nature is

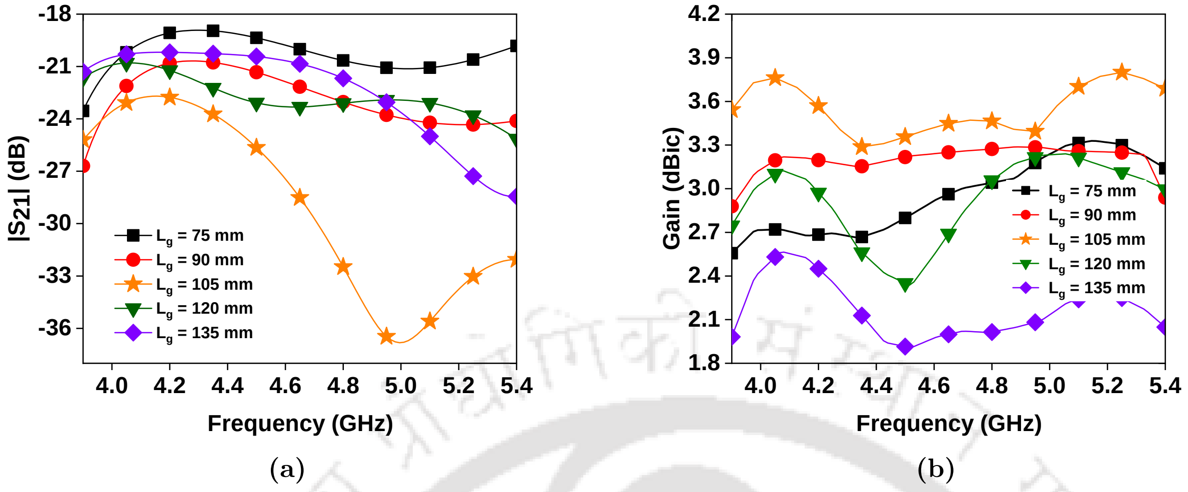

Fig. 5.15: Variation of (a) $|S_{21}|$ and (b) gain with-respect-to L_g as functions of frequency

consistent with that of a planar slot antenna. The same plot also shows the $|S_{21}|$ of the antenna with and without the MS. The difference in levels of $|S_{21}|$ in the two cases is the evidence of the filtering action of the MS. The same figure also shows the measured values of $|S_{22}|$ and $|S_{12}|$ which are almost same as $|S_{11}|$ and $|S_{21}|$ respectively except for minor differences that confirms the symmetric nature of the antenna about its ports.

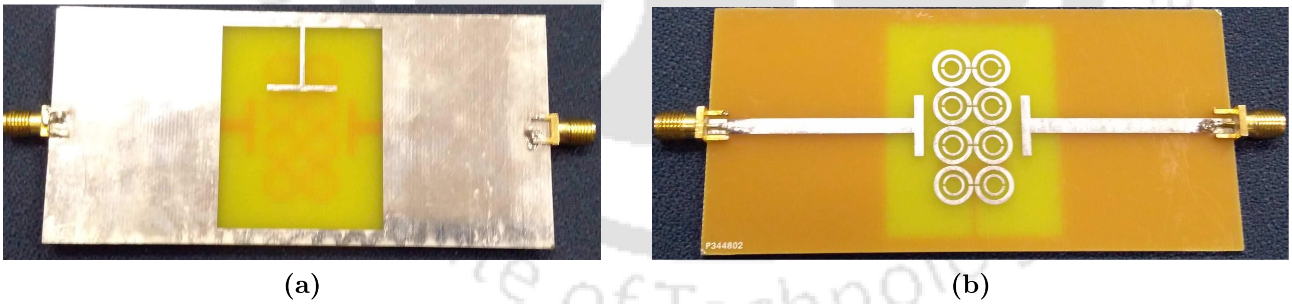

Fig. 5.16: Photograph of the fabricated antenna showing the (a) slotted-ground plane and (b) metasurface with feed lines

Fig. 5.18 shows the current distribution on the lowermost pair of SRRs. As evident, because the currents are induced in the mutually opposite direction in the SRRs, their effects are mitigated and hence the surface waves are attenuated while reaching the opposite port. This results in high inter-port isolation. Fig. 5.19 shows the difference in surface current distribution between the T-sections of the T_X and R_X ports with and without the MS which further confirms the role of the MS in port decoupling.

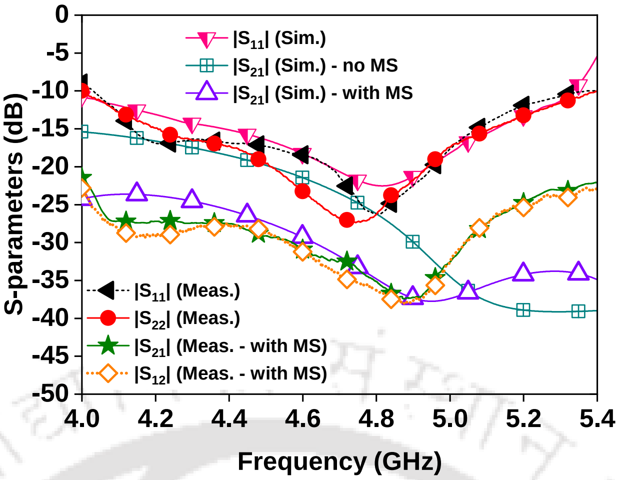

Fig. 5.17: Plots of simulated and measured S-parameters versus frequency

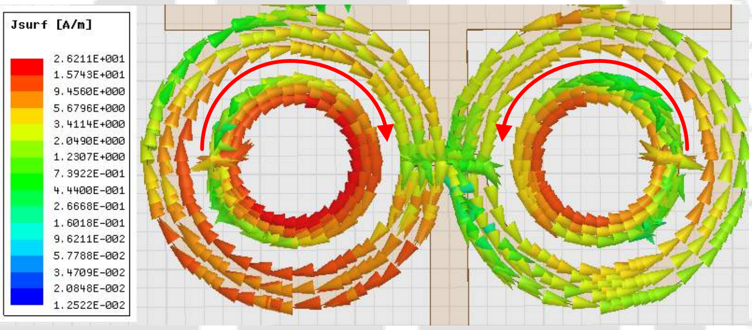

Fig. 5.18: Surface current distribution on the lowermost SRR pairs of the MS at $f_{AR} = 4.44\,\text{GHz}$

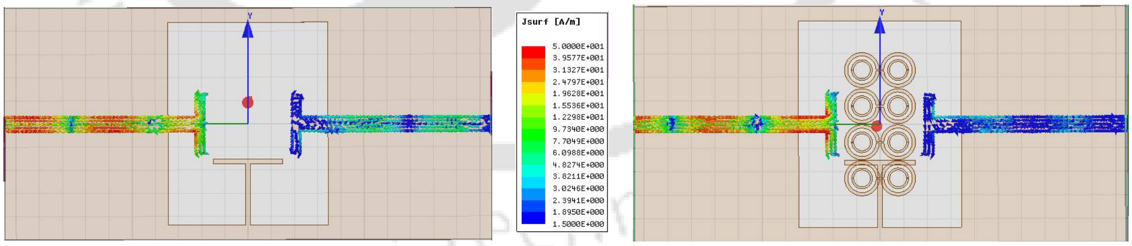

Fig. 5.19: Surface current distribution on the feed-lines without and with the MS at $f_{AR} = 4.44\,\text{GHz}$

Fig. 5.20 shows the surface current distribution on the slotted ground. Since Port 1 has been excited, the surface currents have higher magnitude on the right side of the slot. The vector sum of the current components at each of the phase angles is shown by red colored arrow. Due to the clockwise spinning of the tip of the resultant vector LHCP mode is generated at $z > 0$ plane.

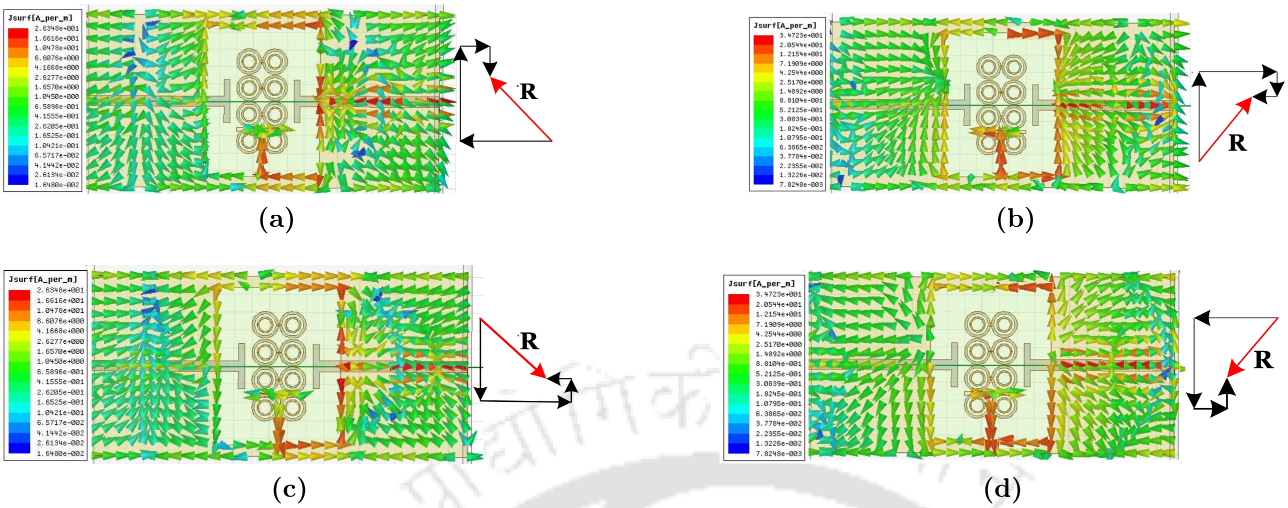

(a) (b)

(c) (d)

Fig. 5.20: Current distribution around excited slot at $f_{AR} = 4.44$ GHz (a) $\omega t = 0°$, (b) $\omega t = 90°$, (c) $\omega t = 180°$, and (d) $\omega t = 270°$

Fig. 5.21 shows the 3 dB AR bandwidth and the gain with respect to frequency. The AR bandwidth is 390 MHz which is 8.97% of the centre frequency $f_{AR} = 4.44$ GHz. At this band the isolation (with the MS) is better than 27 dB which is a significant improvement of about 10 dB over the same antenna without the MS. The gain of the antenna is fairly constant over its AR bandwidth and ranges from 3 dBic to 3.4 dBic.

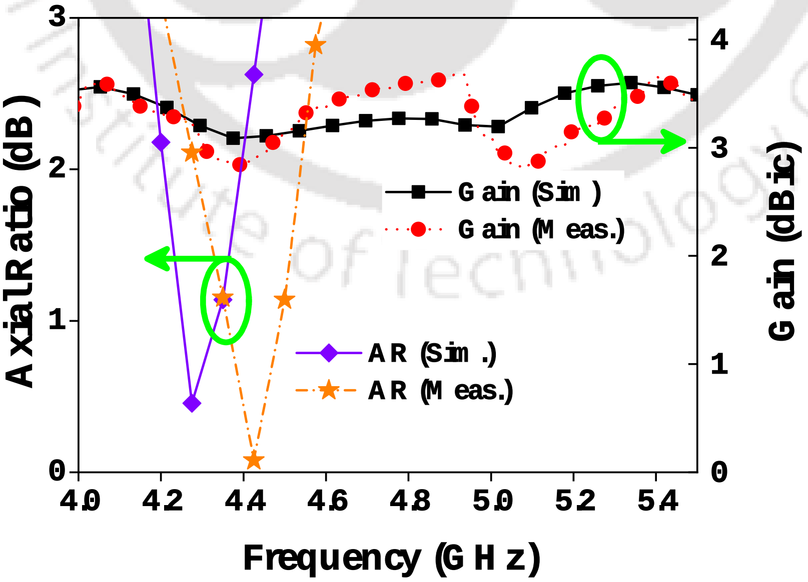

Fig. 5.21: AR and gain versus frequency

The *xz*-plane and *yz*-plane radiation patterns are shown in Fig. 5.22. It is seen from Fig. 5.22(b) that the peak power difference between the LHCP and RHCP pattern is around 24 dB with the main lobe directed at 28°.

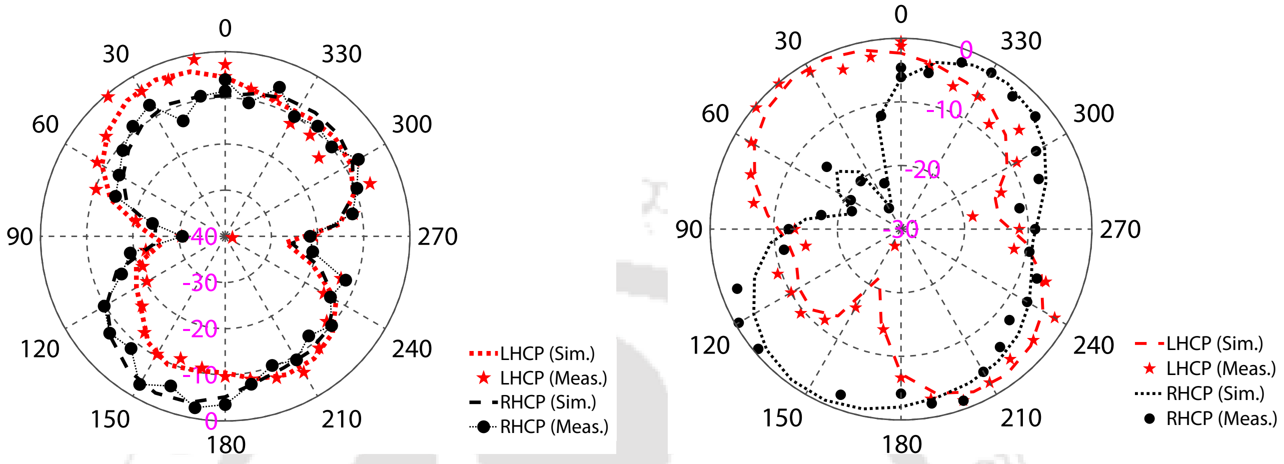

(a) (b)

Fig. 5.22: Radiation pattern at $f = 4.44\,\text{GHz}$ (a) *xoz*-plane and (b) *yoz*-plane

5.5.1 MIMO Performance

As in the previous chapter, for the proposed antenna, ECC is calculated to be less than 0.028 for practical purposes. Also the diversity gain is found to be stable at 10 dB. Thus it can be concluded that the antenna performs satisfactorily as a MIMO antenna. The plot of ECC (ρ_e) and *DG* (in dB) is shown in Fig. 5.23.

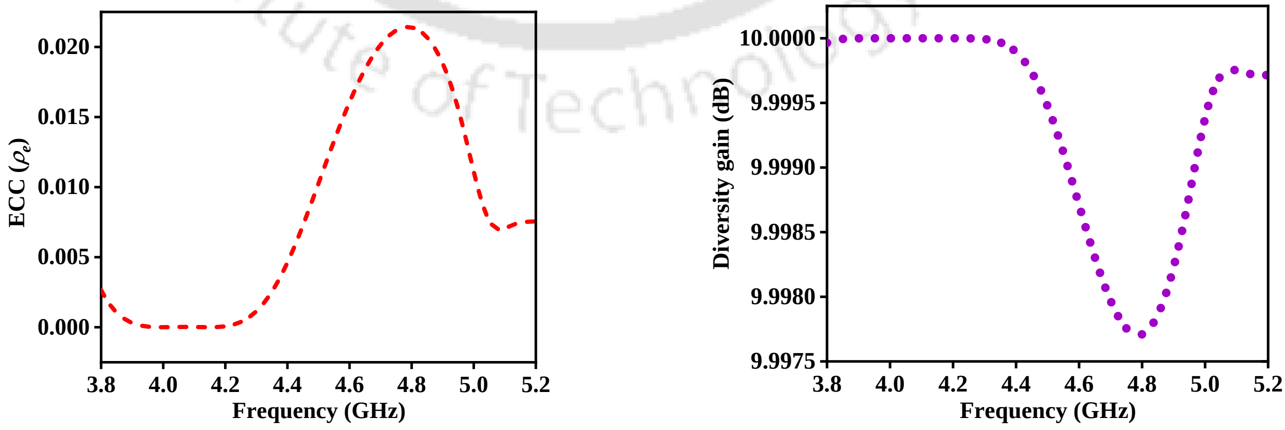

(a) (b)

Fig. 5.23: Radiation pattern at $f = 4.44\,\text{GHz}$ (a) *xoz*-plane and (b) *yoz*-plane

5.5.2 Augmentation of gain

It is well-known that lossy substrates with high loss-tangent ($\tan\delta$) can yield low antenna gains [?]. Hence, it becomes necessary to examine the antenna performance for different substrates and explore the possibilities of augmenting the gain. Fig. 5.24(a) shows the simulated efficiency of the antenna when different substrates (tabulated in Table 5.2) are used. The substrates chosen have close relative permittivities for a meaningful comparison. As expected, the substrate FR-4 with highest loss tangent ($\tan\delta$) is the least efficient when used in the antenna compared to the low-loss ones. Fig. 5.24(b) depicts the effect on antenna gain due to usage of different substrates. Here again, it is confirmed that a low-loss substrate yields higher gain.

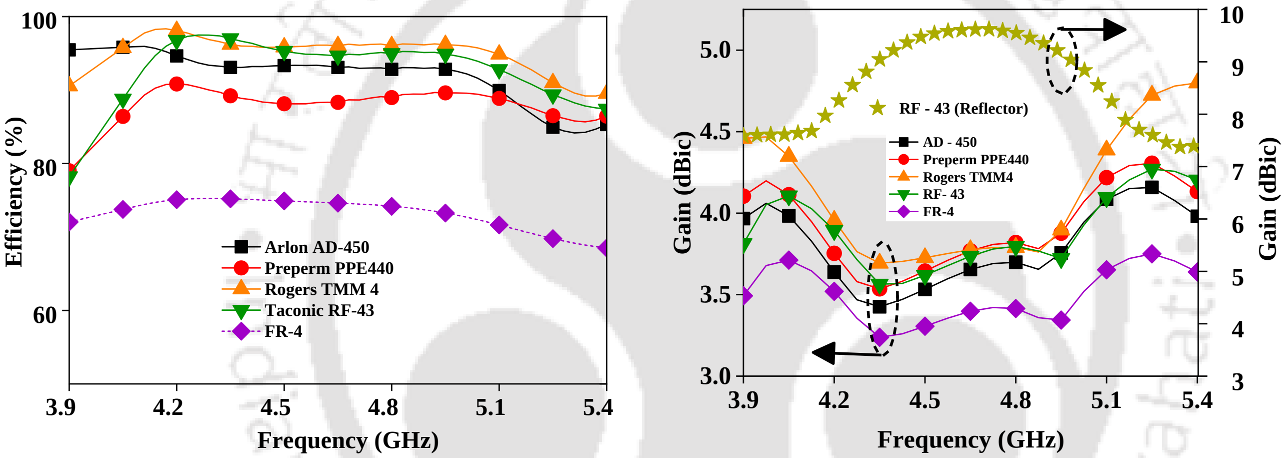

(a) (b)

Fig. 5.24: Performance of the antenna for different substrates (a) Efficiency and (b) Gain versus frequency

The surface wave has an important role in antenna performance. As established in [?], the surface waves are dependent upon the filling material i.e. the dielectric constant of the substrate. An excess of this mode affects the mutual coupling between the elements and the FBR of the antenna. Keeping this fact into consideration, the plots of FBR and $|S_{21}|$ are in Figs. 5.25. As expected, a low ε_r substrate has a higher FBR and lower mutual coupling both of which worsen at higher dielectric constants.

As mentioned earlier, the gain is moderate due to the bi-directional pattern of the slot antenna. In such a case usage of a metallic reflector on one side is suggested to improve the gain [?, ?]. However reflectors have been known to adversely affect the CP performance as seen in [?]. Therefore the functionality of the antenna in terms of both gain and AR bandwidth

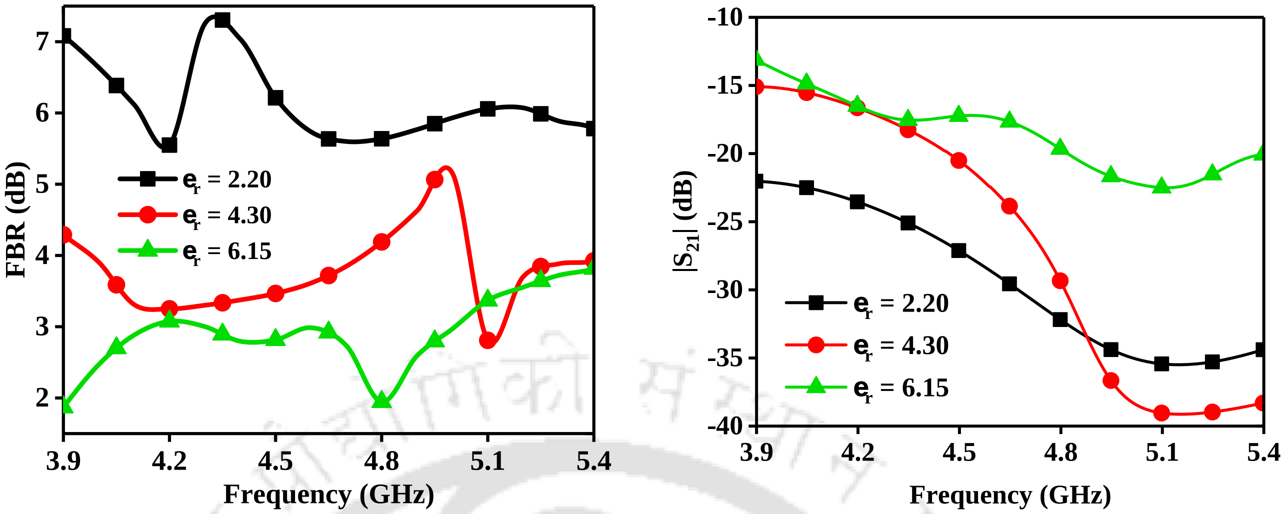

(a) (b)

Fig. 5.25: Effect of substrate dielectric constant ε_r on the performance of the antenna (without the metasurface) (a) Plot of FBR against frequency for different values of ε_r and (b) Plot of $|S_{21}|$ against frequency for different values of ε_r

Table 5.2: Comparison of properties of different substrates

Substrate	Relative permittivity (ε_r)	Loss tangent (tanδ)	Thickness
FR-4	4.3	0.02	1.6 mm
Arlon AD-450	4.5	0.0035	1.52 mm
Rogers TMM4	4.5	0.002	1.52 mm
Preperm PPE440	4.4	0.009	1.6 mm
Taconic RF-43	4.3	0.0033	1.57 mm

(with Taconic RF-43 substrate) is examined by placing a copper reflector (135 mm×65 mm) at a distance of $h_p = 7.5$ mm beneath the microstrip feed lines as shown in Fig. 5.26(a). With this arrangement, the gain is substantially increased to > 7.5 dBic as seen from Fig. 5.24(b). The CP performance of the antenna remains largely unaffected and the AR bandwidth undergoes a minor increase as seen in Fig. 5.26(b). In practical situations requiring high gain, the antenna may be placed at a distance h_p away from a metallic wall which will act as a reflector.

The Table 5.3 gives a comparison of performances between the proposed antenna and other contemporary antennas. It is seen that this design performs better in almost all the parameters apart from gain. The moderate gain is due to low Front-to-Back Ratio (FBR) which is a

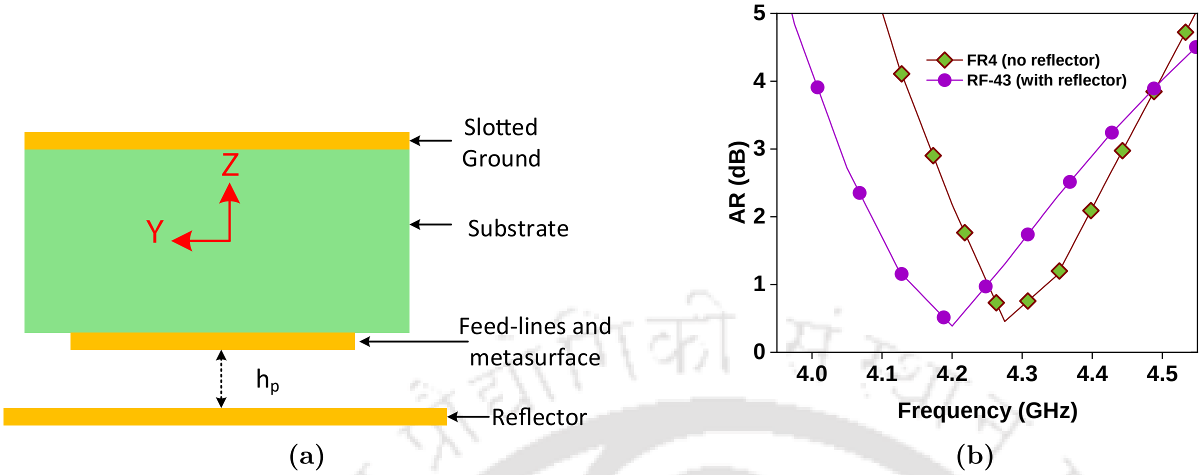

(a) (b)

Fig. 5.26: Antenna with reflector (a) schematic and (b) AR versus frequency

characteristic of slot antenna and is compensated by fairly omni-directional radiation pattern. Moreover, the beam-width is greater than 45° in all planes that is ideal for radalt as discussed before.

5.6 Summary

This chapter proposes a DCP antenna (for both polarizations) with a single radiating slot suitable for radio altimetry in UAVs due to its lightweight. A metasurface based on a 4×2 array of split-ring resonators in this case helps to attenuate the surface waves from the transmitting port to the receiving port, which is instrumental in achieving very high port isolation. From the dispersion diagram, the metasurface unit cells are seen to behave as EBGs. This antenna features a large impedance bandwidth of 28.52% and a high interport isolation of 27 to 36 dB within its AR bandwidth centered at 4.44 GHz, the latter being 390 MHz wide. The key drawback of this antenna's low gain can be easily overcome by adding a metallic reflector to block the lobe behind it. It is also suited as a diversity antenna for 5G MIMO applications due to its low ECC.

Table 5.3: Comparison of proposed DCP antenna with other recently reported antennas

Ref.	Isolation (dB)	−10 dB B.W.	BW_{AR}	Antenna dimensions (λ_0)	Gain (dBic)
[?]	15 to 28	13.23% & 9.52%	7.8%	$0.73 \times 0.73 \times 0.0036$	−3.5 to 4.3
[?]	12 to 25	23.69% and 18.5%	12.5% & 14.7%	$3.54 \times 1.69 \times 0.2768$	4 to 10.7
[?]	10 to 40	4.87%	4.87%	$2.18 \times 2.18 \times 0.22$	5 to 6.4
This work	27 to 36	28.52%	8.97%	$1.58 \times 0.75 \times 0.024$	2.9 to 3.6

6

Dual circularly polarized microstrip patch antenna with multifunction DGS

A two-port planar DCP microstrip patch antenna is presented. The designed antenna has two groups of patches, one each for transmission and reception. In one such group, only the central patch with truncated opposite corners is probe-fed, whereas the surrounding patches act as parasitic patches for bandwidth and gain enhancement. A DGS consisting of 4 units of complementary square spiral resonators is used to enhance the port-to-port isolation as well as the AR bandwidth. Based on the measured data of the fabricated prototype, the antenna is seen to have an impedance bandwidth of 900 MHz with the centre frequency of $f_0 = 6.40$ *GHz. Moreover, the axial ratio (AR) bandwidth is measured to be 600 MHz at* $f_{AR} = 6.36$ *GHz, whereas the peak gain within this band is found to be ranging from 6.8 dBic to 7.9 dBic. It is also noted that the AR bandwidth lies entirely within the impedance bandwidth and the cross-polarisation discrimination is 20 dB in the boresight direction.*

6.1 Introduction

In this chapter, a coaxial probe-fed DCP patch antenna that is composed of two different excited patches located centrally for each type of polarization - left-handed CP (LHCP) and right-handed CP (RHCP) is presented. These patches are surrounded by parasitic elements such that the overall structure has a high gain and bandwidth, as demonstrated in [?, ?]. In the proposed antenna, a type of defected ground structure (DGS) is etched on the ground plane which are used for enhancing the isolation between the ports [?] because of their band-reject property [?, ?, ?]. The usages of DGS have also been reported for higher-order harmonic suppression [?], cross-polarization reduction [?, ?], and improved impedance matching in planar CP antennas [?]. Apart from increasing the inter-port isolation, the DGS presented here also plays a role in augmenting the AR bandwidth of the antenna. To the best of the author's knowledge, applying DGS for the dual role of port-decoupling and AR bandwidth enhancement in a DCP antenna is still a relatively unexplored area. The DGS employed in this antenna is made up of spiral resonators which are preferred for their compactness and less unwanted interference among adjacent DGS units [?, ?].

6.2 Antenna design

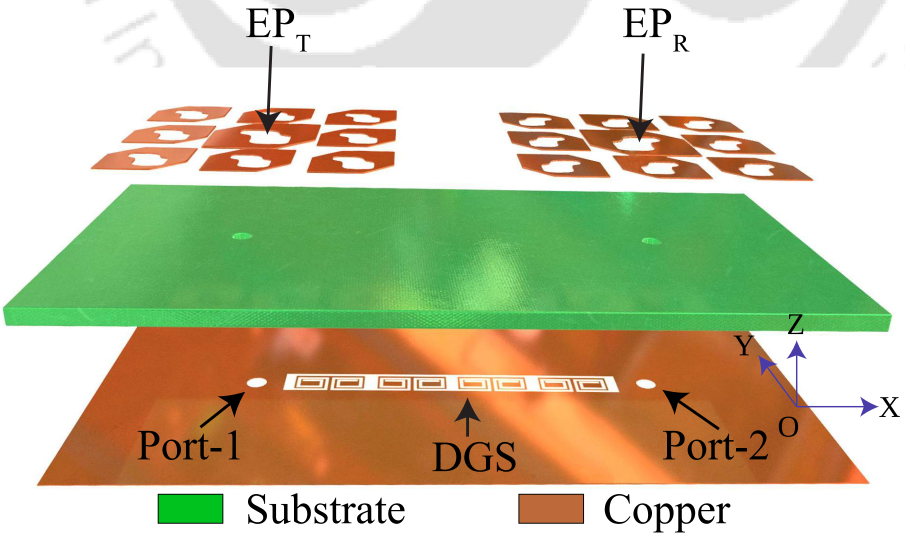

Fig. 6.1: Exploded view of the antenna showing the excited patches ($\mathrm{EP_T}$ and $\mathrm{EP_R}$), surrounding parasitic patches, substrate, and ground plane with ports and DGS

The exploded view of the designed antenna is shown in Fig. 6.1 indicating the different layers. The proposed antenna has been fabricated on FR-4 substrate ($\varepsilon_r = 4.3$, $\tan\delta = 0.02$) of 1.6 mm thickness. As seen in Fig. 6.2(a), the antenna has two groups of 3×3 patches named $\mathrm{T_X}$ patches and $\mathrm{R_X}$ patches of which only the central patches from each of the groups are coaxial probe-fed and are named as Excited Patches ($\mathrm{EP_T}$ and $\mathrm{EP_R}$) for transmission ($\mathrm{T_X}$) and reception ($\mathrm{R_X}$) operations respectively. The remaining 8 patches from each group are the parasitic patches which help in enhancing the bandwidth and the gain of the antenna. The patches of the $\mathrm{T_X}$ and $\mathrm{R_X}$ groups have truncated diagonal corners in opposite orientation to excite two mutually orthogonal circular polarisations in each of them [?]. The magnified view of a central driven patch and a surrounding parasitic patch is shown in Fig. 6.2(b). Each of the patches has a pair of interconnected asymmetrical rectangular slots which help in lowering the resonant frequency of the antenna, and also aid in design optimisation by providing more number of controllable parameters. The edges of the truncated triangular corners of $\mathrm{EP_T}$ and $\mathrm{EP_R}$ satisfy the following relationship as given in [?]

$$f'_{AR} = f_{UP}\left[1 + \frac{S_T}{2S_{UP}}\right] \tag{6.1}$$

Here, f'_{AR} is the is frequency of optimum axial ratio (AR), f_{UP} is the unperturbed frequency of the patch, S_T is the total area of the truncated regions, and S_{UP} is the area of unperturbed patch. From Fig. 6.2(b), $S_T = 13.69\ \mathrm{mm}^2$, $S_{UP} = 121.00\ \mathrm{mm}^2$, and f_{UP} is calculated to be 6.32 GHz. Therefore f'_{AR} is 6.67 GHz.

The DGS on the ground plane is made up of 4 units of Complementary Square Spiral Resonator (CSSR) as shown in Fig. 6.3. A close-up view of a single unit is shown in Fig. 6.3(b). The structure acts as a bandstop filter by suppressing the surface waves incident from the excited patch ($\mathrm{EP_T}$) [?], thereby increasing the isolation between the antenna ports.

The optimized values of all the geometrical parameters are given in Tables 6.1 and 6.2.

6.3 Antenna evolution

The final design is arrived at through six stages using six different prototypes, as shown in Fig. 6.4. Prototype 1 is the simplest of all, with just two excited patches whose opposite corners are truncated. Prototype 2 is a modification of Prototype 1 in which an individual excited patch is surrounded by 8 square-shaped parasitic patches. The parasitic patches are

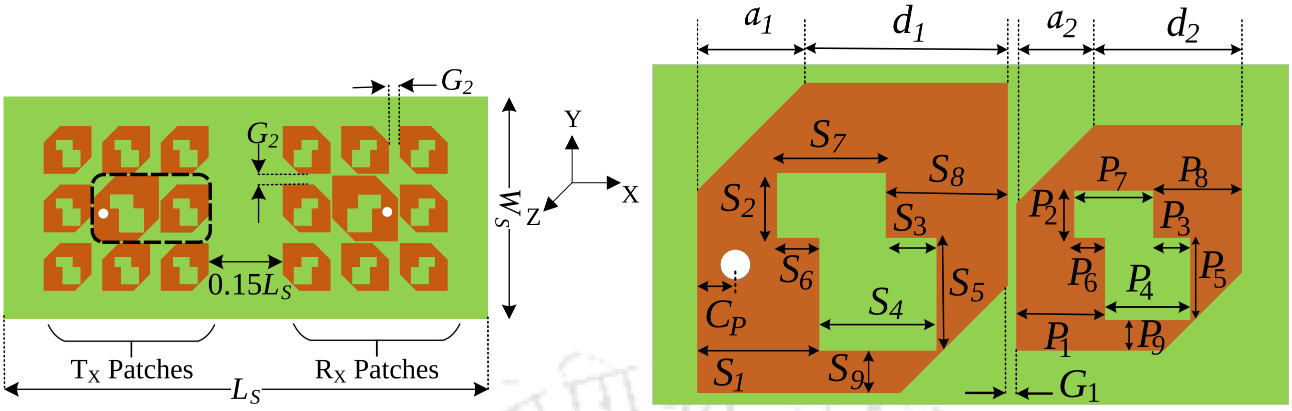

(a) (b)

Fig. 6.2: Antenna geometry showing the (a) groups of patches and (b) magnified view of the dashed rectangular region of patches of T_X group. The white dots on the patches $\mathrm{EP_T}$ and $\mathrm{EP_R}$ represent the locations of the coaxial probes whereas C_P represents the position of the probe with respect to the edge of the patch.

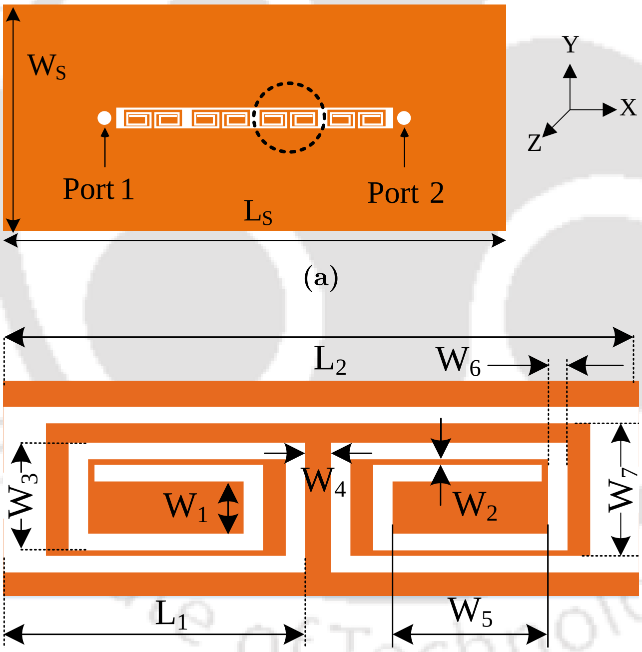

(a)

(b)

Fig. 6.3: (a) Ground plane of the antenna and (b) magnified view of the dashed circular region of DGS.

further modified to have truncated opposite corners, as shown in Prototype 3. Each of the excited patches is provided with a pair of conjoined rectangular slots as shown in Prototype 4. In prototype 4A, keeping the slots intact on the excited patches, the corners of the parasitic patches are truncated. In prototype 5, the conjoined slots are provided even on the parasitic

Table 6.1: Values of the geometric parameters of Fig. 6.2 (all values are in mm).

Parameter	Value	Parameter	Value	Parameter	Value
a_1	3.70	S_6	1.50	P_6	1.09
a_2	2.68	S_7	3.85	P_7	2.80
d_1	7.30	S_8	4.33	P_8	3.15
d_2	5.32	S_9	3.15	P_9	2.29
S_1	4.33	P_1	3.14	C_P	3.90
S_2	2.30	P_2	1.67	G_1	0.30
S_3	1.80	P_3	1.31	G_2	1.80
S_4	4.15	P_4	3.02	L_S	81.00
S_5	4.00	P_5	2.91	W_S	42.50

Table 6.2: Values of the geometric parameters of Fig. 6.3b (all values are in mm).

Parameter	Value	Parameter	Value	Parameter	Value
L_1	4.75	W_1	0.95	W_3	1.95
L_2	9.90	W_2	0.10	W_4	0.40
W_5	2.40	W_6	0.30	W_7	2.40

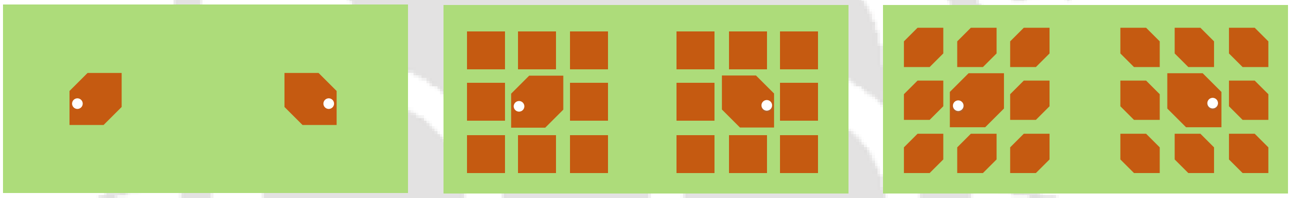

Prototype 1 Prototype 2 Prototype 3

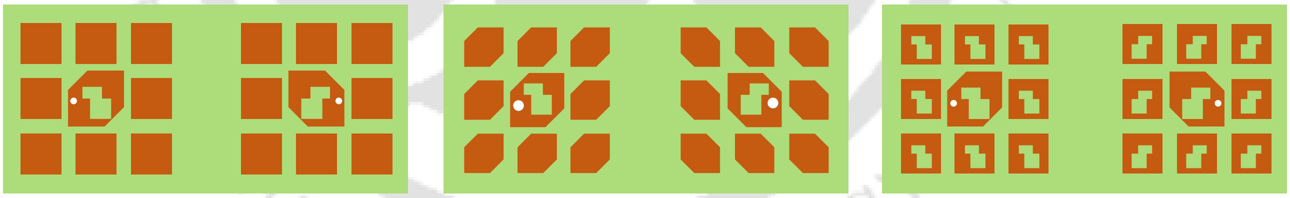

Prototype 4 Prototype 4A Prototype 5

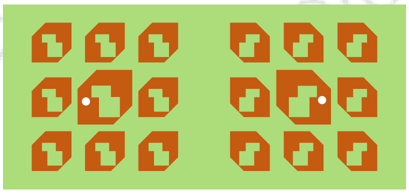

Prototype 6

Fig. 6.4: Stages in antenna design through different prototypes. It is to be noted that none of the prototypes has the DGS on the ground plane. The white dots on the excited patches at the centres represent the locations of coaxial probes.

patches whereas in the final prototype, i.e. Prototype 6, both the excited and the parasitic patches have corner truncations as well as slots.

The plots of AR, gain and $|S_{11}|$ versus frequency for the different prototypes are shown in Figs. 6.5 , 6.6(a), and 6.6(b) respectively. It is evident that Prototypes 1 and 2 have little use as DCP antennas due to their high AR, even though they resonate at lower frequencies. However, it is to be noted that the presence of parasitic patches in Prototype 2 significantly enhances the gain. Prototype 3 has much lower AR in contrast to Prototype 4 though the former fails the threshold of being ≤ 3 dB, whereas the latter has a lower resonance frequency. This implies that, at the lower frequencies, the corner truncations of the parasitic patches are vital for a good CP performance, whereas the slots in the excited patches are instrumental in good impedance matching and improved gain. Therefore, combining the features of Prototypes 3 and 4, Prototype 4A is designed that has a low AR as well as a lower resonant frequency compared to that of Prototype 3. It is also evident from Fig. 6.5 that the slots in the parasitic patches as in Prototype 5 are essential for a lower AR. Thus, the role of the conjoined slots is vital for both antenna miniaturization and better AR performance by introducing two mutually orthogonal modes of almost equal amplitudes modes in the patches that is essential for CP waves which have been extensively studied in [?] and [?]. Therefore, for optimum performance, Prototype 6 is chosen, which incorporates the features of the other prototypes namely large impedance bandwidth, low AR (≤ 3 dB) over a wider range of frequencies, and high gain.

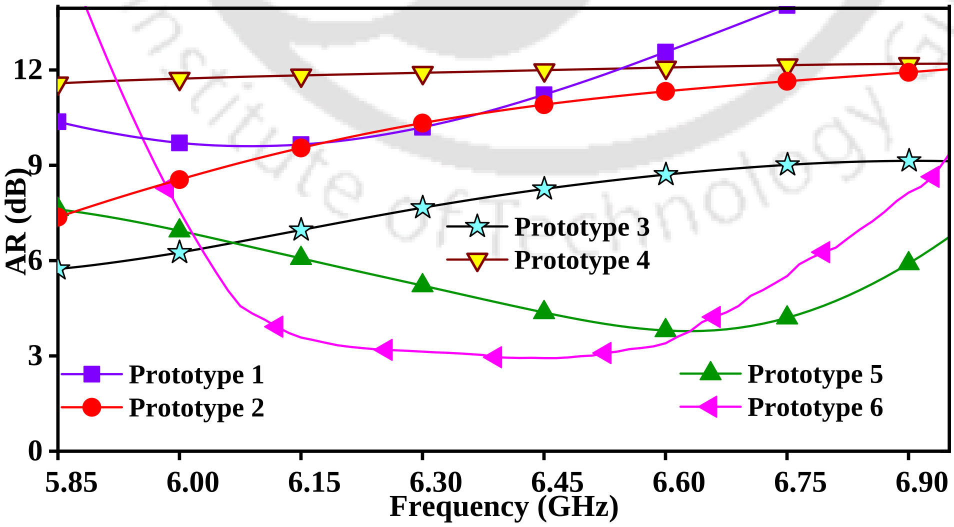

Fig. 6.5: AR of different prototypes of Fig. 6.4 versus frequency.

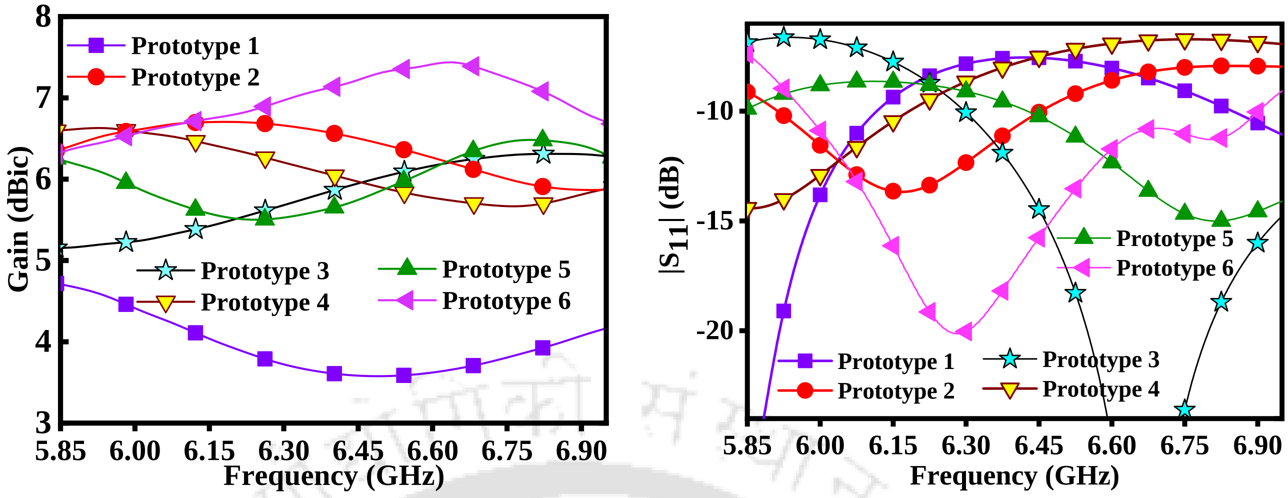

(a) (b)

Fig. 6.6: (a) Gain and (b) $|S_{11}|$ of different prototypes against frequency of Fig. 6.4.

6.4 Design of DGS

As mentioned earlier, since the DGS can be considered to act as a bandstop filter, it can be modelled as an RLC circuit. The circuit parameters C and L can be determined from following the relationships [?]:

$$C = \frac{\omega_C}{2Z_0\left(\omega_0^2 - \omega_C^2\right)} \tag{6.2}$$

$$L = \frac{1}{\omega_0^2 C} \tag{6.3}$$

where Z_0 is the characteristic impedance, ω_C is the lower cut-off angular frequency, and ω_0 is the resonant angular frequency. Substituting $Z_0 = 50\,\Omega$, $\omega_C = 2\pi \times 5.8 \times 10^9$ rad/s, and $\omega_0 = 2\pi \times 6.4 \times 10^9$ rad/s the values of the parameters are found to be $C = 1.38$ pF and $L = 0.45$ nH. The radiation rate η is given by [?]

$$\eta = \left(1 - |S_{11}|^2_{f=f_0} - |S_{21}|^2_{f=f_0}\right) \tag{6.4}$$

where $|S_{11}|^2_{f=f_0}$ and $|S_{21}|^2_{f=f_0}$ are the squares of the amplitudes of S_{11} and S_{21} at the resonant frequency which are 0.88^2 and 0.12^2 respectively. This implies $\eta = 0.21$ that satisfies the condition $0.11 \leq \eta \leq 0.24$ [?]. Furthermore, the value of R is given as [?]

$$R = \frac{2Z_0}{\eta}\left(1 - \eta + \sqrt{1 - 2\eta}\right) \tag{6.5}$$

which yields $R = 740.57\,\Omega$ that satisfies $600\,\Omega \leq R \leq 1500\,\Omega$ [?].

From these R, L, and C values, the S-parameters of the circuit shown in Fig. 6.7(b) are determined using Cadence Virtuoso. These values are then plotted against frequency for comparison with the S-parameters of the DGS bandstop filter as shown in Fig. 6.7(a) from which it is observed that the two sets of S-parameters have close agreement, thus confirming the equivalence of the two structures.

The quality factor Q of the DGS is given by [?]

$$Q = \omega_0 C R \tag{6.6}$$

such that $Q = 41.15$. Using these parameters, the fractional bandwidth (FBW) of the DGS is calculated as [?]

$$FBW = \frac{\sqrt{2 - (1 + 2GZ_0)^2}}{2GZ_0Q} \tag{6.7}$$

which gives FBW = 15.18%, where $G = \frac{1}{R}$ and $GZ_0 = 0.0675$ that satisfies the condition $GZ_0 \leq \frac{\sqrt{2}-1}{2}$ [?]. From the plot of $|S_{21}|$ in Fig. 6.7(a), it is observed that the FBW is 15.63% which agrees well with the value calculated from circuit components.

Of all the geometric parameters of the DGS unit cell given in Table 6.2, the most important one responsible for maximum port-to-port isolation is found to be W_4. The remaining parameters either cause an unwanted shift in the DGS resonant frequency, or adversely impact the antenna function. It can be observed from Fig. 6.8 that for highest inter-port isolation, the value of W_4 should be 0.40 mm. This is because $W_4 = 0.20$ mm yields better isolation at frequencies where the antenna no longer functions as a CP antenna due to high AR (> 3 dB).

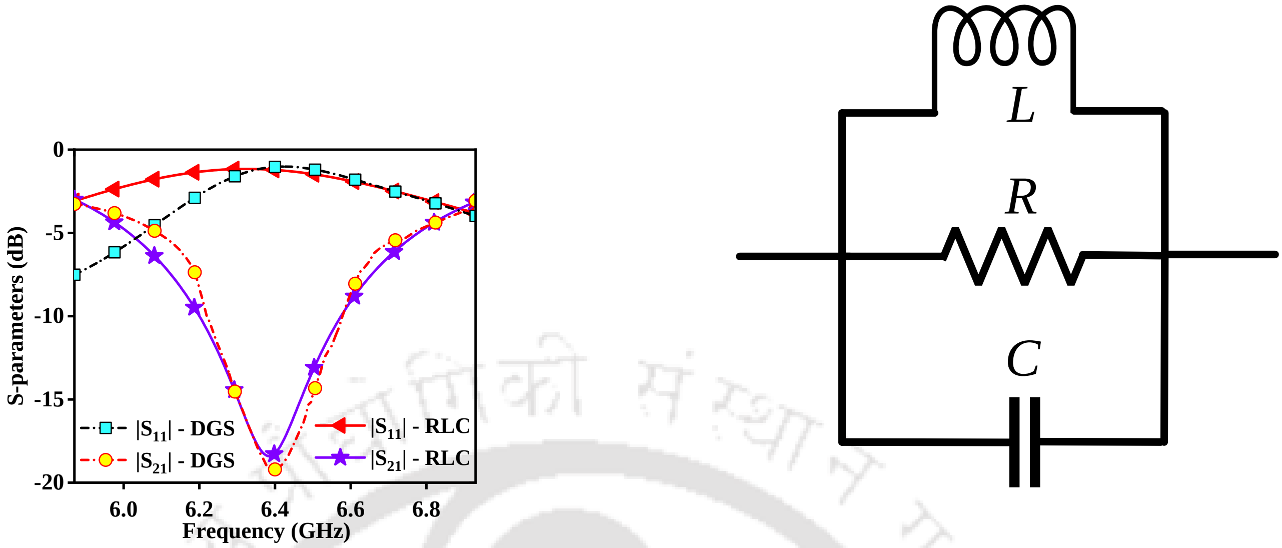

(a)

(b)

Fig. 6.7: (a) RLC-circuit equivalent of the DGS and (b) S-parameters of the DGS versus frequency

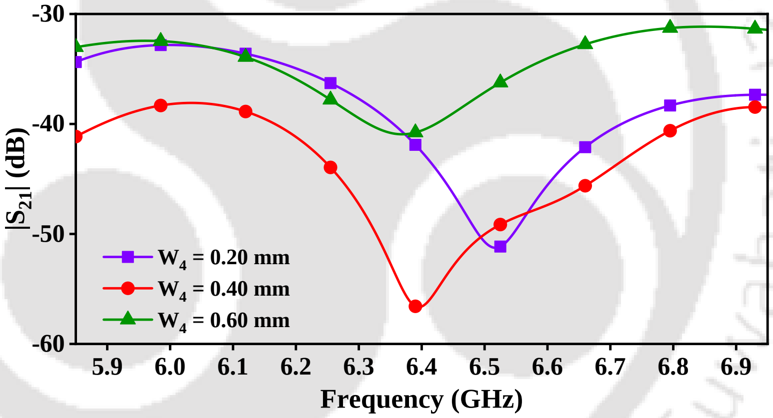

Fig. 6.8: $|S_{21}|$ versus frequency for different values of W_4 (as in Fig. 6.3(b)).

6.5 Parametric analysis

After many simulations, the parameters (of Fig. 6.2) of the selected Prototype 6 which are vital for optimum antenna performance are determined to be:

(i) slot parameters S_3 and S_5 (for best impedance bandwidth),

(ii) slot parameters S_1, S_2, S_3, and S_4 (for best AR bandwidth),

(iii) length of the truncated corner a_1 and gaps between excited and parasitic patches G_1 and G_2 (for best AR bandwidth and gain)

(iv) location of the coaxial feed on the excited patch C_p (for best impedance matching)

Table 6.3 shows the different combinations of S_3 and S_5 tested for optimum impedance bandwidth and Fig. 6.9 shows the plots of $|S_{11}|$ versus frequency for these combinations. It is obvious from the plots that the widest impedance bandwidth occurs when $S_3 = 1.80$ mm and $S_5 = 4.00$ mm (B_1) as for other combinations, the bandwidth is narrower.

Table 6.3: Combination of slot dimensions S_3 and S_5 (in mm) tested for best impedance bandwidth.

Combinations	**S_3**	**S_5**
B_1	1.80	4.00
B_2	0.80	4.00
B_3	2.80	4.00
B_4	1.80	3.30
B_5	1.80	4.70

The different combinations of S_1, S_2, S_3, and S_4 tested for the best AR bandwidth are given in Table 6.4 whereas the AR versus frequency plots for these combinations are given in Fig. 6.10. It is clear from the plots that the parameters S_2 and S_3 are vital for a lower shift of the AR bandwidth (as evident from C_1, C_2, C_5, C_6, and C_7) since any value of these parameters other than 2.30 mm and 1.80 mm respectively causes the AR bandwidth to shift to a higher band. On the other hand, the parameter S_1 controls the AR bandwidth and the largest value of the latter is obtained when $S_1 = 4.33$ mm (as in C_1). Finally, S_4 must be chosen as 4.15 mm as for other values either the AR bandwidth to a higher band (C_9) or is narrower (C_8).

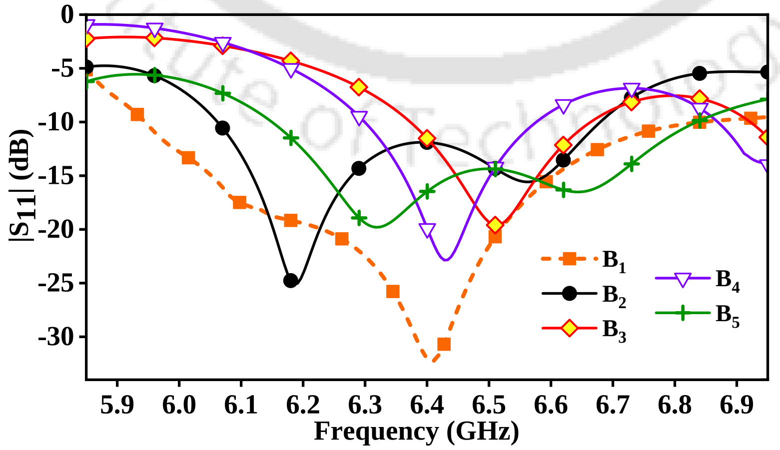

Fig. 6.9: $|S_{11}|$ versus frequency for different values of S_3 and S_5.

Table 6.4: Combination of slot dimensions S_1, S_2, S_3, and S_4 (in mm) examined for the best AR bandwidth.

Combinations	$\mathbf{S_1}$	$\mathbf{S_2}$	$\mathbf{S_3}$	$\mathbf{S_4}$
C_1	4.33	2.30	1.80	4.15
C_2	3.33	2.30	1.80	4.15
C_3	5.33	2.30	1.80	4.15
C_4	4.33	1.80	1.80	3.15
C_5	4.33	2.80	1.80	3.15
C_6	4.33	2.30	0.80	3.15
C_7	4.33	2.30	2.80	5.15
C_8	4.33	2.30	2.80	5.15
C_9	4.33	2.30	2.80	5.15

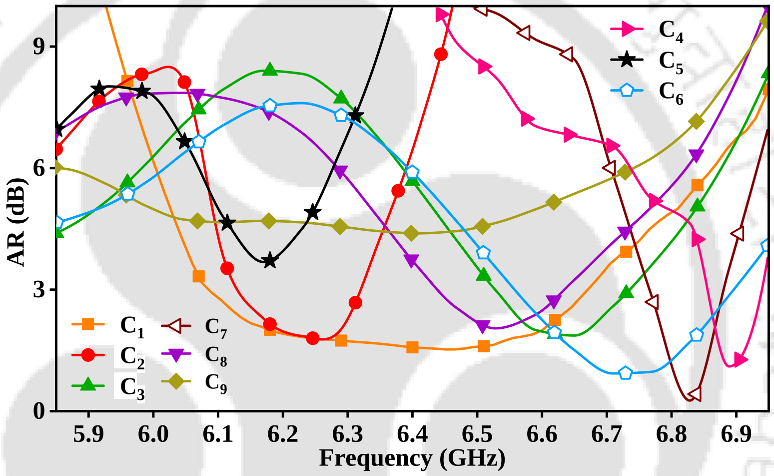

Fig. 6.10: AR with respect to frequency for different values of S_1, S_2, S_3 and S_4.

The effects of length of the truncated corner a_1 and the gap between excited patch and its neighbouring parasitic patch G_1 on the AR bandwidth is shown in Fig. 6.11(a). It is evident from the figure that the AR shifts to the a higher frequency when $a_1 = 4.70$ mm compared to when $a_1 = 2.70$ mm or $a_1 = 3.70$ mm. This can be explained from (6.1) which indicates that a higher value of S_T due to a greater a_1 translates to a larger f'_{AR}. Moreover, the AR bandwidth shifts to the lower band when $a_1 = 2.70$ mm though the AR value is quite high (> 2.5 dB). For this reason, a_1 is chosen as 3.70 mm that yields the widest AR bandwidth. Similarly, choosing $G_1 = 0.30$ mm improves the AR bandwidth significantly, in contrast to when $G_1 = 0.15$ mm or $G_1 = 0.45$ mm.

Fig. 6.11(b) shows the plots of gain at different values of G_1 and G_2 versus frequency. It is obvious that for $G_1 = 0.15$ mm or 0.45 mm the gain is significantly lower than when $G_1 = 0.30$

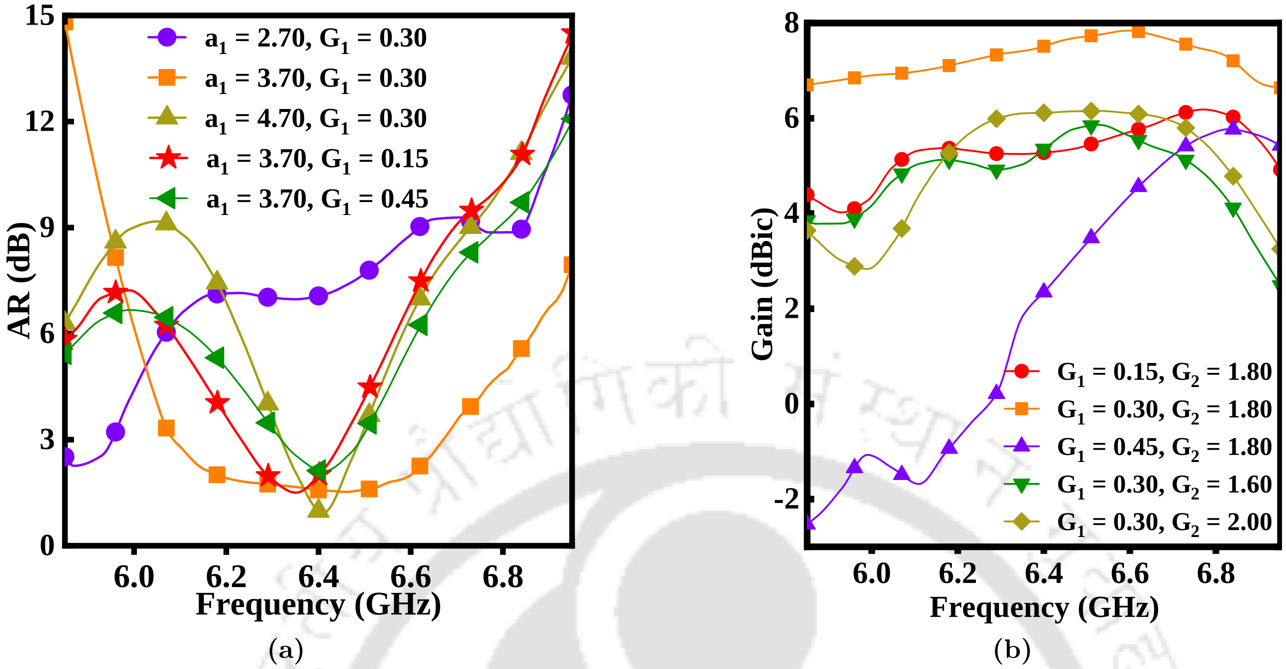

(a) (b)

Fig. 6.11: (a) AR for different values of a_1 and G_1 and (b) gain for different values of G_1 and G_2 versus frequency (all dimensions are in mm)

mm. Therefore, G_1 is chosen as 0.30 mm. Similarly, choosing $G_2 = 1.80$ mm improves the gain by about 1.5 to 2 dBic as compared to when $G_2 = 1.60$ mm or $G_2 = 2.00$ mm.

The location of the coaxial connector probe on the excited patch is important for impedance matching, as seen in Fig. 6.12 from which it can be observed that the best impedance matching is obtained when $C_p = 3.90$ mm as compared to $C_p = 3.60$ mm or $C_p = 4.20$ mm which yield lower impedance bandwidths and also shift the resonant frequencies to a higher value.

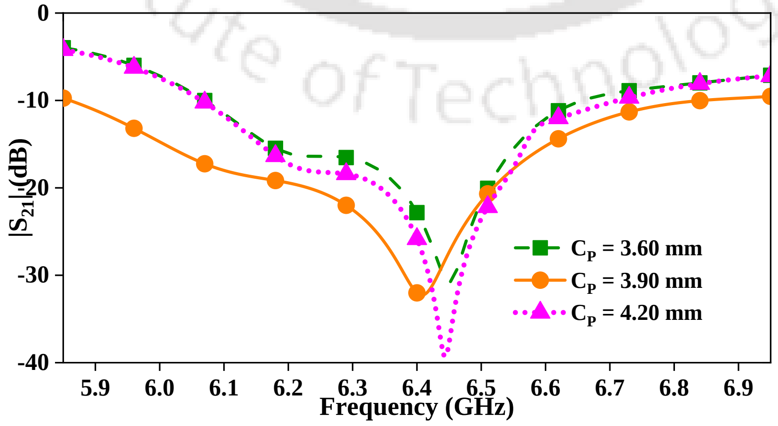

Fig. 6.12: $|S_{11}|$ versus frequency for different values of C_p.

The aperture, through which the coaxial probe is inserted for exciting the antenna, also plays an important role in impedance matching as evident from the plots in Fig. 6.13. It is obvious that a lower radius causes the resonant frequency band to shift to a higher range whereas a higher radius degrades both the impedance matching and the resonance bandwidth. Therefore, an optimum radius of 1.475 mm is chosen for the design.

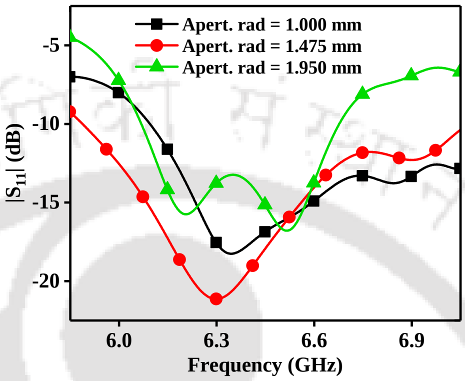

Fig. 6.13: $|S_{11}|$ as function of frequency for different aperture-radii.

6.6 Mechanism of CP

The CP action can be understood by analyzing the surface currents on the excited patch. Fig. 6.14 shows the surface current distribution on the excited patch $\mathrm{EP_T}$ at four different phase angles ($\omega t = 0°$, $90°$, $180°$, and $270°$). Using the method of composite vector analysis [68], the resultant current directions (shown in red arrows) denoted by $\boldsymbol{R}$ is determined for each of these phase angles. From the rotation of the vector $\boldsymbol{R}$ in the anti-clockwise direction with respect to the phase-angle, it can be concluded that RHCP is generated.

Moreover, all the patches are electromagnetically coupled to each other in such a way that, the currents induced at the adjacent edges of any of the parasitic patches, are out of phase by 90°. This phenomenon which is depicted in Fig. 6.15, produces the CP mode and the net AR bandwidth is augmented.

6.7 Results and discussions

The plots of simulated and measured values of S-parameters of the designed antenna under different conditions are shown in Fig. 6.16.

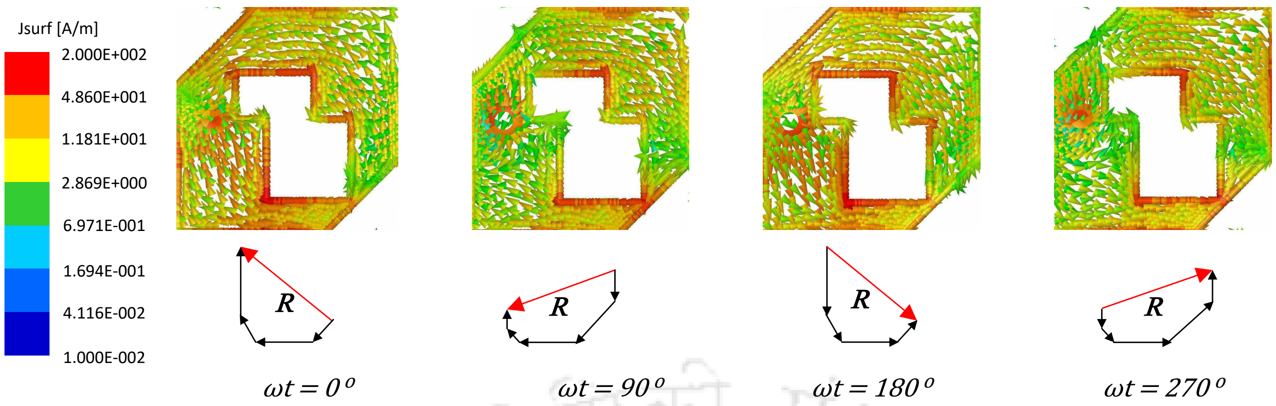

Fig. 6.14: Surface current distribution on $\mathrm{EP_T}$ patch at different phase angles (a) $\omega t = 0°$ (b) $\omega t = 90°$ (c) $\omega t = 180°$ and (d) $\omega t = 270°$ at 6.40 GHz

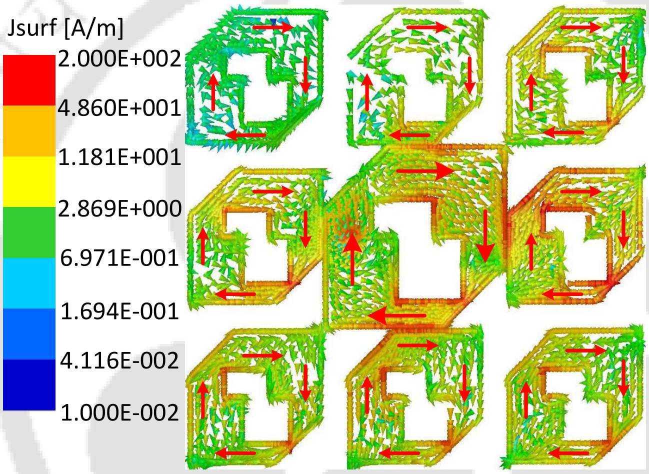

Fig. 6.15: Surface current directions in the patches of the $\mathrm{T_X}$ group at 6.40 GHz

It is seen that the antenna has a wide -10 dB impedance bandwidth that ranges from 5.95 GHz to 6.85 GHz, which is 14.06% of the centre frequency $f_0 = 6.40$ GHz. It may also be observed that the port-to-port isolation varies from 37 to 57 dB within this band. This implies that the DGS substantially aids in port decoupling by imparting an additional 12 to 18 dB to the interport isolation in contrast to the same antenna without the DGS. This effect is further illustrated in Fig. 6.17, which shows that because of the presence of the DGS, the current density on the $\mathrm{R_X}$ patches are considerably lower than when there is no DGS.

By comparing the plots of $|S_{11}|$ in Fig. 6.6(b) and 6.16, it is also noted that the presence of the DGS results in a better impedance matching, at the cost of a slight shift of the resonant frequency to a higher value.

For the purpose of brevity, only the Port 1 was excited while measuring the AR and gain,

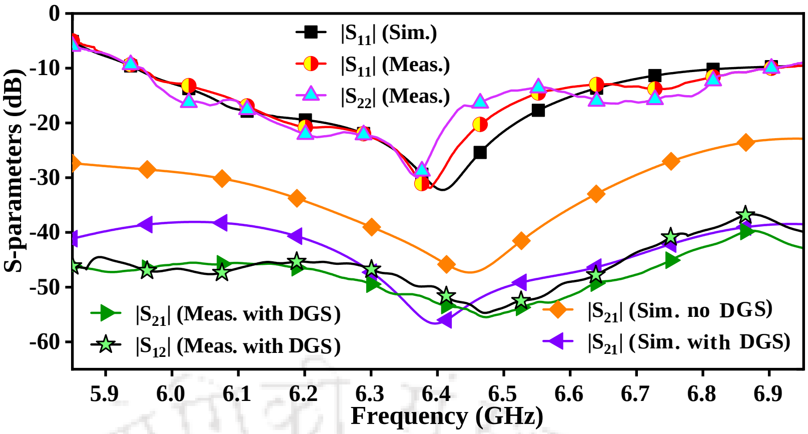

Fig. 6.16: Variation of simulated and measured S-parameters with frequency.

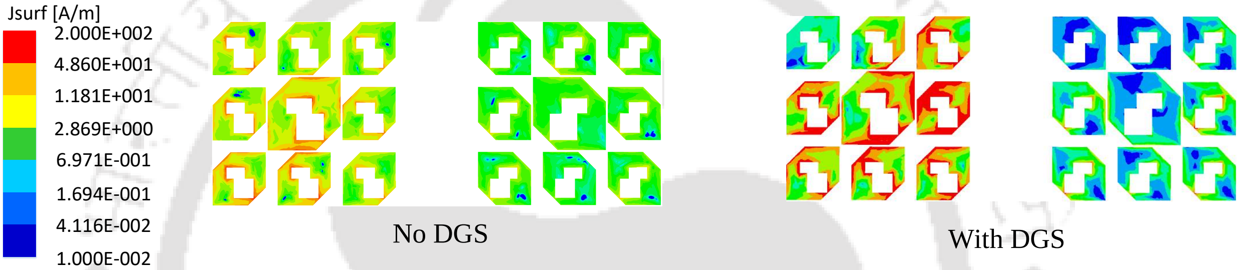

Fig. 6.17: Surface current densities on the antenna under different conditions at 6.40 GHz.

exploiting the symmetric nature of the antenna about its two ports. The AR is measured using the swept-frequency technique [?], and the plot of the same is shown in Fig. 6.18. It is observed that the 3-dB AR bandwidth lies between 6.06 GHz and 6.66 GHz centered at 6.24 GHz and the minimum value of AR occurs at 6.46 GHz. This is quite close to the calculated value obtained using (6.1) with a minor deviation of 3.15%. In this region, the interport isolation ranges from 45 to 55 dB. Thus, high isolation is achieved between the ports that considerably simplifies the transceiver design by lowering the SIC requirement as established in [?, ?].

Assuming noise-figure (NF) to be 17 dB and reference noise power to be −174 dBm, the received noise power $\mathrm{P_N}$ is given by [?]

$$\mathrm{P_N} = -174\,\mathrm{dBm} + 10\log_{10}(\mathrm{BW_{AR}}) + \mathrm{NF} \tag{6.8}$$

Since the AR bandwidth ($\mathrm{BW_{AR}}$) is 600 MHz, the value of $\mathrm{P_N}$ is calculated to be −69.22 dBm. Assuming 20 dBm $\mathrm{T_X}$ power [?], the required SIC is 89.22 dBm. However, as discussed

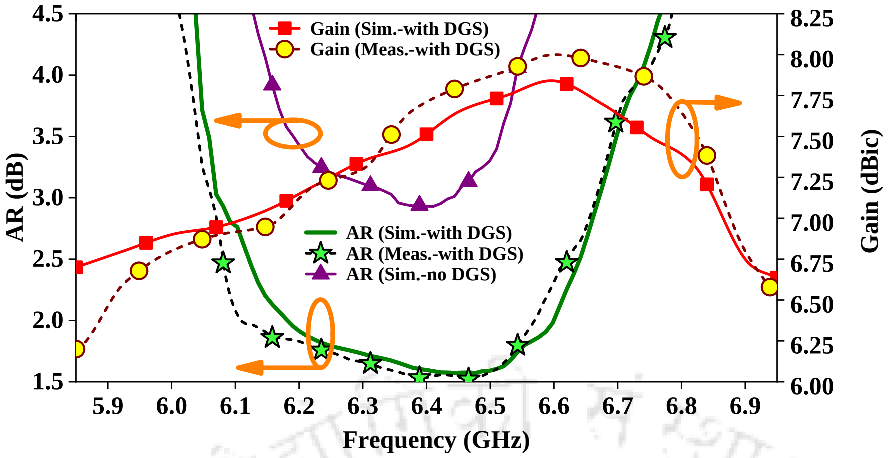

Fig. 6.18: Simulated and measured AR and gain as functions of frequency

above, since the port-to-port isolation within the AR bandwidth lies between 45 and 55 dB, only 34.22 to 44.22 dB of the total isolation is required to be contributed by the external circuitry.

The gain of the antenna is seen to be varying from 6.8 dBic to 7.9 dBic within the AR bandwidth as in Fig. 6.18. The high gain can be explained by observing the surface current vectors in Fig. 6.15, which shows that the directions of the vectors are same as in $\mathrm{EP_T}$ and the parasitic patches surrounding it.

The normalized radiation patterns in two different planes, i.e. the *xoz* plane and the *yoz* plane are shown in Fig. 6.19. It is observed from the figures that the cross-polarization discrimination (XPD), i.e. the difference in power levels between the RHCP and LHCP modes in the direction of main-beam is around 20 dB. This agrees with the equation given in [?] which is

$$\mathrm{P_{dB}} = 20\log_{10}\left(\frac{\mathrm{ar}+1}{\mathrm{ar}-1}\right) \tag{6.9}$$

Here, $\mathrm{P_{dB}}$ is the XPD in dB and ar is the numeric value of AR. At 6.40 GHz, ar = 1.2, which yields 20 dB XPD that agrees with the radiation pattern.

The normalized radiation patterns of the antenna without and with the DGS are shown in Fig. 6.20. It is obvious from these plots that the DGS has a significant role in improving the XPD in both the planes in the direction of main-lobe by about 5 dB. This phenomenon in turn, widens the AR bandwidth, that can be observed by comparing the values of this parameter

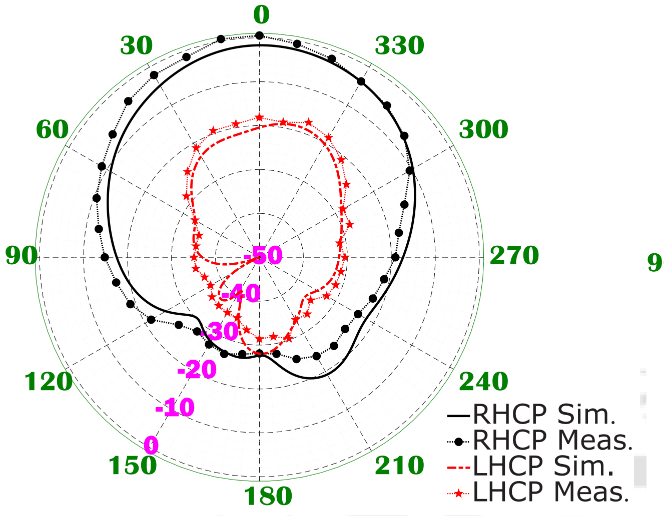

(a) (b)

Fig. 6.19: Radiation patterns in two different planes at 6.40 GHz (a) *xoz* plane and (b) *yoz* plane

without and with DGS from the AR plots given in Fig. 6.18.

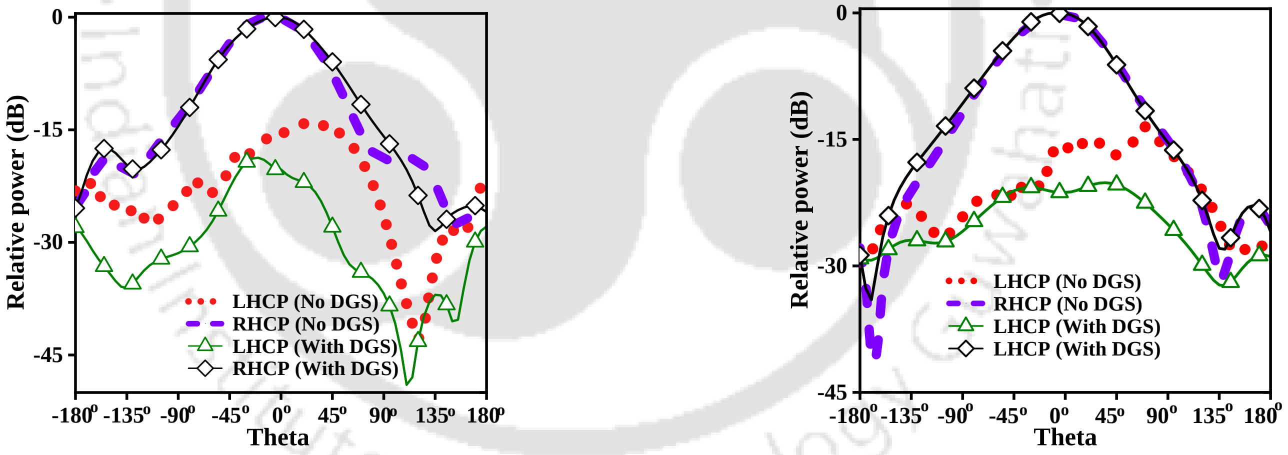

(a) (b)

Fig. 6.20: Radiation patterns in two different planes at 6.40 GHz (a) *xoz* plane and (b) *yoz* plane

The current vector-field distribution around the right central patch is shown in Fig. 6.21a at 6.45 GHz for two different types of ground planes - the one without the DGS and the one incorporating the DGS. In the former case, considerable orthogonal current-vectors are present a compared to the later which contributes to a high cross-polarization that deteriorates the AR bandwidth. On the same note, observing the scalar E-fields below this group of patches (as seen from Fig. 6.21b), it is clear that the contours of the E-fields are more tightly bound to the contour of the central patch in presence of the DGS than when without. Therefore, it can be concluded that the DGS has a significant role in reducing the unwanted cross-polar component thereby boosting the AR bandwidth [?].

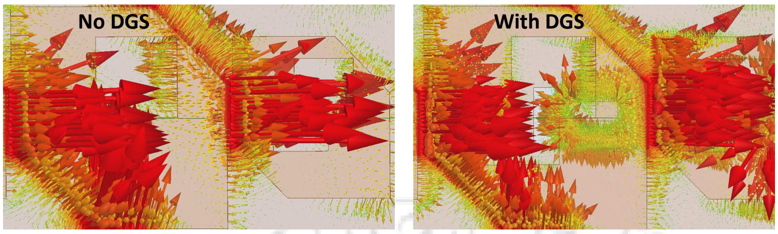

(a)

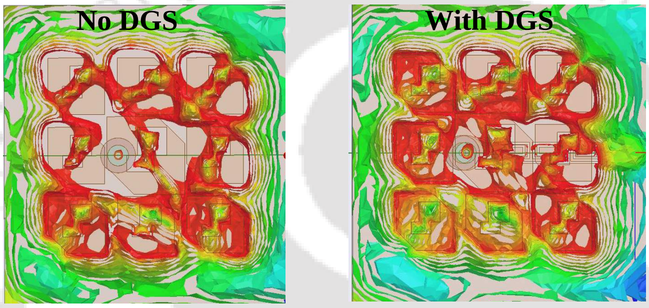

(b)

Fig. 6.21: Radiation patterns in two different planes at 6.40 GHz (a) *xoz* plane and (b) *yoz* plane

The table of comparison showing the distinctions between the designed antenna and other recently reported DCP antennas is presented in Table 6.5. It is obvious that the antenna presented in this work, has the best interport isolation and comparable or superior performances in terms of impedance bandwidth, AR bandwidth, and XPD with the highest among those in state-of-the-art designs with the exception of [73]. The latter, however, is an antenna array of larger overall size as opposed to this antenna. Moreover, using (6.8) and assuming the similar conditions discussed therein, the antenna presented here has the lowest SIC requirement, which indicates a simpler transceiver design that will be required by this antenna as compared to the rest. The photographs of the fabricated antenna are shown in Fig. 6.22.

The plots of ECC with respect to frequency for two the antenna with with the DGS, are given in Figs. 6.23a and 6.23b. It is observed from the plot that with the DGS, the ports are adequately decoupled such that the ECC lies below 0.0050 within the AR bandwidth which is very small, indicating that the antenna beams from its two ports are almost uncorrelated.

(a) (b)

Fig. 6.22: Photograph of the fabricated antenna showing the (a) excited patches surrounded by the parasitic patches and (b) ground plane with the DGS between antenna ports

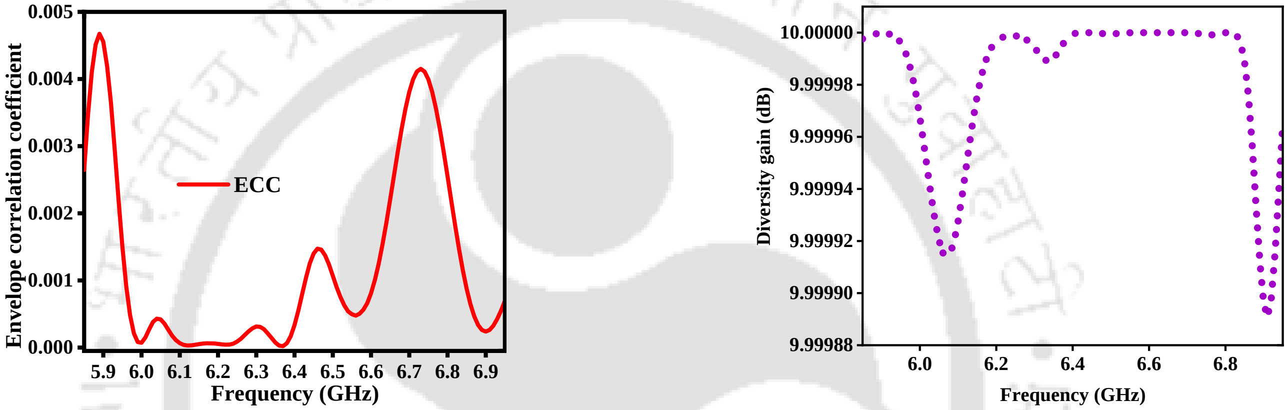

(a) (b)

Fig. 6.23: ECC and DG with respect to frequency

6.8 Design guidelines

The flowchart in Fig. 6.24 gives the overview of the major design stages which are explained below:

(i) Stage 1 - The initial dimensions of the central patches (i.e. side-length $a_1 + d_1$ as in Fig. 6.2b) are chosen for resonance at the desired frequency using the equations given in [?]. This is followed by choosing the length of the truncated corners using (6.1) such that the minimum AR lies in the vicinity of the resonant frequency. This results in Prototype 1 of Fig. 6.4.

(ii) Stage 2 - In this stage, eight parasitic patches (each of side length $a_2 + d_2$ as in Fig. 6.2b) are provided around each of the excited patches so as to augment the overall antenna performance in terms of gain, impedance bandwidth and AR bandwidth. To achieve these goals, the length of the truncated corners of the parasitic patches a_2 (as in Fig. 6.2b) and the inter-patch gaps G_1 and G_2 (as in Figs. 6.2b and 6.2a respectively) are selected for the best AR bandwidth and gain so that Prototypes 2 and 3 are obtained. Subsequently, the slot dimension combinations $[S_1\ S_2\ S_3\ S_4]$ and $[S_3\ S_5]$ (as in Fig. 6.2b) are tuned for the best AR bandwidth and impedance bandwidth respectively yielding Prototypes 4 and 4A. To further lower the AR, slots are provided in rectangular parasitic patches resulting in Prototype 5. Finally Prototype 6 is designed, combining the features of all the preceding ones and the probe-location C_p (as in Fig. 6.2b) is determined for the best impedance matching.

(iii) Stage 3 - The DGS is designed in this stage so that it helps in port-decoupling and cross-polarisation reduction. The latter lowers the AR and improves the AR bandwidth. Furthermore, the RLC equivalent circuit model of the DGS is derived using (6.2)-(6.5) and verified using Cadence Virtuoso.

(iv) Stage 4 - The selected prototype (i.e. Prototype 6 with the DGS on its ground plane) is fabricated and is tested for experimental validation of the simulated results. The parameters measured are - S-parameters, AR and peak gain which are then compared with the simulated data. Also, the antenna is assessed for utility in MIMO applications by computing envelope correlation coefficient (ECC) and channel capacity loss (CCL) from the simulated and measured data.

6.9 Summary

This chapter proposes a DCP antenna that is based on a microstrip patches. The antenna contains two patch groups, each for transmission and reception. Only the central patch with truncated opposite corners is probe-fed in one such group, while the surrounding ones serve as parasitic patches for bandwidth and gain enhancement. To boost port-to-port isolation as well as the AR bandwidth, a DGS consisting of 4 units of square spiral resonators is utilized. This research demonstrates the band-reject properties of the DGS by extracting and checking its S-parameters with its RLC-equivalent circuit. Also, by reducing the orthogonal current elements in a patch, the DGS helps in improving the XPD. These characteristics suggest its suitability

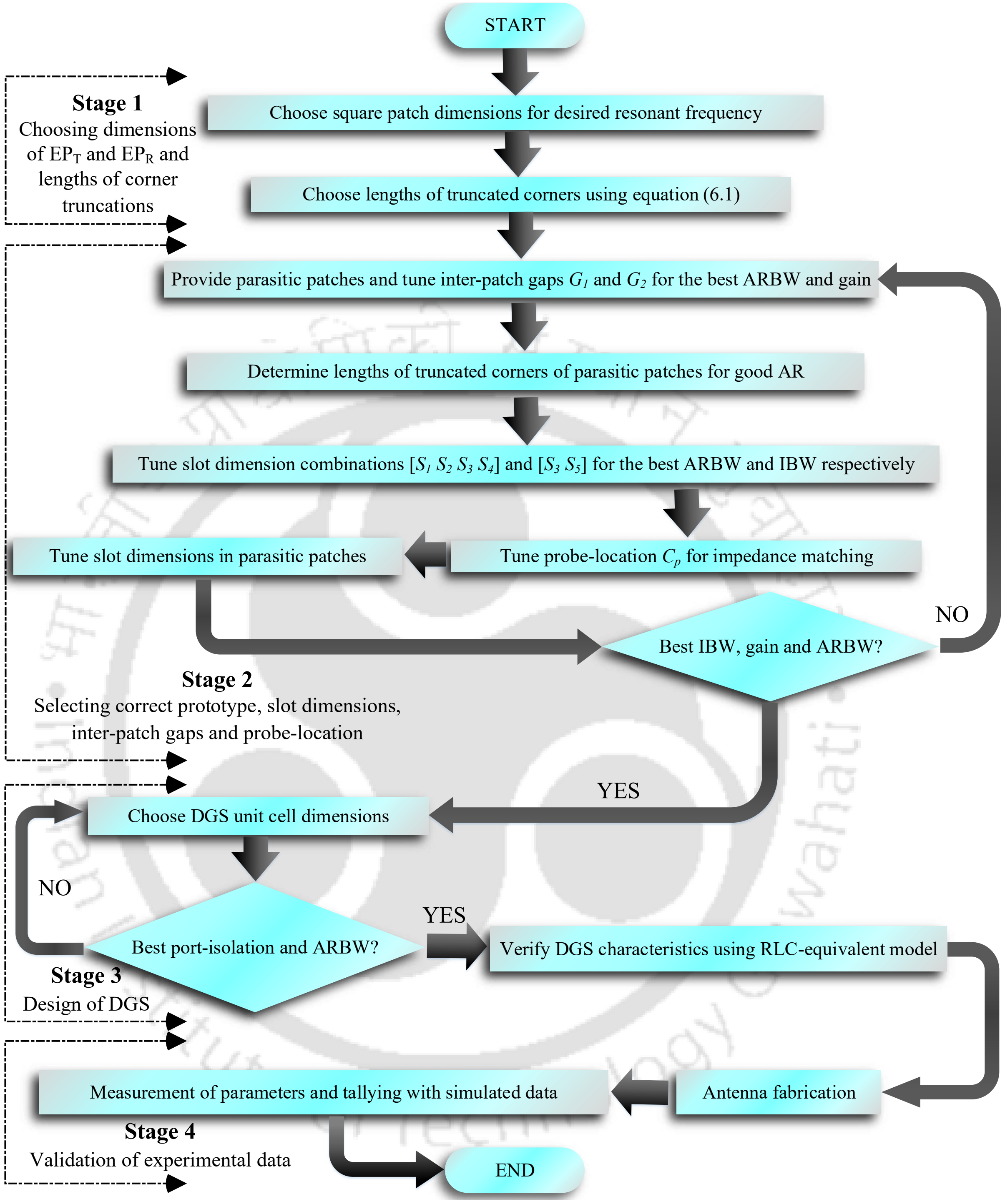

Fig. 6.24: Flowchart showing the design stages (IBW: -10 dB impedance bandwidth, ARBW: 3 dB AR bandwidth)

for polarimetry, satellite communications and polarization diversity applications. Furthermore, since the antenna has highly decoupled ports along with a large AR bandwidth, the usage of this antenna in a radio transceiver will allow the use of a simpler transceiver.

Table 6.5: Comparison of the performance of the proposed antenna with other recently reported antennas: IBW - -10 dB impedance bandwidth, ARBW - 3 dB AR bandwidth, $\mathrm{I_i}$ - Interport isolation within IBW, SIC Req. - SIC Requirement of $\mathrm{R_X}$, († 2.5 dB ARBW, ‡ - circular shape).

Ref.	**IBW (%)**	**ARBW (%)**	**$\mathrm{I_i}$ (dB)**	**XPD (dB)**	**Peak gain (dBic)**	**SIC Req. (dB)**	**Antenna dimensions**
[?]	10.6	10.6	10 to 36	30	2.4	83	$1.38\lambda_0 \times 0.36\lambda_0 \times 0.31\lambda_0$
[?]	12.2	4.80	5 to 20	18	6.8 and 7.4	90	$0.50\lambda_0 \times 0.50\lambda_0 \times 0.057\lambda_0$
[?]	3.0	$2.3^{\dagger}$	7.5 to 20	15	6.5	91.7	$0.70\lambda_0 \times 0.70\lambda_0 \times 0.69\lambda_0$
[?]	6.7	3.8	23 to 30	21	9.3	68	$1.75\lambda_0^2 \times 0.037\lambda_0$ ‡
[73]	5.5	5.5	15 to 25	20	13.5	74.6	$2.10\lambda_0 \times 2.10\lambda_0 \times 0.026\lambda_0$
[?]	4.7 and 7.3	1.1 and 3.2	24 to 40	15	6.0 and 8.0	70.7	$0.73\lambda_0 \times 0.73\lambda_0 \times 0.044\lambda_0$
This work	14.06	9.43	39 to 57	20	7.9	44.22	$1.58\lambda_0 \times 0.83\lambda_0 \times 0.031\lambda_0$

7

Dual circularly polarized travelling-wave antenna array

A series-fed DCP planar slot antenna array is presented in this chapter. The radiating slots of the antenna are located on its ground plane and are excited by means of a ring-shaped microstrip line consisting of rectangular sections at regular intervals. A metallic reflector lies underneath the feed network separated by an air-layer to augment the gain of the antenna. The parameters of a fabricated prototype are measured for validation, based upon which the antenna is found to have an impedance bandwidth of 1189 MHz which is 18.46% of the centre frequency $f_0 = 6.45$ *GHz. Also, the AR bandwidth is 880 MHz centred at* $f_{AR} = 6.54$ *GHz. The inter-port isolation ranges from 25 to 45 dB and the gain ranges from 8.2 to 9.5 dBic within the AR band. The antenna exhibits beam scanning capability and is therefore suitable for various applications like satellite communication, radiometry and polarimetry.*

7.1 Introduction

DCP travelling wave antennas were introduced in Chapter 3 and a few examples from the contemporary literature were discussed. In this chapter we delve deeper into such type of antennas to understand the mechanism behind their functioning. The following section 7.2 therefore develops a theoretical background for DCP travelling-wave antennas. Section 7.3 presents a travelling-wave slot antenna intended for satellite communications and polarimetry designed by the author.

7.2 Theoretical background of DCP travelling wave antennas

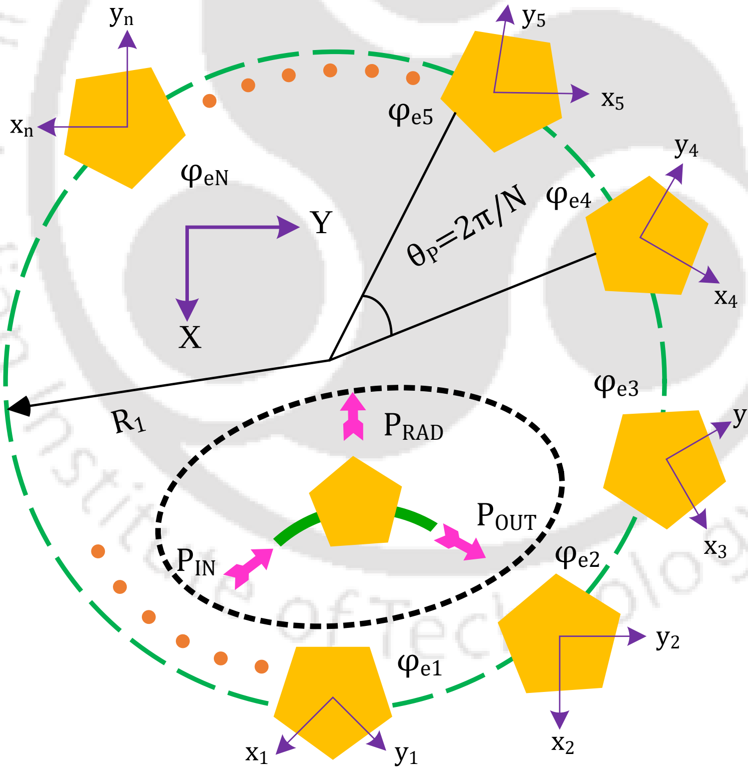

Fig. 7.1: Geometry of N element circular array of radius R_1 [75]

A circular array of N patches spaced at equal distances apart is considered as shown in Fig. 7.1 which has a feed-line of electrical length $m\lambda_g$. The radius of the circle is R_1 and the angular separation between each of the elements is $\theta_p = \frac{2\pi}{N}$. The schematic of a radiating single element model is shown in inset within the dotted elliptical border. The power radiated by each such element can therefore be written as [?]

$$P_{RAD} \propto 1 - \left|\tilde{S}_{21}\right|^2 \tag{7.1}$$

where $\left|\tilde{S}_{21}\right|$ is determined from the ratio of P_{OUT} to P_{IN}. Therefore, the power coupling coefficient γ of this element is

$$\gamma = 1 - \left|\tilde{S}_{21}\right|^2 \tag{7.2}$$

Suppose the total power input to the array is 1 W. Then, the power radiated by element 1 must be

$$p_1 = \gamma \tag{7.3}$$

In the similar way, if p_2, p_3, …, p_n denote the powers radiated by elements 2, 3, …, n the following relations are valid

$$p_2 = (1 - p_1)\,\gamma = (1 - \gamma)\,\gamma \tag{7.4}$$

$$p_3 = (1 - p_2 - p_1)\,\gamma = (1 - \gamma)^2\,\gamma \tag{7.5}$$

$$\vdots \tag{7.6}$$

$$p_n = (1 - \gamma)^{n-1}\,\gamma \tag{7.7}$$

These terms i.e. p_1, p_2, p_3, …, p_n are in geometric progression with a common ratio $(1 - \gamma)$ whose sum A_T represents the total radiated power by the circular array. Thus one may write

$$A_T = \sum_{n=1}^{N} p_n = \frac{\gamma\left(1 - (1 - \gamma)^N\right)}{1 - (1 - \gamma)} = 1 - (1 - \gamma)^N \tag{7.8}$$

This equation, as will be seen later, is of great importance as it gives a hint on the optimum number of elements required in such an array for a given $\left|\tilde{S}_{21}\right|$.

Suppose φ_1, φ_2, φ_3, …, φ_n, …, φ_N represent the phase angles of excitation of patches numbered 1, 2, 3, …, n, …, N as shown in Fig. 7.1. Without any loss of generality, we assume $\varphi_1 = 0°$. The phase angle φ_n corresponding to the element n must satisfy the relationship given below

$$\varphi_n = -2\pi \frac{n-1}{N} m\lambda_g \tag{7.9}$$

where $1 < n < N$. An examination of Fig. 7.1 suggests that the coordinates of patch n i.e. (x_n, y_n) is tilted at an angle $(n-1)\,\theta_p$ with respect to that of patch 1 i.e (x_1, y_1). In such a case, the equations for coordinate transformation can be applied which is

$$\begin{bmatrix} x_n \\ y_n \end{bmatrix} = \begin{bmatrix} \cos\left(\theta_p\left(n-1\right)\right) & \sin\left(\theta_p\left(n-1\right)\right) \\ -\sin\left(\theta_p\left(n-1\right)\right) & \cos\left(\theta_p\left(n-1\right)\right) \end{bmatrix} \begin{bmatrix} x_1 \\ y_1 \end{bmatrix} \tag{7.10}$$

or

$$(x_n, y_n) = (x_1, y_1)\exp\left(j\left(n-1\right)\theta_p\right) \tag{7.11}$$

Since a linear polarization is the superposition of two circular polarizations, for the n^{th} element, we may write

$$\vec{E}\Big|_n = \left|\vec{E}_{RHCP}\right|_n (x_n\hat{a}_x - jy_n\hat{a}_y) + \left|\vec{E}_{LHCP}\right|_n (x_n\hat{a}_x + jy_n\hat{a}_y) \tag{7.12}$$

The AR of the n^{th} radiating element may be written as

$$AR_n = 20\log_{10}\frac{\left|\vec{E}_{RHCP}\right|_n + \left|\vec{E}_{LHCP}\right|_n}{\left|\vec{E}_{RHCP}\right|_n - \left|\vec{E}_{LHCP}\right|_n} \tag{7.13}$$

Suppose k is the ratio of the magnitude of RHCP component to that of the LHCP component of E-field. Then k may be written as

$$k = \frac{\left|\vec{E}_{RHCP}\right|_n}{\left|\vec{E}_{LHCP}\right|_n} = \frac{10^{AR_n/20}+1}{10^{AR_n/20}-1} \tag{7.14}$$

or

$$\left|\vec{E}_{RHCP}\right|_n = k\left|\vec{E}_{LHCP}\right|_n \tag{7.15}$$

It is noted that

$$\left|\vec{E}_{RHCP}\right|_n^2 + \left|\vec{E}_{LHCP}\right|_n^2 = 1 \tag{7.16}$$

and

$$|E| \propto \sqrt{p_n} \tag{7.17}$$

or

$$|E| = \chi\sqrt{p_n} \tag{7.18}$$

where χ is a normalizing factor. Hence using (7.15), (7.16) and (7.18) one may write

$$\left|\vec{E}_{RHCP}\right|_n = \chi\sqrt{\frac{k^2}{k^2+1}p_n} \tag{7.19}$$

and

$$\left|\vec{E}_{LHCP}\right|_n = \chi\sqrt{\frac{1}{k^2+1}p_n} \tag{7.20}$$

Thus the RHCP E-field of the entire array can be expressed as

$$
\begin{aligned}
\left|\vec{E}_{RHCP}\right|_T &= \sum_{n=1}^{N}\left|\vec{E}_{RHCP}\right|_n \left(x_n\hat{a_x} - jy_n\hat{a}_y\right)\exp\left(j\varphi_n\right)\\
&= \sum_{n=1}^{N}\left|\vec{E}_{RHCP}\right|_n \left(x_1\hat{a_x} - jy_1\hat{a}_y\right)\exp\left(j\left(n-1\right)\theta_p\right)\exp\left(j\varphi_n\right)\\
&= \sum_{n=1}^{N}\chi\sqrt{\frac{k^2}{k^2+1}p_n}\left(x_1\hat{a_x} - jy_1\hat{a}_y\right)\exp\left(j\left(n-1\right)\theta_p\right)\exp\left(j\varphi_n\right)\\
&= \sum_{n=1}^{N}\chi\sqrt{\frac{k^2}{k^2+1}\left(1-\gamma\right)^{n-1}}\gamma\left(x_1\hat{a_x} - jy_1\hat{a}_y\right)\exp\left(j\left(n-1\right)\theta_p\right)\exp\left(j\varphi_n\right)\\
&= \chi\left(x_1\hat{a_x} - jy_1\hat{a}_y\right)\sqrt{\frac{k^2}{k^2+1}\gamma}\sum_{n=1}^{N}\left(1-\gamma\right)^{\frac{n-1}{2}}\exp\left(j\left(n-1\right)\frac{2\pi}{N}\right)\exp\left(-j2\pi\frac{n-1}{N}m\lambda_g\right)
\end{aligned}
\tag{7.21}
$$

Therefore, summing the geometric series, one obtains

$$
\left|\vec{E}_{RHCP}\right|_T = \chi\left(x_1\hat{a_x} - jy_1\hat{a}_y\right)\sqrt{\frac{k^2}{k^2+1}}\gamma\frac{1-\left(1-\gamma\right)^{N/2}\exp\left(j2\pi\left(1-m\lambda_g\right)\right)}{1-\left(1-\gamma\right)^{\frac{1}{2}}\exp\left(j2\pi\frac{\left(1-m\lambda_g\right)}{N}\right)}
\tag{7.22}
$$

Proceeding in the similar way as above the expression for $\left|\vec{E}_{LHCP}\right|_T$ is obtained as given below

$$
\left|\vec{E}_{LHCP}\right|_T = \sum_{n=1}^{N}\left|\vec{E}_{LHCP}\right|_n \left(x_n\hat{a_x} + jy_n\hat{a}_y\right)\exp\left(j\varphi_n\right)
\tag{7.23}
$$

$$
=\chi\left(x_1\hat{a_x} + jy_1\hat{a}_y\right)\sqrt{\frac{1}{k^2+1}}\gamma\frac{1-\left(1-\gamma\right)^{N/2}\exp\left(-j2\pi\left(1+m\lambda_g\right)\right)}{1-\left(1-\gamma\right)^{\frac{1}{2}}\exp\left(-j2\pi\frac{\left(1+m\lambda_g\right)}{N}\right)}
\tag{7.24}
$$

The overall AR of the array (AR_A) is written as

$$
AR_A = 20\log_{10}\frac{\left|\vec{E}_{RHCP}\right|_T + \left|\vec{E}_{LHCP}\right|_T}{\left|\left|\vec{E}_{RHCP}\right|_T - \left|\vec{E}_{LHCP}\right|_T\right|}
\tag{7.25}
$$

Therefore using (7.14), (7.22), (7.24) and (7.25) the expression for AR_A is reduced to the following simplified form

$$AR_A = 20\log_{10} \frac{\left|\frac{10^{AR_n/20}+1}{10^{AR_n/20}-1}\right| \left|\frac{1-(1-\gamma)^{N/2}\exp(j2\pi(1-m\lambda_g))}{1-(1-\gamma)^{\frac{1}{2}}\exp\left(j2\pi\frac{(1-m\lambda_g)}{N}\right)}\right| + \left|\frac{1-(1-\gamma)^{N/2}\exp(-j2\pi(1+m\lambda_g))}{1-(1-\gamma)^{\frac{1}{2}}\exp\left(-j2\pi\frac{(1+m\lambda_g)}{N}\right)}\right|}{\left|\left|\frac{10^{AR_n/20}+1}{10^{AR_n/20}-1}\right| \left|\frac{1-(1-\gamma)^{N/2}\exp(j2\pi(1-m\lambda_g))}{1-(1-\gamma)^{\frac{1}{2}}\exp\left(j2\pi\frac{(1-m\lambda_g)}{N}\right)}\right| - \left|\frac{1-(1-\gamma)^{N/2}\exp(-j2\pi(1+m\lambda_g))}{1-(1-\gamma)^{\frac{1}{2}}\exp\left(-j2\pi\frac{(1+m\lambda_g)}{N}\right)}\right|\right|} \tag{7.26}$$

From the analysis above, the following conclusions are drawn

(i) AR_A increases initially with AR_n and then becomes stable if the latter is too high i.e. the individual elements are elliptically polarized [75]

(ii) γ determines the coupling coefficient in this type of arrays that is in turn dependent on transmission coefficient $|S_{21}|$. For instance, a high value of γ will cause most of the incident power to be radiated off by the first few elements, leading to an undesirably high AR_A [75].

(iii) According to (7.8), the total power radiated A_T is also dependent on a converging geometric series with exponent N. This implies initially A_T increases with N and then becomes stable. The same phenomenon is observed on the nature of AR_A.

(iv) When the antenna radiates RHCP waves, the total phase-shift by a radiating element is given by $Im\left(\exp\left(j\left(n-1\right)\left(1-m\lambda_g\right)\frac{2\pi}{N}\right)\right)$. This means when $m\lambda_g = 1$, the net-phase shift of an element is 0. In such a condition, all elements radiate in-phase ensuring the field strength of this polarization sense is maximum. Conversely, for the LHCP mode since the total phase-shift is $\exp\left(-j\frac{2\pi}{N}\left(1+m\lambda_g\right)\left(n-1\right)\right)$, with $m\lambda_g = 1$ there is a net phase-delay. For every element, this phase-delay adds up leading to the overall reduction in field strength of LHCP wave. This is the main reason why, if carefully designed, these type of DCP antennas have very high port-to-port isolation.

(v) The radius R_1 of the array affects the parameter $m\lambda_g$ which in turn influences AR_A.

7.2.1 Variation of AR_A with respect to different parameters

We now plot the parameter AR_A of (7.26) in this subsection with respect to different terms on the right-hand-side of this equation. This discussion will help validate the above conclusions drawn and give a hint of the values of be chosen for the different geometrical parameters in such antennas.

Effect of AR_n - The plot of AR_A with respect to AR_n for $N = 5$, $\gamma = 0.57$ and $m = 1$ in Fig 7.2a. It is obvious from the lot that AR_A increases initially with AR_n and then becomes stable at 4.5 dB for $AR_n > 30$ dB. Therefore it is evident that for the best performance, AR_n should be very low, though the array exhibits CP behaviour even when the individual elements are linearly polarized when γ is low. However, it has already been established in Section 7.3.1 that a very low γ is undesirable because of which γ is chosen as 0.57.

Effect of N - The plot of AR_A with respect to N for $AR_n = 1.2$, $\gamma = 0.57$ and $m = 1$ is given in Fig. Fig. 7.2b. This plot has a remarkable feature which indicates that for the given configuration, $N = 5$ is the most optimum value as the AR_A is lowest for this N which is an important design objective. It is also obvious that, keeping m constant, an array with high N starts performing poorly in terms of AR which can be rectified only by altering the dimensions of the individual elements (i.e. slots) and is cumbersome.

Effect of m - Here m is the scaling factor of the guide-wavelength λ_g and from the plot of AR_A with-respect-to m (as shown in Fig. 7.2c), for different values of N ($N = 3$,5 and 7) it is observed that the curve has a periodicity of N. Moreover, the minimum possible value of AR_A is obtained only when $N = 5$ which confirms the earlier choice of N. It is also noted that a minima of AR_A occurs at $m = 11$ for $N = 5$, a fact that has been utilised in the present design as will be seen later.

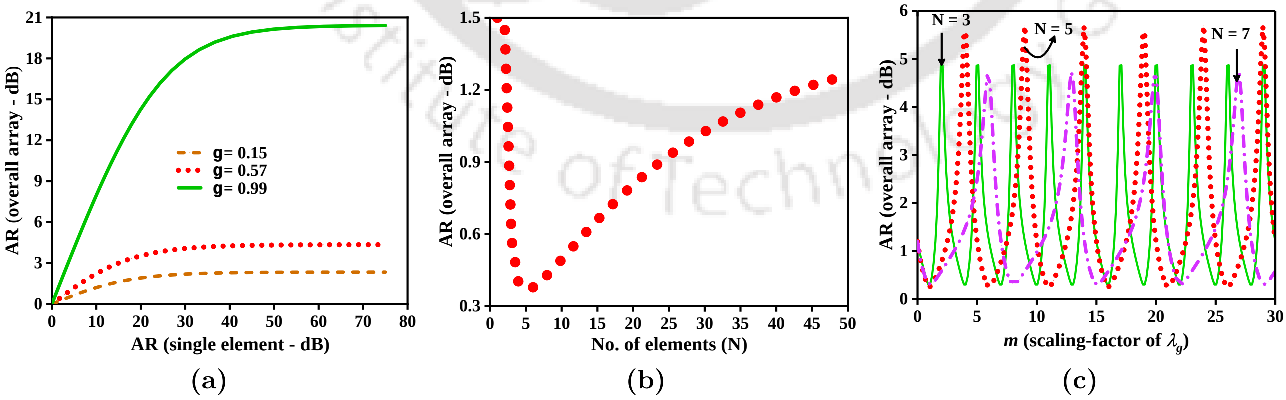

Fig. 7.2: AR_A as (a) a function of AR_n for different values of γ (b) a function of number of elements N (c) a function of scaling factor m of the guide-wavelength λ_g

7.3 Dual circularly polarized travelling wave slot antenna array

In this section, a planar wideband DCP TWA antenna with radiating slots on the ground plane is presented. These slots, which lie uniformly along the circumference of a circle, are excited in series by a microstrip feed-line underneath the substrate. To improve the gain of the antenna, a metallic reflector is provided beneath the feed network. The direction of main lobe of the antenna is controllable by varying the frequency of operation.

7.3.1 Antenna geometry

The proposed antenna comprises a slotted ground plane composed of 10 radiating slots arranged in a circular fashion. The slots are roughly rectangular in shape with two additional rectangular sections at their ends for ease of optimization to achieve best performances.

A rough initial estimation of the length of the slot is made using the following equation given in [?]

$$L_{slot} = \frac{c}{2 f_0 \sqrt{\varepsilon_{re}}} \tag{7.27}$$

where $L_{slot} = L$ is the length of the slot (as in Fig. 7.3), c is the speed of light in vacuum, f_0 is the centre frequency, and ε_{re} is the effective relative permittivity. The value of L_{slot} thus obtained is further tuned for optimum performance. The angular separation between two adjacent slots is $\frac{2\pi}{10} = 36°$ which implies that the distance between two such slots is 33 mm ($l_g \approx \lambda g + \frac{\lambda g}{10}$, where λg is the guided wavelength) to ensure CP [?] as shown in Fig. 7.3. The two sets of slots (S_1 to S_5 and S_6 to S_{10}) are arranged in opposite orientation so as to maximize the inter-port isolation and also enforce two opposite polarizations - LHCP and RHCP. The feed network shown in Fig. 7.4 comprises a microstrip ring with 10 rectangular sections (numbered R_1 to R_{10}) placed beneath each of the 10 slots. The two ports, Port 1 and Port 2 are located at the terminals of this ring-shaped feed. A square-shaped pure copper reflector (219 mm × 219 mm) lies beneath the feed network separated by an air-gap of height H_g and supported by Nylon pillars. The function of this reflector is to suppress the back-lobe of the slot array and boost the overall directivity of the antenna, thereby augmenting its gain. The array is fabricated on FR-4 substrate ($\varepsilon_r = 4.3$, $\tan\delta = 0.02$) of height 1.6 mm.

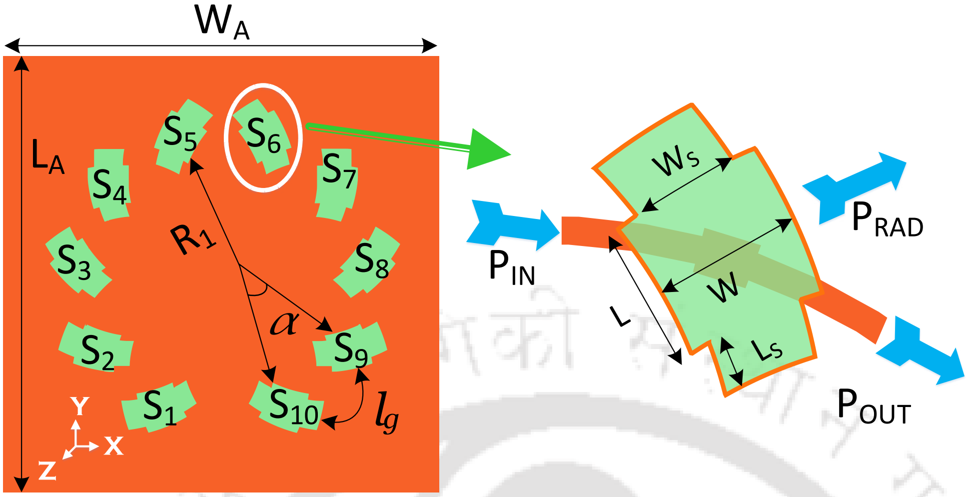

Fig. 7.3: Schematic of the slotted ground plane with 10 slots and radiating single slot model

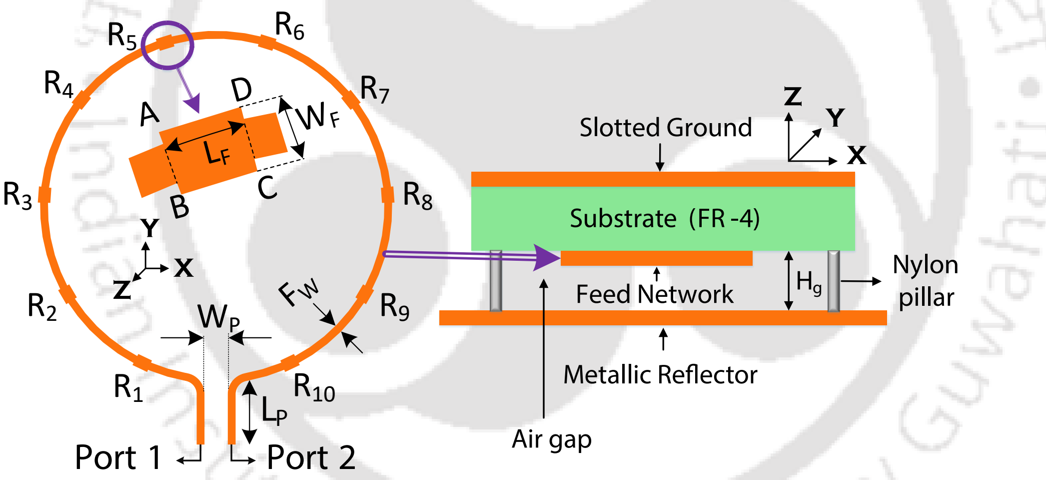

Fig. 7.4: Schematic of the feed network showing the ports and side-view of the antenna showing the metallic reflector

P$_{\text{geom.}}$	Value	P$_{\text{geom.}}$	Value	P$_{\text{geom.}}$	Value	P$_{\text{geom.}}$	Value	P$_{\text{geom.}}$	Value
W_A	165	L_A	165	R_1	52.50	α	36°	L_S	6.0
W_S	10.5	L	15.0	W	15	L_F	5.0	W_F	4.0
F_W	2.50	L_P	23.0	W_P	7.3	H_G	16.5		

Table 7.1: Values of the geometric parameters (P$_{\text{geom.}}$) of Figs. 7.3 and 7.4 (all lengths are in mm)

The normalized total power radiated by the array A_T is represented by the expression in

(7.8). As mentioned in Section 7.2, here N is the number of radiating elements (i.e. slots in this case) and γ is the power coupling coefficient of an individual slot. The latter is dependent upon the transmission coefficient of an isolated slot $\left|\tilde{S}_{21}\right|$ and is obtained from the ratio of P_{OUT} to P_{IN} as shown in Fig. 7.3.

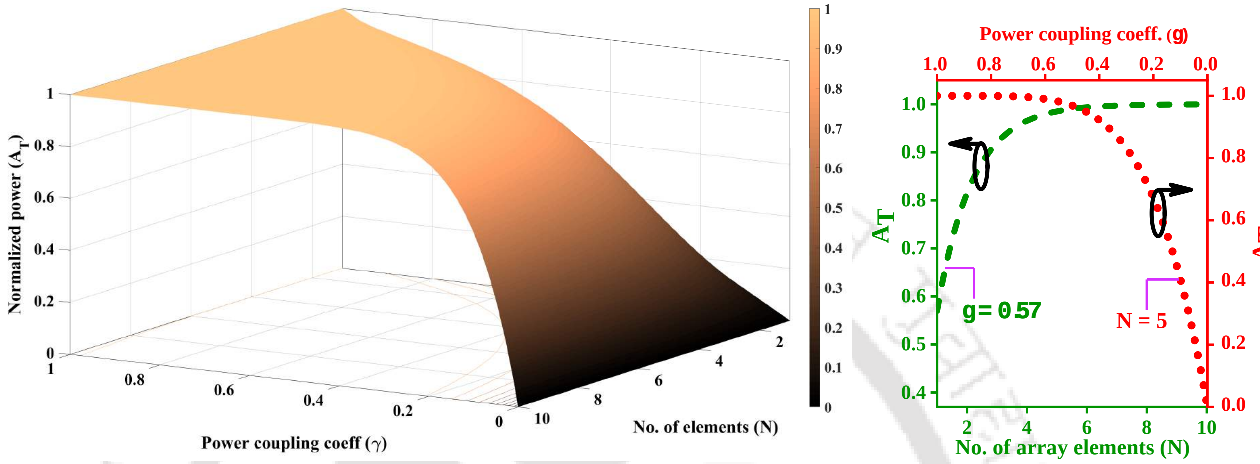

(a) (b)

Fig. 7.5: Variation of normalized radiated power A_T at 6.4 GHz (a) 3D plot of Eq. (7.8) and (b) 1D plot at $\gamma = 0.57$ and $N = 5$

The surface plot of (7.8) is shown in Fig. 7.5(a) which shows that if the array has a large size, normalized radiated power A_T reaches a high value (≥ 0.95) for small values of N only when γ is very high. This is an undesirable situation as it will result in uneven distribution of power and hence the antenna gain will suffer degradation. This also leads to impedance mismatch due to the higher value of inductive reactance [?]. On the other hand, for a too low value of γ, a large value of N will be required for high A_T which will increase the antenna footprint apart from having an adverse impact on the axial ratio (AR). Therefore, the dimensions of the rectangular section $ABCD$ (as shown in Fig. 7.4), which controls the value of γ, is critical for optimum performance.

Therefore, for the present configuration, with $\gamma = 0.57$ and $N = 5$ it is seen that $A_T = 0.987$ (Fig.7.5(b)) which implies that the first 5 slots (S_1 to S_5 corresponding to Port 1) contribute to 98.7% of the total power radiated by the antenna.

7.3.2 Analysis of the effect of slot parameter W_S

It was mentioned in the preceding section that the two additional rectangular sections of dimension $L_S \times W_S$ at their ends (Fig. 7.3) were important for design optimization. In this section the effects of W_S on both the array and single slot will be examined. Fig. 7.6(a) shows the sensitivity of AR with respect to W_S on a single slot. It can be observed that a high value of this parameter produces a low AR in an isolated slot. This CP performance of the single slot is reflected in that of the array as shown in Fig. 7.6(b), where the AR initially is seen to reduce significantly for high W_S and then becomes stable. This nature of the AR of the array is consistent with the prediction in (7.26) from which it can be said that a low AR of a single slot improves CP performance of the array as a whole.

However, a very high value of W_S has a detrimental effect on the gains of both an isolated slot and the array as shown in Fig. 7.7. Therefore, for optimum AR bandwidth and gain of the array, W_S is chosen as 10.5 mm.

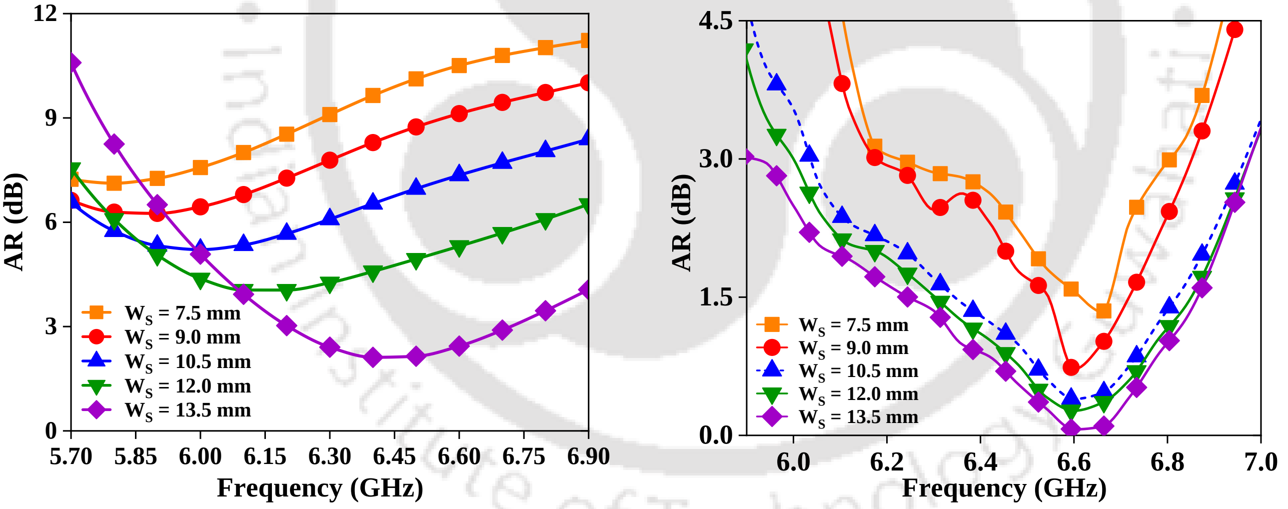

(a) (b)

Fig. 7.6: Variation of AR with different values of W_S for (a) single slot and (b) array

The slot dimension W_S influences the power coupling coefficient γ as seen in Fig. 7.8a. A too high or a too low value adversely affects the gamma which is a very important term in the expression for total power radiated by the array A_T as given in the expression (7.8). Therefore, an empirical expression for γ as a function of W_s and frequency f is obtained which is given

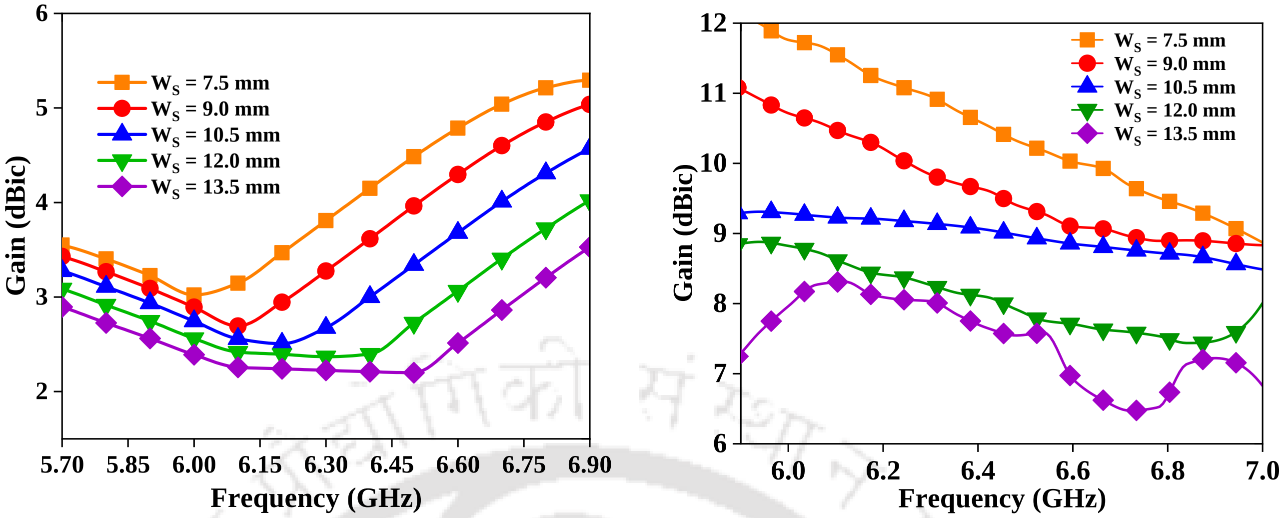

(a) (b)

Fig. 7.7: Variation of gain with different values of W_S for (a) single slot and (b) array

below

$$\gamma = -6.418 + 2.528 * f + 0.2074 * W_s - 0.2587 * f^2$$
$$- 0.07586 * f * W_s + 0.007316 * f^3 + 0.005623 * f^2 * W_s$$

From this expression, the surface plot of γ is obtained which is shown in Fig.7.8b. For the ease of visualisation, as an example, the plot of γ obtained from the above expression for $W_S = 10.5$ mm is shown along with the simulated γ in Fig. 7.8c.

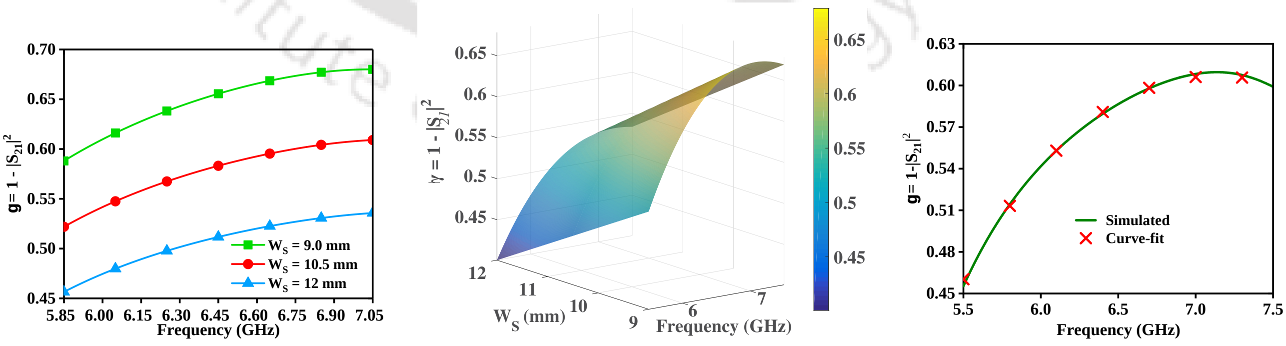

(a) (b) (c)

Fig. 7.8: (a) Plot of γ versus frequency for different W_S (b) surface plot of γ as a function of frequency f and slot-dimension W_s (c) line plot of gamma for $W_S = 10.5$ mm (both simulated and curve-fit data)

To understand the effect of W_S on the AR, the E-field lines around an isolated slot at 6.45

GHz for different values of W_S are shown in Fig. 7.9. It is obvious from the plot that a value of W_S apart from 10.5 mm, there are considerable orthogonal components of E-field which degrades the circular polarisation performance and hence increases the AR.

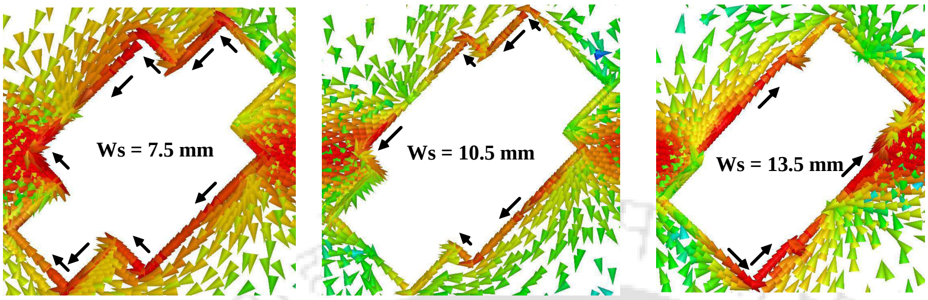

Fig. 7.9: Electric field distribution around an isolated slot at 6.45 GHz for different slot-dimensions W_S

7.3.3 Results and discussions

The fabricated prototype of the designed antenna is shown in Fig. 7.10a whereas the mounted specimen is shown in Fig. 7.10b. The simulated and measured S-parameters are shown in Fig. 7.11 from which it can be observed that the impedance bandwidth ranges from 5.85 GHz to 7.04 GHz with the centre frequency $f_0 = 6.45$ GHz. From Fig. 7.12, the 3-dB AR bandwidth is seen to lie between 6.10 GHz and 6.98 GHz which is 13.46% of $f_{AR} = 6.54$ GHz. It can therefore be inferred that the entire AR bandwidth is usable for CP operation as within this region $|S_{11}| < -10$ dB. The inter-port isolation ranges from 25 to 45 dB within the AR bandwidth.

The gain under different conditions is shown in Fig. 7.12. It can be observed that the antenna gain undergoes a significant improvement of 3 to 5 dBic with the reflector. The measured gain of the antenna with the reflector ranges from 8.2 to 9.5 dBic in its entire AR bandwidth. To reduce the bulk of the overall structure, in situations requiring high gain, the antenna may be placed at a distance H_g away from a metallic wall that will act as a reflector.

The simulated and measured radiation patterns at xz and yz planes obtained by exciting Port 1 at 6.45 GHz are shown in Fig. 7.13. The XPD in the direction of maximum radiation is around 14 dB. It can also be seen that due to the presence of the reflector the back lobe is considerably reduced and the FBR ratio is improved.

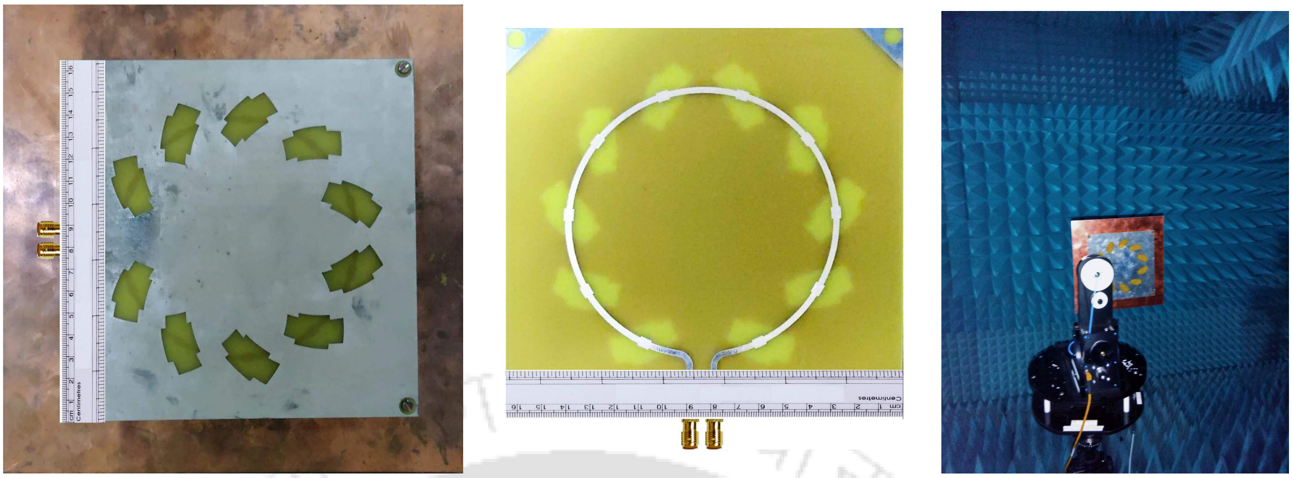
(a) (b)

Fig. 7.10: Photographs of the (a) fabricated antenna with reflector showing slotted ground plane and the feed (b) mounted antenna in anechoic chamber

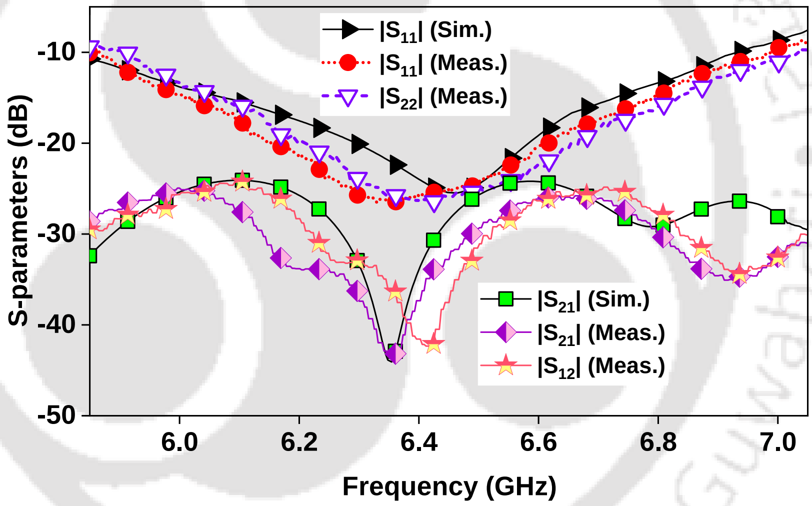

Fig. 7.11: Simulated and measured S-parameters of the proposed antenna

As mentioned earlier, since this is a series-fed array, the beam direction can be controlled by varying the frequency. Fig. 7.14 shows the variation of the main lobe direction at different frequencies. It is observed that the main lobe rotates towards the Y-axis along Φ as the frequency is changed from 6.00 GHz to 6.60 GHz. This feature is useful in satellite communications where the main beam is generally tilted at an angle with respect to the earth.

The element distance plays a vital role in determining the angle of main-lobe which is a function of phase change between the elements. This factor also decides the peak gain of the main-lobe. To demonstrate this fact, approximate expressions of main-lobe inclination θ (with

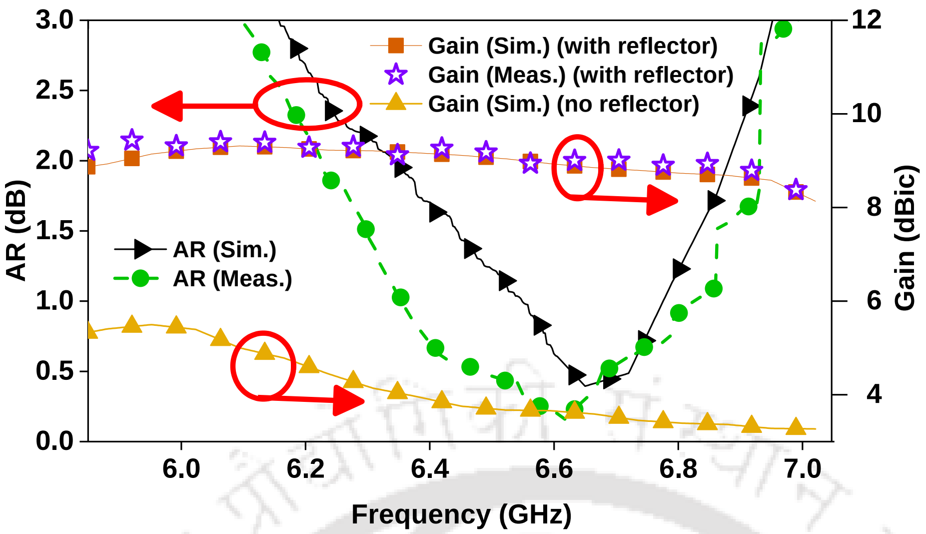

Fig. 7.12: Simulated and measured AR and gain of the proposed antenna

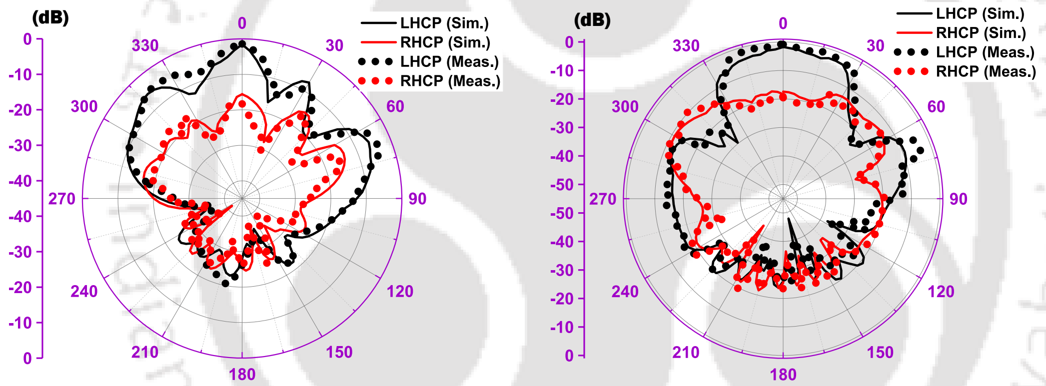

Fig. 7.13: Simulated and measured radiation patterns at 6.45 GHz upon excitation of Port 1 at xz and yz planes

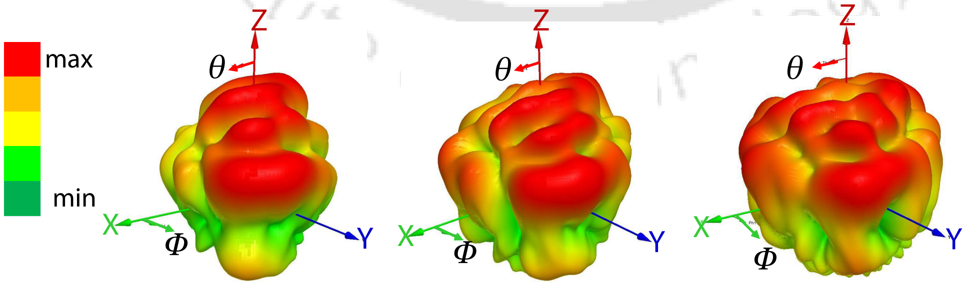

Fig. 7.14: Simulated 3D radiation pattern showing the rotation of the main lobe along Φ at three different frequencies - 6.00 GHz, 6.30 GHz and 6.60 GHz

respect to bore-sight in radians) and peak-gain (G - in dBic) in both xz- and yz-planes (as functions of normalised inter-element gap $\kappa = \frac{l}{\lambda_g}$) at 6.45 GHz are determined using curve-fitting technique which are given below:

In the xz-plane

$$\theta_{xz} = 0.9359 * \sin(12.69\kappa - 1.971) + 0.3263 * \sin(1.893\kappa - 1.341) + 0.4919 * \sin(9.536\kappa - 1.837)$$

$$G_{xz} = 26.62 * \sin(2.178\kappa - 1.527) + 18.46 * \sin(2.668\kappa - 0.8723) + 1.503 * \sin(9.379\kappa - 1.37)$$

In the yz-plane

$$\theta_{yz} = -0.06372 - 0.8045 * \cos(2.687\kappa) - 0.799 * \sin(2.687\kappa) - 0.4954 * \cos(5.374\kappa) - 0.4183 * \sin(5.374\kappa) - 0.01434 * \cos(8.061\kappa) - 0.507 * \sin(8.061\kappa)$$

$$G_{yz} = 8.179 * \sin(0.8446 * \kappa + 0.4688) + 2.464 \sin(7.674 * \kappa - 5.875) + 2.124 \sin(13.16 * \kappa - 1.953)$$

The graphs in Fig. 7.15 the validity of these expressions where θ and G obtained from curve-fitting equations are plotted against the simulated data.Thus these expressions yield fairly good initial estimations of beam directions and peak gain for a given inter-slot gap.

Like the preceding chapters, this antenna too is evaluated for its MIMO performance from ECC and diversity gain as shown in Fig. 7.16. It is obvious that the proposed antenna is suitable for 5G MIMO applications since both the parameters show satisfactory levels.

Table 7.2 gives a comparison between the antenna presented here and other state-of-the-art DCP antennas. It is seen that the proposed antenna has parameters close to most of the other antennas except the one in [?] which has a higher inter-port isolation. The latter, however, has a multilayer structure with a lossy power-divider in the feed network in contrast to this antenna which has a simple feed.

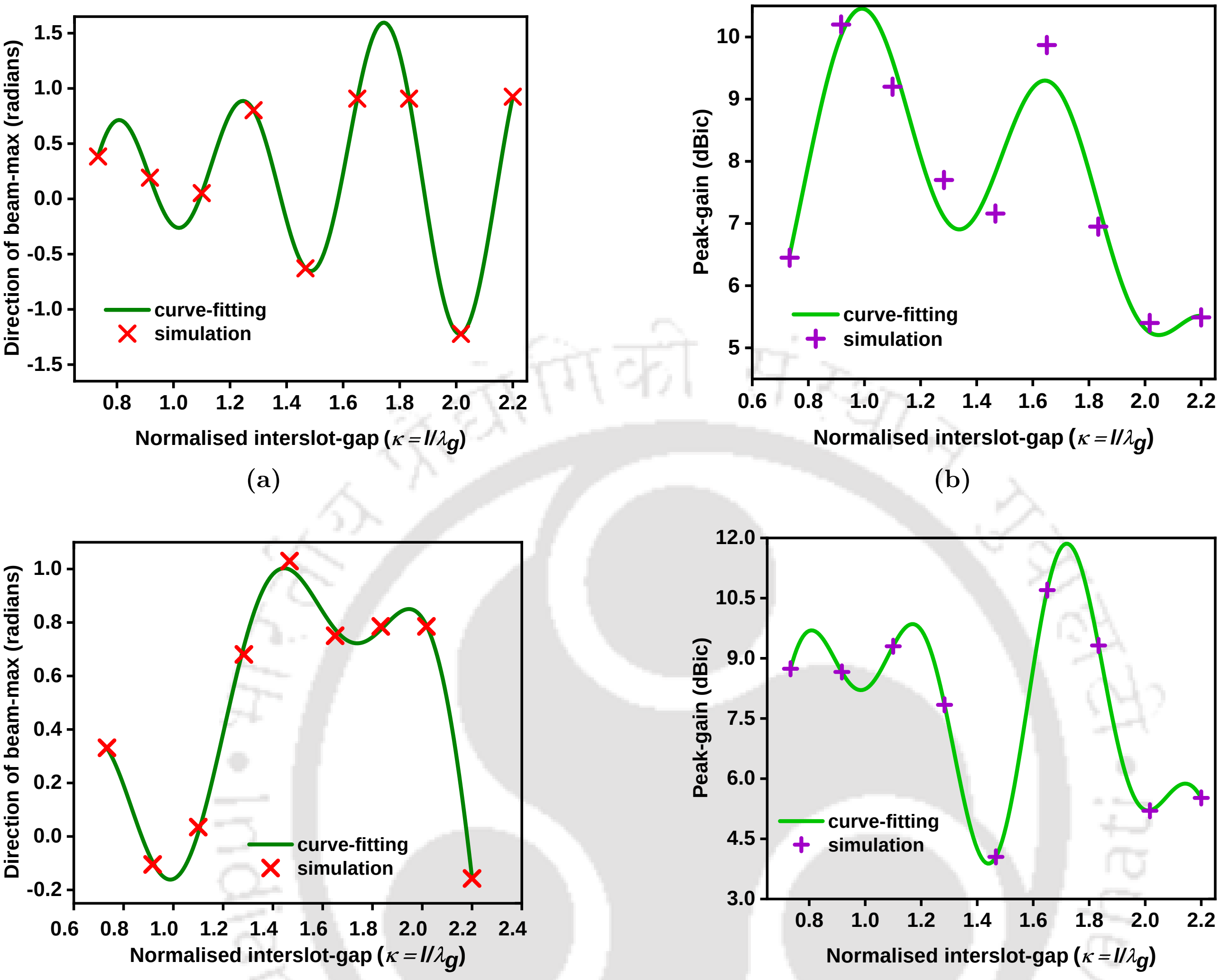

(a) (b)

(c) (d)

Fig. 7.15: (a) Main-lobe direction in xz - plane (b) peak-gain in xz - plane (c) main-lobe direction in yz - plane (d) peak-gain in in yz - plane

(a) (b)

Fig. 7.16: Variation of MIMO parameters with different values of frequency (a) ECC and (b) DG

Table 7.2: Comparison of the proposed antenna with other recently reported DCP antennas (f_0 - Centre frequency, IBW - Impedance bandwidth, $ARBW$ - AR bandwidth, I_A - Isolation within $ARBW$, G_P - Peak gain within $ARBW$)

Ref.	f_0 (GHz)	IBW (%)	ARBW (%)	I_A (dB)	G_P (dBic)
[?]	6.60	18.18	18.18	40 to 70	8.7 to 10.5
[?]	2.45	10.63	10.63	10 to 36	0 to 2.4
[?]	19.25	12.98	7.5	7 to 21	3.6 to 4.9
[?]	4.68	36	17.4	16 to 23	6 to 7.5
[?]	9.70	14.43	7.2	5 to 6	6 to 13.5
[75]	10.63	25.88	15.7	15 to 30	5 to 11.1
This work	6.45	18.46	13.46	25 to 45	8.2 to 9.5

7.4 Summary

A novel DCP antenna with radiating slots on the ground plane is presented in this chapter. A very high port-decoupling (25 to 45 dB) is achieved using the very geometry of this antenna in spite of the close physical proximity between the ports. Being a series-fed slot antenna array, the antenna has wide AR bandwidth and a high gain, the later made possible through the usage of a metallic reflector to improve the FBR. The antenna also demonstrates the ability to scan frequencies as its main beam can be steered at various angles by changing its operating frequency. The theoretical background and its analysis presented in the earlier sections of this chapter justifies the antenna design and should be of help to future antenna engineers looking to design similar type of arrays.

8

Conclusions and future work

A colossal amount of work has been done thus far on two-port and multi-port linearly polarized antennas. In this dissertation, however, the contribution of the author to the field of dual circularly polarized planar antennas is described, which have specific applications due to their certain advantages that was somewhat lacking in the existing literature. Therefore through this work we have designed several novel antennas of this type which we hope will be of use in satellite communications (especially CubeSats), polarimetry, radar altimetry, MIMO and mobile communications. This chapter reflects on these contributions and concludes the thesis. We have also given a glimpse at the direction where future antenna developers can take this work forward.

8.1 Concluding statements

We have presented four different types of DCP antennas operating at different frequency bands. The antennas were initially designed in a commercial EM solver (CST Microwave Studio) followed by their fabrication and measurements. The antennas were fabricated by PCB Power Inc. whereas the measurements were done at IIT Kanpur. A close match between the simulated and measured results were observed. Other than the four novel antennas presented in the thesis, we have also examined the different methods of port-decoupling in two-port antennas elaborating their merits and de-merits. Therefore in a nutshell we may say

(I) Chapter 1 begins by discussion of analytical formulations of microstrip patch antenna and planar slot antenna. This chapter also introduces the concept of CP and its relative advantages over LP followed by brief sections on CP planar antennas available in the literature stressing on the single-feed topology.

(II) The various modes of unwanted electromagnetic coupling between two patches placed in proximity are detailed in Chapter 2. Moreover, the necessity of highly decoupled ports is mathematically expressed showing that high bandwidth and port-isolation are essential for a simpler receiver. Hence an elaborate discussion on methods of port-decoupling in planar antennas is presented with brief notes on their corresponding advantages and drawbacks.

(III) Chapter 3 discusses a large number of DCP planar antennas from literature from which one may infer that CP slot antennas should be chosen for their high AR bandwidths. A section devoted to DCP travelling-wave antennas establishes that in spite of physical proximity between their ports, these antennas have high port-isolation if designed properly.

(IV) The antenna in Chapter 4 is a DCP slot antenna designed to operate at the S-band, has two different slots (corresponding to each polarization) in which port-decoupling was accomplished by the usage of an interdigital capacitor. This antenna has a bandwidth of 361 MHz with the port-to-port isolation ranging from 17.6 dB to 46 dB whereas the usable AR bandwidth lies between 2.113 to 2.25 GHz. Being a slot antenna, it has moderate gain and its main lobe is bi-directional in nature which has its utility in different types of applications like S-band satellite communications, MIMO communication, mobile communication (UMTS or IMT-2000), mobile satellite service (2000-2200 MHz) and communication in coal mines.

(V) In Chapter 5 a DCP antenna with a common slot (for both the polarizations) is presented that is suitable for radio altimetry in UAVs because of its lightness in weight. In this case, a metasurface based on a 4 × 2 array of split-ring resonators help in attenuating the surface waves from the transmitting port to the receiving port that is instrumental in yielding very high port-isolation. This antenna has a wide impedance bandwidth of 28.52% and a high interport isolation of 27 to 36 dB within its AR bandwidth that is 390 MHz wide centered at 4.44 GHz. The main limitation low gain of this antenna can be easily overcome by connecting a metallic reflector that will suppress its back lobe. Also, because of its low ECC, it is suitable as a diversity antenna for 5G MIMO applications.

(VI) A DCP antenna based on microstrip patch antenna is presented in Chapter 6. The designed antenna has two groups of patches, each for transmission and reception. In one such group, only the central patch with truncated opposite corners is probe-fed whereas the surrounding patches act as parasitic patches for bandwidth and gain enhancement. A DGS consisting of 4 units of complementary square spiral resonators is used to enhance the port-to-port isolation as well as the AR bandwidth. This work demonstrates the bandstop properties of the DGS by extracting its S-parameters and verifying them with its RLC-equivalent circuit. These features suggest its suitability for applications in polarimetry, satellite communications, and polarization diversity. Moreover, especially because of its large impedance bandwidth and highly decoupled ports, the usage of this antenna in a radio transceiver will allow the usage of a simpler transceiver.

(VII) A DCP travelling-wave antenna based on slotted ground plane is presented in Chapter 7. Utilizing the very geometry of this antenna, a very high interport isolation (25 to 45 dB) is obtained even though the ports are physically very close to each other. Being a slot antenna array in nature, a high AR bandwidth (880MHz) and gain (8.2 to 9.5 dBic) are obtained and using a metallic reflector the gain is further augmented by suppressing its back-lobe. Moreover, the antenna exhibits frequency scanning ability as its main beam can be steered at different angles by varying its frequency of operation.

8.2 Future work

This work has been restricted to designing antennas that have fixed beams corresponding to specific ports. Therefore a natural extension of this work could be in the area of reconfigurable antennas where the beams can be switched using active components. This technique is useful in wireless communications as it provides a CP modulation scheme for microwave tagging systems and offers double the system capacity through a frequency reuse [?].

Combining both planar antenna and bandpass filter resulting is filtering-antenna is seen to aid in miniaturization and lowering of expenses [?]. Till date, however, only a DLP filtering-antenna has been reported [?] which leaves the scope wide-open to design DCP filtering antennas.

One of the major drawbacks of the slot antennas presented in Chapters 3 and 4 is their differences in the senses of polarizations in their bi-directional beams that can be a disadvantage in some applications. As a remedy to this deficiency, desigining a frequency selective surface (FSS) to change the sense of polarization in a particular hemisphere has been suggested in [?]. Also, the very nature of the beams in such antennas yielded low-gains as discussed in these chapters that can be overcome by usage of FSS as shown in [?]. Moreover, an appropriately designed FSS for these antennas can also aid in their radar cross-section (RCS) reduction as demonstrated in [?]. Therefore, design of a novel FSS for these DCP slot antennas can be a possible extension of the latter.

Many of the slot antennas designed here (especially in Chapters 3, 4 and 6) are useful in satellite communication. It may also be pointed out that satellite exteriors are awash with a vast EM energy [?] that can be harnessed using energy harvesting DCP antennas of which no embodiments exist in the present literature and have promising potential in the domain of satellite health monitoring.

List of Publications

Journal publications

1. **S. Chaudhuri**, R.S. Kshetrimayum, and R.K. Sonkar, "High inter-port isolation dual circularly polarized slot antenna with interdigital capacitor", *International Journal of RF and Microwave Computer-Aided Engineering*, Wiley, vol. 29, e21903, 2019 (**Chapter 4**)

2. **S. Chaudhuri**, R.S. Kshetrimayum, and R.K. Sonkar, "High inter-port isolation dual circularly polarized slot antenna with split-ring resonator based novel metasurface", *AEU-International Journal of Electronics and Communications*, Elsevier, vol. 107, pp. 146—156, 2019 (**Chapter 5**)

3. **S. Chaudhuri**, M. Mishra, R.S. Kshetrimayum, R.K. Sonkar, S. Bhattacharjee, and B. Saha, "High port-to-port isolation dual circularly polarised microstrip patch antenna with multifunction DGS", accepted for publication in *IET Microwaves, Antennas & Propagation* (DOI: 10.1049/iet-map.2020.0094) (**Chapter 6**)

4. **S. Chaudhuri**, R.S. Kshetrimayum, R.K. Sonkar, and M. Mishra, "Dual circularly polarised travelling wave slot antenna array", *Electronics Letters*, IET, vol. 55, pp. 1071–1073, 2019 (**Chapter 7**)

Conference publications

1. **S. Chaudhuri**, R.S. Kshetrimayum and R.K. Sonkar, "High Inter-port Isolation Dual Circularly Polarized Modified Franklin Microstrip Antenna", *13th European Conference on Antennas and Propagation (EuCAP)*, Krakow, March 2019, pp. 1–4. (**Chapter 3**)

2. **S. Chaudhuri**, R.S. Kshetrimayum, R.K. Sonkar, and D. Mishra, "Dual Circularly Polarized Slot Antenna with Novel Isolator", *41st Photonics & Electromagnetics Research Symposium (PIERS) 2019*, Rome, June 2019. (**Chapter 3**)

Other publications

1. **S. Chaudhuri**, R.S. Kshetrimayum, R.K. Sonkar and D. Mishra, "High Gain Dual Linearly Polarized Patch Antenna Array", *41st Photonics & Electromagnetics Research Symposium (PIERS) 2019*, Rome, June 2019.

2. **S. Chaudhuri**, M. Mishra, R.S. Kshetrimayum, R.K. Sonkar, H. Chel, and V.K. Singh, “Rectangular DRA array for 24 GHz ISM band applications”, *IEEE Antennas and Wireless Propagation Letters*, IEEE, vol. 19, issue. 9, pp. 1501—1505, September 2020
3. **S. Chaudhuri**, R.S. Kshetrimayum, R.K. Sonkar, and M. Mishra, “Wideband Rectangular Dielectric Resonator Antenna Array for ISM Band Applications”, *TENSYMP 2020, Dhaka*, IEEE

A

Appendix

Contents

A.1 Field equations in microstrip patch antenna

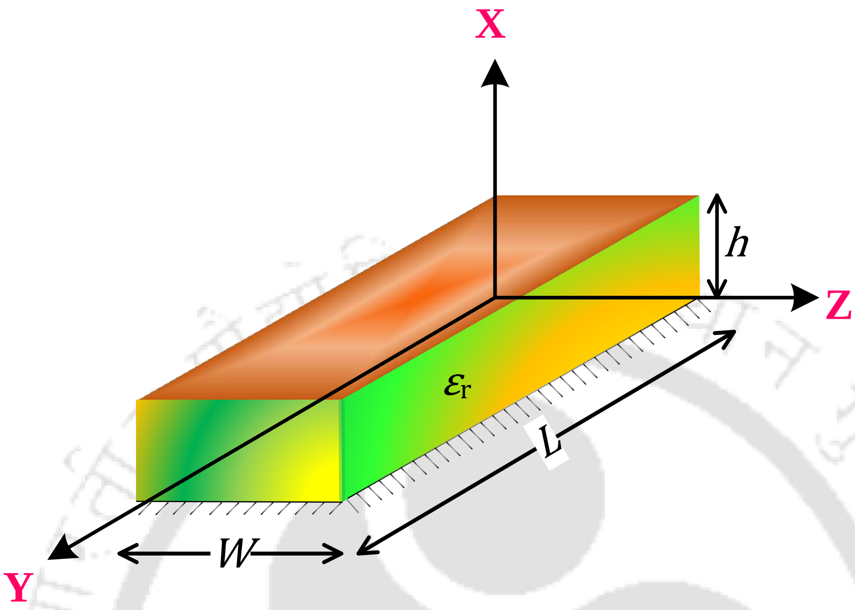

Fig. A.1: Geometry of microstrip patch antenna [2]

Suppose A_x is the vector potential that satisfies the Helmholtz equation

$$\nabla^2 A_x + k^2 A_x = 0 \tag{A.1}$$

Using the separation of variables technique, the general solution of the above equation is

$$\begin{aligned} A_x = {} & [A_1 \cos(k_x x) + A_2 \sin(k_x x)] \times [A_3 \cos(k_y y) + A_4 \sin(k_y y)] \\ & \times [A_5 \cos(k_z z) + A_6 \sin(k_z z)] \end{aligned} \tag{A.2}$$

where k_x, k_y, and k_z are the wave-numbers along X-, Y-, and Z- axes respectively, that are determined by the boundary conditions. The E- and H-field components in terms of vector potential A_x is given by

$$E_x = -\frac{j}{\omega\mu\varepsilon}\left(\partial_{xx} + k^2\right) A_x \qquad \text{and} \qquad H_x = 0 \tag{A.3}$$

$$E_y = -\frac{j}{\omega\mu\varepsilon}\partial_{xy}A_x \qquad \text{and} \qquad H_y = \frac{1}{\mu}\partial_z A_x \tag{A.4}$$

$$E_z = -\frac{j}{\omega\mu\varepsilon}\partial_{xz}A_x \qquad \text{and} \qquad H_z = -\frac{1}{\mu}\partial_y A_x \tag{A.5}$$

$\left(\partial_{xx} \equiv \frac{\partial^2}{\partial_{x^2}}, \partial_{xy} \equiv \frac{\partial^2}{\partial_x \partial_y}, \partial_{xz} \equiv \frac{\partial^2}{\partial_x \partial_z}, \partial_x \equiv \frac{\partial}{\partial_x}, \partial_y \equiv \frac{\partial}{\partial_y}, \text{and } \partial_z \equiv \frac{\partial}{\partial_z}\right)$ with the following boundary conditions

$$E_y\left(x=0, 0 \le y \le L, 0 \le z \le W\right) = 0 \quad \text{and} \quad E_y\left(x=h, 0 \le y \le L, 0 \le z \le W\right) = 0 \tag{A.6}$$

$$H_y\left(0 \le x \le h, 0 \le y \le L, z=0\right) = 0 \quad \text{and} \quad H_y\left(0 \le x \le h, 0 \le y \le L, z=W\right) = 0 \tag{A.7}$$

$$H_z\left(0 \le x \le h, y=0, 0 \le z \le W\right) = 0 \quad \text{and} \quad H_z\left(0 \le x \le h, y=L, 0 \le z \le W\right) = 0 \tag{A.8}$$

Applying the above boundary conditions to (A.3), (A.4), and (A.5), the following solutions are obtained

$$A_x = A_{mnp}\cos\left(k_x x\right)\cos\left(k_y y\right)\cos\left(k_z z\right) \tag{A.9}$$

and

$$\begin{cases} k_x = \frac{m\pi}{h}, & m = 0, 1, 2, \ldots \\ k_y = \frac{n\pi}{L}, & n = 0, 1, 2, \ldots \\ k_z = \frac{p\pi}{W}, & p = 0, 1, 2, \ldots \end{cases} \tag{A.10}$$

where k_x, k_y and k_z are constrained by the condition

$$k_x^2 + k_y^2 + k_z^2 = 4\pi^2 f_r^2 \mu\varepsilon \tag{A.11}$$

The term f_r is the resonant frequency and is given by

$$f_r = \frac{1}{2\pi\sqrt{\mu\varepsilon}}\left[\left(\frac{m\pi}{h}\right)^2 + \left(\frac{n\pi}{L}\right)^2 + \left(\frac{p\pi}{W}\right)^2\right]^{\frac{1}{2}} \tag{A.12}$$

Substituting (A.9) into (A.3), (A.4), and (A.5), the following field equations are obtained

$$E_x = -j\frac{(k^2 - k_x^2)}{\omega\mu\varepsilon}A_{mnp}\cos(k_x x)\cos(k_y y)\cos(k_z z) \qquad \text{and} \qquad H_x = 0 \tag{A.13}$$

$$E_y = -j\frac{k_x k_y}{\omega\mu\varepsilon}A_{mnp}\sin(k_x x)\sin(k_y y)\cos(k_z z)\,; \quad H_y = -\frac{k_z}{\mu}A_{mnp}\cos(k_x x)\cos(k_y y)\sin(k_z z) \tag{A.14}$$

$$E_z = -j\frac{k_x k_z}{\omega\mu\varepsilon}A_{mnp}\sin(k_x x)\cos(k_y y)\sin(k_z z)\,; \quad H_z = \frac{k_y}{\mu}A_{mnp}\cos(k_x x)\sin(k_y y)\cos(k_z z) \tag{A.15}$$

The dominant mode (TM^x_{010}) is generated by the lowest frequency which is when $L > W \ggg h$ and is given by

$$f_r\big|_{010} = \frac{c}{2L\sqrt{\varepsilon_r}} \tag{A.16}$$

If the antenna structure is such that $L > W > \frac{L}{2} \ggg h$, the next higher-order mode i.e. TM^x_{001} mode is generated whose resonance frequency is

$$f_r\big|_{001} = \frac{c}{2W\sqrt{\varepsilon_r}} \tag{A.17}$$

On the other hand, for $L > \frac{L}{2} > W \ggg h$, the second-order mode of TM^x_{020} is generated whose resonant frequency is

$$f_r\big|_{020} = \frac{c}{L\sqrt{\varepsilon_r}} \tag{A.18}$$

A.2 Polarization

The term *polarization* for an EM wave is related to the direction of its associated electric field (E-field). In other words, the geometric shape described by the tip of the E-field vector in a plane determines the polarization. In general cases, an EM wave propagating in z- axis has both x and y components of the electric field whose expression is given by [76]

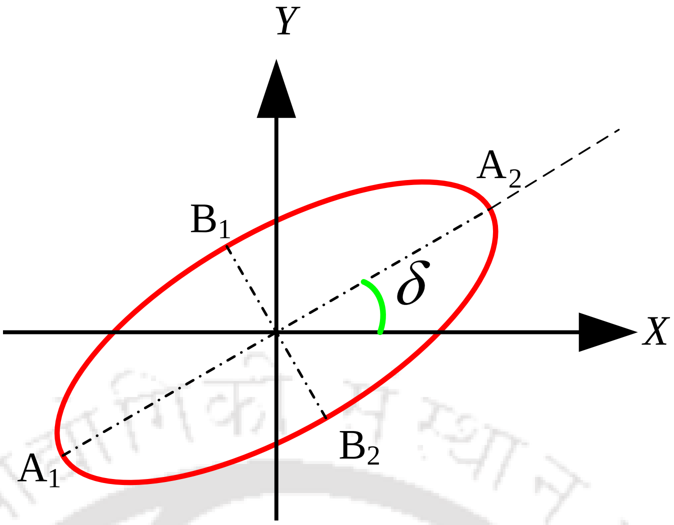

Fig. A.2: Path traced by tip of E-field vector for elliptical polarization [76]

$$\vec{E} = (\hat{x}E_{x0} + \hat{y}E_{yo})\exp(-jkz) \tag{A.19}$$

The phase-components in time-domain can be expressed as

$$\vec{E}_{x0} = |E_{x0}|\cos(\omega t + \phi_x) = \varrho_x \tag{A.20}$$

and

$$\vec{E}_{y0} = |E_{y0}|\cos(\omega t + \phi_y) = \varrho_y \tag{A.21}$$

where ϕ_x and ϕ_y represent the phase angles of the field components. Equations (A.20) and (A.21) may be written as

$$\varrho_x = |E_{x0}|\cos(\omega t)\cos(\phi_x) - |E_{x0}|\sin(\omega t)\sin(\phi_x) \tag{A.22}$$

and

$$\varrho_y = |E_{y0}|\cos(\omega t)\cos(\phi_y) - |E_{y0}|\sin(\omega t)\sin(\phi_y) \tag{A.23}$$

or

$$\frac{\varrho_x}{|E_{x0}|} = \cos(\omega t)\cos(\phi_x) - \sin(\omega t)\sin(\phi_x) \tag{A.24}$$

and

$$\frac{\varrho_y}{|E_{y0}|} = \cos(\omega t)\cos(\phi_y) - \sin(\omega t)\sin(\phi_y) \tag{A.25}$$

or

$$\frac{\varrho_x}{|E_{x0}|}\sin(\phi_y) - \frac{\varrho_y}{|E_{y0}|}\sin(\phi_x) = \cos(\omega t)\left[\cos(\phi_x)\sin(\phi_y) - \cos(\phi_y)\sin(\phi_x)\right] \tag{A.26}$$

and

$$\frac{\varrho_x}{|E_{x0}|}\cos(\phi_y) - \frac{\varrho_y}{|E_{y0}|}\cos(\phi_x) = \sin(\omega t)\left[\sin(\phi_x)\cos(\phi_y) - \sin(\phi_y)\cos(\phi_x)\right] \tag{A.27}$$

Upon squaring both sides of the above two expressions and adding them, one obtains

$$\left(\frac{\varrho_x}{|E_{x0}|}\right)^2 + \left(\frac{\varrho_y}{|E_{y0}|}\right)^2 - 2\frac{\varrho_x}{|E_{x0}|}\frac{\varrho_y}{|E_{y0}|}\cos\phi = \sin^2\phi \tag{A.28}$$

where $\phi = \phi_y - \phi_x$

It is thus obvious that the general case is that of an elliptical polarization which is pictorially depicted in Fig. A.2.

The following cases are of special interest

(i) $|E_{x0}| = 0$ or $|E_{y0}| = 0$ - In such a case, the AR$\rightarrow \infty$, and the polarization is linear as the ellipse assumes the shape of a straight line.

(ii) $|E_{x0}| = |E_{x0}|$ and $\phi = \pm 90^\circ$ - This is the condition for circular polarization as the minor and the major axis of the ellipse are of the same magnitude.

A.3 Larmor frequency [1]

Let us consider an electron moving in a circular loop of radius r at an angle θ with respect to an applied magnetic field $\vec{B}$. The electron has an angular momentum $\boldsymbol{L}$ and a magnetic

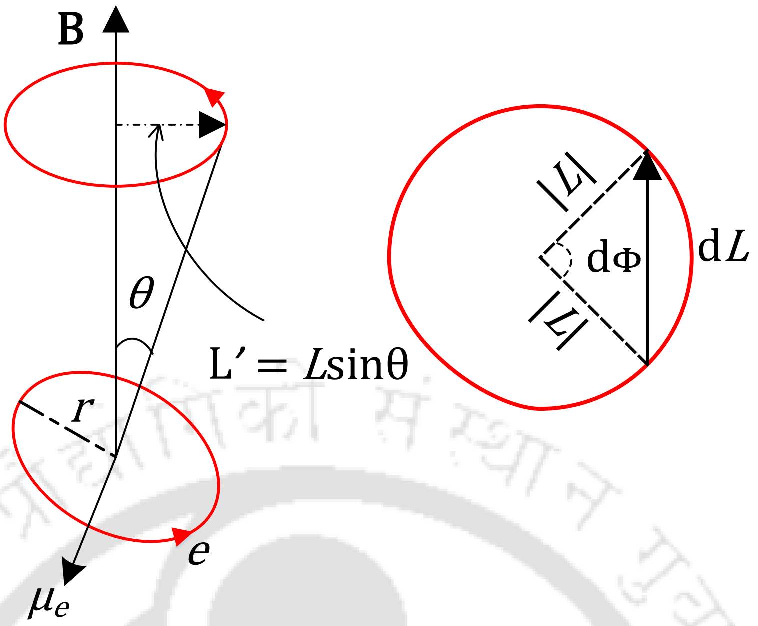

Fig. A.3: Larmor radius (side- and top-view) of the circle traced by an electron in a loop in an applied magnetic field [1]

moment $\boldsymbol{\mu_e}$. The magnetic field exerts a torque $\vec{\tau}$ on the dipole created by the circling electron given by

$$\vec{\tau} = \boldsymbol{\mu_e} \times \vec{B} \tag{A.29}$$

The angular impulse $\vec{\tau}dt$ produces a change in angular momentum such that

$$\vec{\tau}dt = d\boldsymbol{L} \tag{A.30}$$

Thus, from the circle traced out by the tip of this vector $\boldsymbol{L}$(top view shown in Fig. A.3) the following condition is satisfied

$$d\Phi = d\boldsymbol{L}/\boldsymbol{L'} = \frac{\vec{\tau}dt}{\boldsymbol{L}\sin\theta} \tag{A.31}$$

Hence, the precisional angular velocity $\omega_p = \left|\frac{d\Phi}{dt}\right|$, may be written as

$$\omega_p = \frac{|\vec{\tau}|}{|\boldsymbol{L}\sin\theta|} = \frac{|\boldsymbol{\mu_e}|\left|\vec{B}\right|\sin\theta}{|\boldsymbol{L}|\sin\theta} \tag{A.32}$$

Therefore

$$\omega_p = \frac{\mu_e B}{L} \tag{A.33}$$

where $|\boldsymbol{\mu_e}| = \mu_e$, $\left|\vec{B}\right| = B$ and $|\boldsymbol{L}| = L$. Now, the magnetic moment of a circular current is given by

$$\mu = IA \tag{A.34}$$

and the angular velocity ω and current I are related by

$$I = ev = \frac{e\omega}{2\pi} \tag{A.35}$$

where e is the electronic charge. Furthermore, the angular momentum may be written as

$$L = mr^2\omega \tag{A.36}$$

where m is the mass of an electron. Therefore, the precisional angular velocity ω_p is written as

$$\omega_p = \frac{e\omega}{2\pi}\frac{\pi r^2}{mr^2\omega}B = \frac{eB}{2m} \tag{A.37}$$

Hence, the Larmor frequency is

$$f_p = \frac{eB}{4\pi m} \tag{A.38}$$

A.4 Circular birefringence [1]

In an ionized medium, the left- and right-handed components of an EM wave travel at different frequencies because of the dissimilar refractive indices experienced by each of these components. With respect to this medium, the left-(L) and right-handed(R) components rotate with frequencies - $f+f_p$ and $f-f_p$, where f_p denotes the Larmor frequency. Since the medium is dispersive, the refractive indices are functions of frequencies given by

$$n_L = n\left(f - f_p\right) \qquad \text{and} \qquad n_R = n\left(f + f_p\right) \tag{A.39}$$

The optical path difference of the L and R components after traversing a distance d is given by $\left(n_L - n_R\right)d$. Using the Taylor's series expansion and neglecting the higher order terms, the following equivalent expression is obtained

$$n_R - n_L = n\left(f + f_p\right) - n\left(f - f_p\right) \tag{A.40}$$

or

$$n_R - n_L = \left[n\left(f\right) + \frac{dn\left(f\right)}{df} f_p\right] - \left[n\left(f\right) - \frac{dn\left(f\right)}{df} f_p\right] \tag{A.41}$$

or

$$n_R - n_L = 2 f_p \frac{dn\left(f\right)}{df} \tag{A.42}$$

By substituting the expression for Larmor frequency from (A.38) and noting that $\frac{dn\left(f\right)}{df} = \frac{\lambda^2}{c}\frac{dn\left(f\right)}{d\lambda}$ we get

$$n_R - n_L = 2\left(\frac{eB}{4\pi}\right)\frac{dn\left(f\right)}{df} \tag{A.43}$$

If ϕ_L and ϕ_R are the phase changes undergone by the L and R components respectively, the net phase difference $\Delta\phi$ is given by

$$\Delta\phi = 0.5\left(\phi_L - \phi_R\right) \tag{A.44}$$

or

$$\Delta\phi = \frac{1}{2}\left(\frac{2\pi d}{\lambda}\right)\left(\frac{eB}{4\pi m}\right)\left(\frac{\lambda^2}{c}\frac{dn\left(f\right)}{d\lambda}\right) \tag{A.45}$$

or

$$\Delta\phi = \left(\frac{e}{2m}\frac{\lambda}{c}\frac{dn\left(f\right)}{d\lambda}\right)Bd \tag{A.46}$$

Thus the rotation angle is proportional to both wavelength λ and the dispersion in the medium $\frac{dn\left(f\right)}{d\lambda}$. Therefore, a plane polarized wave, which is a linear sum of a right-hand and a left-hand wave, will rotate as it propagates. Hence it is clear that the effect is more pronounced at the lower frequencies.

A.5 AR measurement technique

The general form of E-field components of RHCP and LHCP may be written as

$$\vec{E}_{RHCP} = \frac{1}{\sqrt{2}}\left(\vec{E}_H + j\vec{E}_V\right) \qquad \text{and} \qquad \vec{E}_{LHCP} = \frac{1}{\sqrt{2}}\left(\vec{E}_H - j\vec{E}_V\right) \tag{A.47}$$

The rectangular horn antenna employed to measure the AR has high polarization purity and is rotated in fixed angular steps. The next step is to show that dual linearly polarized (DLP) components at each such step may be directly converted to CP components. The horizontal and vertical components may be written as

$$\vec{E}_H = \vec{E}_{Hr} + j\vec{E}_{Hi} \qquad \text{and} \qquad \vec{E}_V = \vec{E}_{Vr} + j\vec{E}_{Vi} \tag{A.48}$$

where

$$\vec{E}_{Hr} = \vec{H}_A \cos\left(H_P\right) \qquad \text{and} \qquad \vec{E}_{Hi} = \vec{H}_A \sin\left(H_P\right) \tag{A.49}$$

and

$$\vec{E}_{Vr} = \vec{V}_A \cos\left(V_P\right) \qquad \text{and} \qquad \vec{E}_{Vi} = \vec{V}_A \sin\left(V_P\right) \tag{A.50}$$

where the horizontal and vertical amplitude components ($\vec{H}_A$, $\vec{V}_A$) and their phase-angles ($\vec{H}_P$, $\vec{V}_P$) are measured at each θ in the far-field region of the antenna for $\phi = 0°$ and $\phi = 90°$ as shown in Fig. 1.3. Inserting (A.49) and (A.50) in (A.48), the CP components may be re-written as [?]

$$E_{RHCP} = \frac{1}{\sqrt{2}}\left\{\left[\vec{H}_A \cos\left(H_P\right) + \vec{V}_A \sin\left(V_P\right)\right] + j\left[\vec{H}_A \sin\left(H_P\right) - \vec{V}_A \cos\left(V_P\right)\right]\right\} \tag{A.51}$$

and

$$E_{LHCP} = \frac{1}{\sqrt{2}}\left\{\left[\vec{H}_A \cos\left(H_P\right) - \vec{V}_A \sin\left(V_P\right)\right] + j\left[\vec{H}_A \sin\left(H_P\right) + \vec{V}_A \cos\left(V_P\right)\right]\right\} \tag{A.52}$$

Bibliography

[1] F. L. Pedrotti and P. Bandettini, "Faraday rotation in the undergraduate advanced laboratory," *American Journal of Physics*, vol. 58, no. 6, pp. 542–545, 1990.

[2] C. A. Balanis, *Antenna theory: analysis and design*, 3rd ed., 2016.

[3] S. S. Gao, Q. Luo, and F. Zhu, *Circularly polarized antennas*, 1st ed. John Wiley & Sons, 2013.

[4] K.-L. Wong, W.-H. Hsu, and C.-K. Wu, "Single-feed circularly polarized microstrip antenna with a slit," *Microwave and Optical Technology Letters*, vol. 18, no. 4, pp. 306–308, 1998.

[5] N. Nasimuddin, *Microstrip antennas*, 1st ed. BoD–Books on Demand, 2011.

[6] Z. N. Chen, X. Qing *et al.*, "A compact circularly polarized slotted-slit-microstrip patch antenna," in *Asia-Pacific Microwave Conference 2011.* IEEE, 2011, pp. 582–585.

[7] K. Y. Lam, K.-M. Luk, K. F. Lee, H. Wong, and K. B. Ng, "Small circularly polarized u-slot wideband patch antenna," *IEEE Antennas and Wireless Propagation Letters*, vol. 10, pp. 87–90, 2011.

[8] Z. N. Chen, X. Qing *et al.*, "Asymmetric-circular shaped slotted microstrip antennas for circular polarization and rfid applications," *IEEE Transactions on Antennas and Propagation*, vol. 58, no. 12, pp. 3821–3828, 2010.

[9] ——, "Slotted microstrip antennas for circular polarization with compact size," *IEEE Antennas and Propagation Magazine*, vol. 55, no. 2, pp. 124–137, 2013.

[10] S. S. Yang, K.-F. Lee, A. A. Kishk, and K.-M. Luk, "Design and study of wideband single feed circularly polarized microstrip antennas," *Progress In Electromagnetics Research*, vol. 80, pp. 45–61, 2008.

[11] W.-S. Chen, C.-K. Wu, and K.-L. Wong, "Novel compact circularly polarized square microstrip antenna," *IEEE Transactions on Antennas and propagation*, vol. 49, no. 3, pp. 340–342, 2001.

[12] M. Wong, H. Wong, and K.-M. Luk, "Small circularly polarised patch antenna," *Electronics Letters*, vol. 41, no. 16, pp. 887–888, 2005.

[13] R. Caso, A. Buffi, M. R. Pino, P. Nepa, and G. Manara, "A novel dual-feed slot-coupling feeding technique for circularly polarized patch arrays," *IEEE Antennas and Wireless Propagation Letters*, vol. 9, pp. 183–186, 2010.

[14] W.-M. Li, B. Liu, and H.-W. Zhao, “The U-shaped structure in dual-band circularly polarized slot antenna design,” *IEEE Antennas and Wireless Propagation Letters*, vol. 13, pp. 447–450, 2014.

[15] P. Mousavi, B. Miners, and O. Basir, “Wideband L-shaped circular polarized monopole slot antenna,” *IEEE Antennas and Wireless Propagation Letters*, vol. 9, pp. 822–825, 2010.

[16] J.-Y. Sze, K.-L. Wong, and C.-C. Huang, “Coplanar waveguide-fed square slot antenna for broadband circularly polarized radiation,” *IEEE Transactions on antennas and propagation*, vol. 51, no. 8, pp. 2141–2144, 2003.

[17] K.-M. Chang, R.-J. Lin, I.-C. Deng, and Q.-X. Ke, “A novel design of a microstrip-fed shorted square-ring slot antenna for circular polarization,” *Microwave and Optical Technology Letters*, vol. 49, no. 7, pp. 1684–1687, 2007.

[18] K. Kandasamy, B. Majumder, J. Mukherjee, and K. P. Ray, “Dual-band circularly polarized split ring resonators loaded square slot antenna,” *IEEE Transactions on antennas and Propagation*, vol. 64, no. 8, pp. 3640–3645, 2016.

[19] P. K. Tharehalli Rajanna, K. Rudramuni, and K. Kandasamy, “Compact triband circularly polarized planar slot antenna loaded with split ring resonators,” *International Journal of RF and Microwave Computer-Aided Engineering*, vol. 29, no. 12, p. e21953, 2019.

[20] P. M. Paul, K. Kandasamy, and M. Sharawi, “A tri-band slot antenna loaded with split ring resonators,” *Microwave and Optical Technology Letters*, vol. 59, no. 10, pp. 2638–2643, 2017.

[21] A. Siahcheshm, J. Nourinia, C. Ghobadi, M. Karamirad, and B. Mohammadi, “A broadband circularly polarized cavity-backedArchimedean spiral array antenna for c-band applications,” *AEU-International Journal of Electronics and Communications*, vol. 81, pp. 218–226, 2017.

[22] L. Zhou, S. Liu, Y. Wei, Y. Chen, and N. Gao, “Dual-band circularly-polarised antenna based on complementary two turns spiral resonator,” *Electronics letters*, vol. 46, no. 14, pp. 970–971, 2010.

[23] L. Yang, L.-J. Xu, Y.-M. Bo, and M. Zhang, “A single-feed dual-band circularly polarized microstrip antenna with spiral slots,” in *2017 International Applied Computational Electromagnetics Society Symposium (ACES)*. IEEE, 2017, pp. 1–2.

[24] S. Singhal, M. M. Sharma, and R. P. Yadav, “Epsilon-shaped circularly polarized strip and slot-loaded ultra-wideband antenna for ku-band and k-band,” *International Journal of RF and Microwave Computer-Aided Engineering*, vol. 30, no. 5, p. e22142, 2020.

[25] A. Kumar, A. Q. Ansari, B. K. Kanaujia, and J. Kishor, “Dual circular polarization with reduced mutual coupling among two orthogonally placed CPW-fed microstrip antennas for broadband applications,” *Wireless Personal Communications*, vol. 107, no. 2, pp. 759–770, 2019.

[26] C. Chen and E. Yung, “Dual-band dual-sense circularly-polarized CPW-fed slot antenna with two spiral slots loaded,” *IEEE Transactions on Antennas and Propagation*, vol. 57, no. 6, pp. 1829–1833, 2009.

[27] M. Niroo-Jazi, T. A. Denidni, M. Chaharmir, and A. Sebak, “A hybrid isolator to reduce electromagnetic interactions between Tx/Rx antennas,” *IEEE Antennas and Wireless Propagation Letters*, vol. 13, pp. 75–78, 2013.

[28] S. Gao, L. Li, P. Gardner, and P. Hall, “Wideband dual-polarised microstrip patch antenna,” *Electronics Letters*, vol. 37, no. 20, pp. 1213–1214, 2001.

[29] A. U. Zaman, L. Manholm, and A. Derneryd, “Dual polarised microstrip patch antenna with high port isolation,” *Electronics Letters*, vol. 43, no. 10, pp. 551–552, 2007.

[30] G. Parker, Y. Antar, A. Ittipiboon, and A. Petosa, “Dual polarised microstrip ring antenna with good isolation,” *Electronics Letters*, vol. 34, no. 11, pp. 1043–1044, 1998.

[31] J.-S. Row, S.-H. Yeh, and K.-L. Wong, “Compact dual-polarized microstrip antennas,” *Microwave and Optical Technology Letters*, vol. 27, no. 4, pp. 284–287, 2000.

[32] B. Lindmark, “A novel dual polarized aperture coupled patch element with a single layer feed network and high isolation,” in *IEEE Antennas and Propagation Society International Symposium 1997. Digest*, vol. 4. IEEE, 1997, pp. 2190–2193.

[33] C.-X. Mao and Q.-X. Chu, “Compact coradiator UWB-MIMO antenna with dual polarization,” *IEEE transactions on antennas and propagation*, vol. 62, no. 9, pp. 4474–4480, 2014.

[34] M. Naser-Moghadasi, R. Ahmadian, Z. Mansouri, F. B. Zarrabi, and M. Rahimi, “Compact EBG structures for reduction of mutual coupling in patch antenna MIMO arrays,” *Progress In Electromagnetics Research*, vol. 53, pp. 145–154, 2014.

[35] M. T. Islam and M. S. Alam, “Compact EBG structure for alleviating mutual coupling between patch antenna array elements,” *Progress In Electromagnetics Research*, vol. 137, pp. 425–438, 2013.

[36] H. S. Farahani, M. Veysi, M. Kamyab, and A. Tadjalli, “Mutual coupling reduction in patch antenna arrays using a UC-EBG superstrate,” *IEEE Antennas and Wireless Propagation Letters*, vol. 9, pp. 57–59, 2010.

[37] Y. Fu, Q. Zheng, Q. Gao, and G. Zhang, “Mutual coupling reduction between large antenna arrays using electromagnetic bandgap (EBG) structures,” *Journal of Electromagnetic Waves and Applications*, vol. 20, no. 6, pp. 819–825, 2006.

[38] S. D. Assimonis, T. V. Yioultsis, and C. S. Antonopoulos, “Design and optimization of uniplanar EBG structures for low profile antenna applications and mutual coupling reduction,” *IEEE Transactions on Antennas and Propagation*, vol. 60, no. 10, pp. 4944–4949, 2012.

[39] M. A. Abdalla, A. M. Abdelreheem, M. H. Abdegellel, and A. M. Ali, “Surface wave and mutual coupling reduction between two element array MIMO antenna,” in *2013 IEEE Antennas and Propagation Society International Symposium (APSURSI)*. IEEE, 2013, pp. 178–179.

[40] S.-W. Su, C.-T. Lee, and F.-S. Chang, “Printed MIMO-antenna system using neutralization-line technique for wireless USB-dongle applications,” *IEEE Transactions on Antennas and Propagation*, vol. 60, no. 2, pp. 456–463, 2011.

[41] S. Zhang and G. F. Pedersen, "Mutual coupling reduction for UWB MIMO antennas with a wideband neutralization line," *IEEE Antennas and Wireless Propagation Letters*, vol. 15, pp. 166–169, 2015.

[42] Y. Wang and Z. Du, "A wideband printed dual-antenna system with a novel neutralization line for mobile terminals," *IEEE antennas and wireless propagation letters*, vol. 12, pp. 1428–1431, 2013.

[43] S.-W. Su and C.-T. Lee, "Printed two monopole-antenna system with a decoupling neutralization line for 2.4-ghz MIMO applications," *Microwave and Optical Technology Letters*, vol. 53, no. 9, pp. 2037–2043, 2011.

[44] Y. Yu, L. Yi, X. Liu, and Z. Gu, "Compact dual-frequency microstrip antenna array with increased isolation using neutralization lines," *Progress In Electromagnetics Research*, vol. 56, pp. 95–100, 2015.

[45] J.-H. Huang, W.-J. Chang, and C. F. Jou, "Dual-band MIMO antenna with high isolation application by using neutralizing line," *Progress In Electromagnetics Research*, vol. 48, pp. 15–19, 2014.

[46] D. Guha, S. Biswas, M. Biswas, J. Y. Siddiqui, and Y. M. Antar, "Concentric ring-shaped defected ground structures for microstrip applications," *IEEE Antennas and Wireless Propagation Letters*, vol. 5, pp. 402–405, 2006.

[47] F.-G. Zhu, J.-D. Xu, and Q. Xu, "Reduction of mutual coupling between closely-packed antenna elements using defected ground structure," *Electronics Letters*, vol. 45, no. 12, pp. 601–602, 2009.

[48] S. Xiao, M.-C. Tang, Y.-Y. Bai, S. Gao, and B.-Z. Wang, "Mutual coupling suppression in microstrip array using defected ground structure," *IET microwaves, antennas & propagation*, vol. 5, no. 12, pp. 1488–1494, 2011.

[49] A. Habashi, J. Nourinia, and C. Ghobadi, "A rectangular defected ground structure (DGS) for reduction of mutual coupling between closely-spaced microstrip antennas," in *20th Iranian Conference on Electrical Engineering (ICEE2012)*. IEEE, 2012, pp. 1347–1350.

[50] C.-M. Luo, J.-S. Hong, and L.-L. Zhong, "Isolation enhancement of a very compact UWB-MIMO slot antenna with two defected ground structures," *IEEE Antennas and Wireless Propagation Letters*, vol. 14, pp. 1766–1769, 2015.

[51] K. Wei, J.-Y. Li, L. Wang, Z.-J. Xing, and R. Xu, "Mutual coupling reduction by novel fractal defected ground structure bandgap filter," *IEEE transactions on antennas and propagation*, vol. 64, no. 10, pp. 4328–4335, 2016.

[52] H. Lihao, Z. Huiling, H. Zhang, and C. Quanming, "Reduction of mutual coupling between closely-packed antenna elements with split ring resonator (SRR)," in *2010 International Conference on Microwave and Millimeter Wave Technology*. IEEE, 2010, pp. 1873–1875.

[53] A. Habashi, J. Nourinia, and C. Ghobadi, "Mutual coupling reduction between very closely spaced patch antennas using low-profile folded split-ring resonators (FSRRs)," *IEEE Antennas and Wireless Propagation Letters*, vol. 10, pp. 862–865, 2011.

[54] Z. Qamar, L. Riaz, M. Chongcheawchamnan, S. A. Khan, and M. F. Shafique, "Slot combined complementary split ring resonators for mutual coupling suppression in microstrip phased arrays," *IET Microwaves, Antennas & Propagation*, vol. 8, no. 15, pp. 1261–1267, 2014.

[55] C.-C. Hsu, K.-H. Lin, and H.-L. Su, "Implementation of broadband isolator using metamaterial-inspired resonators and a T-shaped branch for MIMO antennas," *IEEE Transactions on Antennas and Propagation*, vol. 59, no. 10, pp. 3936–3939, 2011.

[56] H. A. Atallah, A. B. Abdel-Rahman, K. Yoshitomi, and R. K. Pokharel, "Mutual coupling reduction in MIMO patch antenna array using complementary split ring resonators defected ground structure." *Applied Computational Electromagnetics Society Journal*, vol. 31, no. 7, 2016.

[57] Y. Torabi, A. Bahri, and A.-R. Sharifi, "A novel metamaterial MIMO antenna with improved isolation and compact size based on LSRR resonator," *IETE journal of research*, vol. 62, no. 1, pp. 106–112, 2016.

[58] J. Zhu, S. Li, B. Feng, L. Deng, and S. Yin, "Compact dual-polarized UWB quasi-self-complementary MIMO/diversity antenna with band-rejection capability," *IEEE Antennas and Wireless Propagation Letters*, vol. 15, pp. 905–908, 2015.

[59] T. Ghosh, S. Ghosal, D. Mitra, and S. R. Bhadra Chaudhuri, "Mutual coupling reduction between closely placed microstrip patch antenna using meander line resonator," *Progress In Electromagnetics Research*, vol. 59, pp. 115–122, 2016.

[60] S. Thummaluru and R. Chaudhary, "Mu-negative metamaterial filter-based isolation technique for MIMO antennas," *Electronics Letters*, vol. 53, no. 10, pp. 644–646, 2017.

[61] G. Srivastava and A. Mohan, "Compact MIMO slot antenna for UWB applications," *IEEE Antennas and Wireless Propagation Letters*, vol. 15, pp. 1057–1060, 2015.

[62] A. Boukarkar, X. Q. Lin, Y. Jiang, L. Y. Nie, P. Mei, and Y. Q. Yu, "A miniaturized extremely close-spaced four-element dual-band MIMO antenna system with polarization and pattern diversity," *IEEE Antennas and Wireless Propagation Letters*, vol. 17, no. 1, pp. 134–137, 2017.

[63] T. Jiao, T. Jiang, and Y. Li, "A low mutual coupling MIMO antenna using 3-D electromagnetic isolation wall structures," in *2017 Sixth Asia-Pacific Conference on Antennas and Propagation (APCAP)*. IEEE, 2017, pp. 1–2.

[64] Z. Li, X. Zhu, and C. Yin, "CPW-fed ultra-wideband slot antenna with broadband dual circular polarization," *AEU-International Journal of Electronics and Communications*, vol. 98, pp. 191–198, 2019.

[65] R. K. Saini and S. Dwari, "A broadband dual circularly polarized square slot antenna," *IEEE Transactions on Antennas and Propagation*, vol. 64, no. 1, pp. 290–294, 2015.

[66] R. Xu, J.-Y. Li, J. Liu, S.-G. Zhou, Z.-J. Xing, and K. Wei, "A design of dual-wideband planar printed antenna for circular polarization diversity by combining slot and monopole modes," *IEEE Transactions on Antennas and Propagation*, vol. 66, no. 8, pp. 4326–4331, 2018.

[67] R. Xu, J.-Y. Li, J.-J. Yang, K. Wei, and Y.-X. Qi, “A design of u-shaped slot antenna with broadband dual circularly polarized radiation,” *IEEE Transactions on Antennas and Propagation*, vol. 65, no. 6, pp. 3217–3220, 2017.

[68] D. Chandu and S. Karthikeyan, “A novel broadband dual circularly polarized microstrip-fed monopole antenna,” *IEEE Transactions on Antennas and Propagation*, vol. 65, no. 3, pp. 1410–1415, 2017.

[69] S. Chaudhuri, R. S. Kshetrimayum, and R. K. Sonkar, “Dual circularly polarized slot antenna with novel isolator,” in *2019 41st Photonics And Electromagnetics Research Symposium PIERS.* PIERS, 2019, pp. 1–5.

[70] G.-L. Wu, W. Mu, G. Zhao, and Y.-C. Jiao, “A novel design of dual circularly polarized antenna fed by l-strip,” *Progress In Electromagnetics Research*, vol. 79, pp. 39–46, 2008.

[71] C. Min and C. E. Free, “Dual-ring circularly-polarized microstrip patch array using hybrid feed,” *IEEE Transactions on Antennas and Propagation*, vol. 57, no. 6, pp. 1825–1828, 2009.

[72] P. Hallbjorner, I. Skarin, K. From, and A. Rydberg, “Circularly polarized traveling-wave array antenna with novel microstrip patch element,” *IEEE Antennas and Wireless Propagation Letters*, vol. 6, pp. 572–574, 2007.

[73] S. J. Chen, C. Fumeaux, Y. Monnai, and W. Withayachumnankul, “Dual circularly polarized series-fed microstrip patch array with coplanar proximity coupling,” *IEEE Antennas and Wireless Propagation Letters*, vol. 16, pp. 1500–1503, 2017.

[74] S. Chaudhuri, R. S. Kshetrimayum, and R. K. Sonkar, “High inter-port isolation dual circularly polarized modified Franklin microstrip antenna,” in *2019 13th European Conference on Antennas and Propagation (EuCAP).* IEEE, 2019, pp. 1–4.

[75] Y.-H. Yang, J.-L. Guo, B.-H. Sun, Y.-M. Cai, and G.-N. Zhou, “The design of dual circularly polarized series-fed arrays,” *IEEE Transactions on Antennas and Propagation*, vol. 67, no. 1, pp. 574–579, 2018.

[76] W. K. Chen, *The electrical engineering handbook.* Elsevier, 2004.